A NEW POOL BOILING FACILITY FOR THE STUDY OF NANOFLUIDS

A NEW POOL BOILING FACILITY FOR THE STUDY OF NANOFLUIDS

By JAMES M. V. STRACK, B.Eng.Mgt.

A Thesis
Submitted to the School of Graduate Studies
in Partial Fulfillment for the Requirements for the Degree
Master of Applied Science

McMaster University

MASTER OF APPLIED SCIENCE (2013) MCMASTER UNIVERSITY

(Engineering Physics) Hamilton, Ontario, Canada

Title: A New Pool Boiling Facility for the Study of Nanofluids

Author: James Michael Vincent Strack, B.Eng.Mgt. (McMaster University)

Supervisor: Dr. D.R. Novog

Number of Pages: xviii, 137

Abstract

Nanofluids are engineered colloidal dispersions of nanoparticles in a liquid. The field of nanofluids has seen much interest due to reported heat transfer enhancements over the corresponding pure fluids at low particle concentrations. Particularly, a large increase in critical heat flux (CHF) has been widely reported along with modification of the boiling interface. Inconsistencies in reported impact on nucleate boiling heat transfer and the degree of CHF enhancement illustrate the need for further study.

A pool boiling experiment has been designed and constructed at McMaster University to allow for the study the boiling of water-based nanofluids. The facility has been commissioned with saturated distilled water tests at atmospheric pressure, heat flux levels up to 1200 $kW \cdot m^{-2}$, and at wall superheat levels up to 19.5^{o}C. Wall superheat and heat flux uncertainties were estimated to be ±0.6^{o}C and ±20 $kW \cdot m^{-2}$, respectively. For the installed test section, heat flux is limited to 2.62 ± 0.06 $MW \cdot m^{-2}$. A high speed video system for the analysis of bubble dynamics was tested and used for qualitative comparisons between experimental runs. This system was tested at 2500 FPS and an imaging resolution of 39 pixels

per mm, but is capable of up to 10 000 FPS at the same spatial resolution. Heat flux versus wall superheat data was compared to the Rohsenow correlation and found to qualitatively agree using surface factor C_{sf} = 0.011. Results were found to have a high degree of repeatability at heat flux levels higher than 600 $kW \cdot m^{-2}$.

The new facility will be used to conduct studies into the pool boiling of saturated water-based nanofluids at atmospheric pressure. Additional work will involve the control and characterization of heater surface conditions before and after boiling. Quantitative analysis of bubble dynamics will be possible using high speed video and particle image velocimetry.

Acknowledgements

This project would not have been possible without the help and support of several people. First, I would like to thank my supervisor Dr. David Novog for his guidance, advice, and endless patience over the past two and a half years. It has been truly appreciated.

I would also like to thank Clealand Berwick and Jim Cleaver at the machine shop for their support in the design and manufacturing of the boiling vessel. Additional thanks to Jim Garrett for the manufacturing of the ceramic insulator and soldering of the thermocouples. Thanks are also due to Dr. Shinya Nagasaki for providing laboratory space and Dr. Jim Cotton for loaning the thermocouple calibration apparatus.

Thanks also go out to the entire research group for the endless coffee/beer runs and lab shenanigans necessary for maintaining sanity over the past years.

Finally, I would like to thank my family for their endless support in everything I have always done. This would not have been possible without you.

Table of Contents

List of Figures

List of Tables

List of Symbols

a	linear best fit intercept
b	linear best fit slope
c_{pf}	specific heat of fluid
C_{sf}	surface factor constant in Rohsenow correlation
Cu	copper
CHF	critical heat flux
CJC	cold junction compensation
D	test section diameter
D_d	bubble departure diameter
DLS	dynamic light scattering
f	bubble departure frequency)
FPS	frames per second
g	acceleration due to gravity
h_{fg}	latent heat of vaporization
k	thermal conductivity

K	constant in Zuber correlation
L	heater characteristic dimension
L'	heater characteristic dimension (dimensionless)
NPS	nominal pipe size
NPT	national pipe thread
OD	outer diameter
ONB	onset of nucleate boiling
P	power
Pr	Prandtl number
PIV	particle image velocimetry
PTFE	polytetrafluoroethylene
PVC	polyvinyl chloride
q''	heat flux
r	constant in Rohsenow correlation
R^2	square of Pearson product-moment correlation coefficient
s	constant in Rohsenow correlation (Chapter 1)
s	sample standard deviation (Chapter 4)
s^2	sample variance (Chapter 4)
SEM	scanning electron microscopy
T_{bulk}	bulk fluid temperature
T_{cal}	calibrated temperature
T_i	temperature at location i

T_w	wall temperature
T_{sat}	saturation temperature
ΔT_{wall}	$T_{wall} - T_{bulk}$
z	vertical position
λ_d	Taylor instability wavelength
μ_f	dynamic viscosity
ρ_f	liquid phase density
ρ_g	vapour phase density
$\Delta\rho$	density change between liquid and vapour phases ($\rho_f - \rho_g$)
σ	surface tension (Chapter 1)
σ	standard deviation (Chapter 4)
σ^2	variance (Chapter 4)

Chapter 1

Introduction

Knowledge of heat transfer – the transport of thermal energy between physical systems through conduction, convection, or radiation – and thermal hydraulics – the study of fluid mechanics in thermal systems – are important to many disciplines. A prime example is in a thermal nuclear power plant where thermal energy is released from fuel undergoing a fission process. This thermal energy is transported via a coolant and used to generate steam which powers turbines to generate electricity. Adequate cooling of the fuel must be maintained during plant operation and shutdown to prevent damage to the fuel. Increasing understanding of thermal hydraulics is therefore not only important in terms of increasing the efficiency of a system but also in enhancing safety.

Nanofluids are engineered colloidal dispersions of nanoparticles in a liquid. The term “nanoparticle” in this context refers to particles 1 – 100 nm in size. Typical examples of the liquid used as the base of a nanofluid include water, ethanol, oil, ethylene glycol, and refrigerant; the nanoparticles include metals (copper, silver,

gold), metal oxides (alumina, titanium oxide, copper oxide, silica), carbides, and carbon nanotubes. Following the pioneering work of Choi et al [1], the field of nanofluids has seen much interest due to reported heat transfer enhancements over the corresponding pure fluids, even at low particle concentrations.

The theory of enhancing the heat transfer characteristics of a fluid using dispersed solid particles originated with Maxwell [2]. However, the inclusion of millimeter- and micrometer-sized particles has been found to have limited practicality due to increased abrasion, clogging, sedimentation, and increased pressure drop [3]. Nanoparticles are closer in size to fluid molecules; their small size and momentum reduce chances of sedimentation, erosion, clogging, and give a high surface area for heat transfer [3].

In early studies involving nanofluids, work was focused on thermal conductivity enhancement involving higher concentrations of nanoparticles (volume fractions up to 20%) suspended in coolants engine oil and ethylene glycol [1]. Several additional studies into heat transfer with nanofluids have been conducted and report modifications in thermal-dynamic properties in comparison to their base fluid which could not be explained using existing theory, including enhanced thermal conductivity, convective heat transfer, boiling heat transfer, and critical heat flux (CHF) [4]. Inconsistencies in the reported results between research groups – especially dealing with boiling heat transfer – illustrate the limited

understanding of the underlying heat transfer mechanisms, difficulties in consistent nanofluid preparation, and the need for further study [4].

1.1 Pool Boiling Background

1.1.1 Vapour Formation and Nucleation

Vapour formation in boiling can result from three processes: evaporation, homogeneous nucleation, and heterogeneous nucleation [5]. In practical applications of boiling, evaporation and heterogeneous nucleation are the dominant mechanisms. In the heterogeneous nucleation process, non-condensable gases such as air become trapped in flaws or imperfections in the heated surface (such as cracks, cavities, or debris) [5]. These nucleation sites can then act as centres for vapour generation. When the temperature at a nucleation site is above a certain level (the critical superheat; dependent on nucleation site size and the fluid), the vapour nucleus will grow out of the site and the nucleation process initiates occurs.

The size and geometry of vapour bubbles leaving a heated surface depend on the size of nucleation sites, surface tension and liquid inertia forces preventing bubble detachment, and buoyancy and drag forces promoting detachment [5]. Thermo-capillary convection, also known as Bérnard-Marangoni convection may also have an effect. This effect, which results in fluid flowing from areas of low surface tension to high surface tension, is caused by temperature gradients in the

fluid resulting in surface tension gradients [6]. In general, for a given heater geometry and fluid conditions the product of bubble departure frequency f and diameter D_d is a constant representing the superficial vapour velocity. Given the surface tension σ, liquid and vapour densities ρ_f and ρ_g, this product fD_d was evaluated by Zuber to be represented as [5]:

$$fD_d = 0.59\left[\frac{\sigma g(\rho_f - \rho_g)}{\rho_f^2}\right]^{1/4} \tag{1.1}$$

1.1.2 Pool Boiling Curve

Pool boiling is defined as the boiling of a stagnant liquid at a submerged heated surface [5]. If the bulk of the liquid is below its boiling point the process is termed subcooled pool boiling; if the liquid is at its boiling point it is termed saturated pool boiling. A typical boiling curve (heat flux versus wall superheat) for the pool boiling of water is shown in Figure 1-1. A description of each region follows below. In general, systems can be divided into heat flux controlled (heat generation rate is the independent variable) and temperature controlled (wall temperature is the independent variable). For the purposes of this experimental program, greater attention is paid toward heat flux controlled systems since heater power is the controlled variable in the experiment.

1.1.2.1 Natural Convection Region

Between points A and B', the wall superheat is low enough that nucleation sites are not active and heat at the wall is removed by single phase natural convection to the fluid.

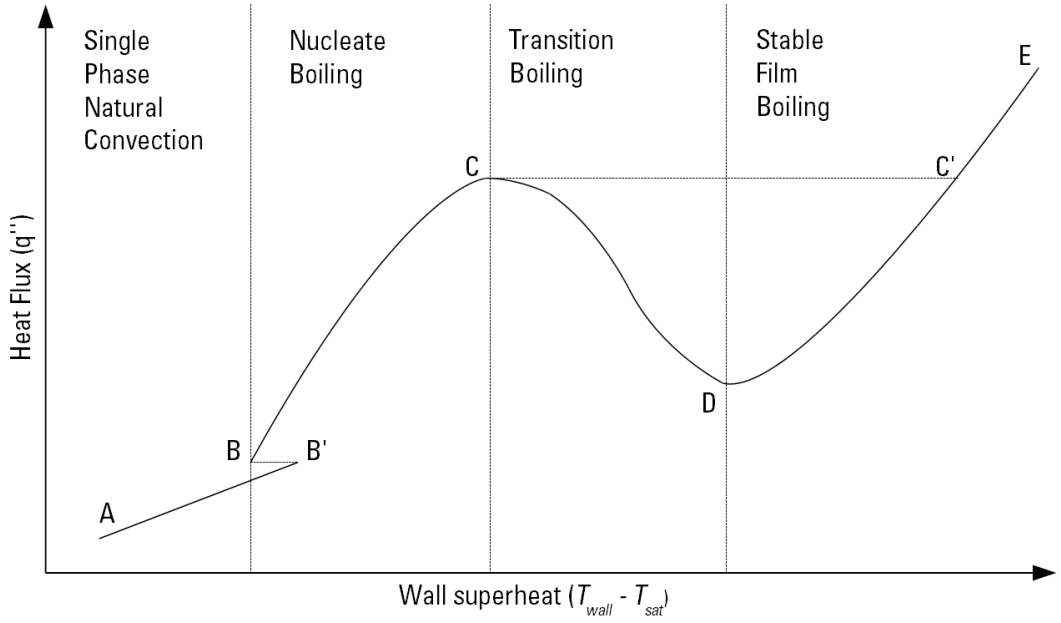

Figure 1-1: Typical pool boiling curve [7]

1.1.2.2 Nucleate Boiling

At higher heat fluxes, the wall superheat increases and becomes sufficient for nucleation sites to become active. Following the onset of nucleate boiling (region B-C in Figure 1-1), the slope of the boiling curve increases due to improved heat removal. This improved heat transfer results from three mechanisms [5]:

- Bubble agitation: induced fluid motion from the growing and departure of bubbles results in an increase in near wall turbulence improving fluid mixing.
- Thermal boundary layer stripping: as bubbles rise, cooler liquid flows downward to replace them.
- Evaporation: The process of vaporizing liquid into superheated vapour causes heat to be transported from the surface to the bubble as latent heat.

Additionally, Marangoni flows caused by surface tension gradients at the bulk fluid/vapour bubble interface may also contribute to improved boiling heat transfer. In general, liquids exhibit decreasing surface tension with increasing temperatures [8]. The Marangoni effect mentioned in section 1.1.1 causes a flow from areas of low surface tension (warm fluid) to high surface tension (cool fluid). The result is a liquid flow around the periphery of the vapour bubble; this is illustrated in Figure 1-2. For departing vapour bubbles, this causes liquid to be drawn toward the heater surface. The contribution of these convection currents to boiling heat transfer is not agreed upon and often considered insignificant to convective currents resulting from buoyancy effects, but the effect is larger at higher levels of fluid subcooling [8].

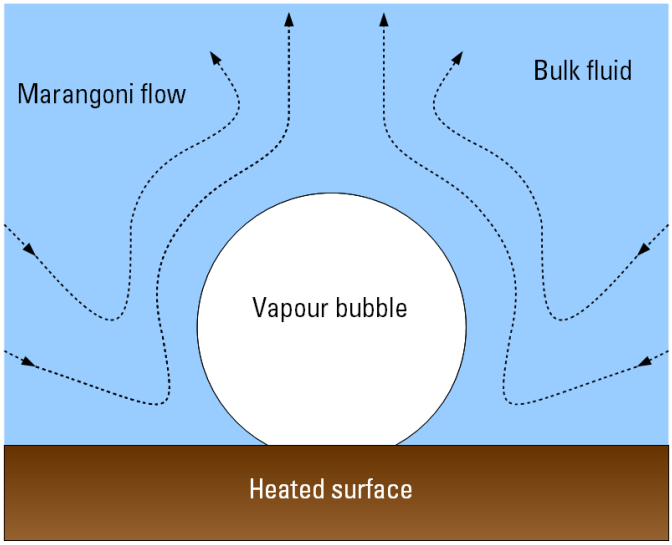

Figure 1-2: Marangoni convection in subcooled nucleate boiling [8]

The boiling curve may be discontinuous at the onset of nucleate boiling (point B-B') as the activation of nucleation sites may occur at a wall superheat level higher than required to sustain developed nucleate boiling [5]. This may result in a drop in wall temperature following the onset of nucleate boiling. This discontinuity is dependent on pressure and is typically small for water at atmospheric conditions. [5].

While a large number of correlations exist for heat transfer in the nucleate boiling region, the Rohsenow correlation is often used to describe this region of the boiling curve in pool boiling [9]:

$$q'' = \mu_f h_{fg} \left[\frac{\sigma}{g\Delta\rho}\right]^{-\frac{1}{2}} \left(\frac{1}{C_{sf}}\right)^{\frac{1}{r}} \cdot \mathrm{Pr}^{-\frac{s}{r}} \left[\frac{c_{pf}(T_w - T_{sat})}{h_{fg}}\right]^{\frac{1}{r}} \tag{1.2}$$

Here, q'' is heat flux, $\mu_f$is liquid viscosity, h_{fg} is the latent heat of vaporization, σ is the surface tension, g is the acceleration due to gravity, $\Delta\rho$ is the change in density between liquid and vapour phases, Pr is the Prandtl number, c_p is the liquid specific heat, $T_w - T_{sat}$ is the wall superheat, *s* and *r* are constants, and C_{sf} is an arbitrary surface constant. The surface constant is included to capture the variation in behaviour between different fluids, surface materials, and surface finishes.

1.1.2.3 Critical Heat Flux

At a certain elevated heat flux, the rate of vapour leaving the heated surface becomes high enough to restrict liquid from returning to the surface [5]. This departure from nucleate boiling (point C) causes deterioration in heat transfer. In a heat flux controlled system, this causes a rapid temperature excursion from point C to point C' in Figure 1-1. In many circumstances, this rapid rise in temperature is significant enough to cause severe damage to the heated surface.

For saturated fluids, the Zuber correlation is used to predict CHF on large, horizontal, upward facing surfaces [5]:

$$q''_{CHF,Zuber} = K h_{fg} \rho_g^{1/2} \left[g\sigma\left(\rho_f - \rho_g\right) \right]^{1/4} \tag{1.3}$$

Here *K* is a constant, $h_{fg}$is the latent heat of vaporization, ρ_f and ρ_g are the densities of the fluid and vapour, and σ is surface tension. Zuber specified *K* to be

$\pi/24$ [5]. Later studies by Lienhard extended Equation 1.3 to take into account various heater geometries and to take into account additional empirical data by adding a multiplying factor to *K*; this multiplying factor is a function of a characteristic length *L'* which itself is a function of the Taylor instability wavelength λ_d [5]:

$$L' = 2\pi\sqrt{3}\frac{L}{\lambda_d} \tag{1.4}$$

$$\lambda_d = 2\pi\sqrt{3}\left[\frac{\sigma}{g(\rho_f - \rho_g)}\right]^{0.5} \tag{1.5}$$

The heater characteristic dimension in Equation 1.4 depends on the heater geometry; several examples are presented below in Table 1-1; these relationships are not valid for small heater geometries.

Critical heat flux is also dependent on surface wettability. In a study by Liaw and Dhir involving water, the wettability of heater surfaces was increased through oxidation; it was found that CHF increased with decreasing contact angle (with corresponding increasing surface wettability) [5]. Surface modification following pool boiling studies with nanofluids have also been observed and suspected as playing a large role in CHF enhancement [10]. This phenomenon is further discussed in Chapter 2: Literature Review.

Table 1-1: Critical heat flux for select finite bodies as presented in Collier and Thome [5]

Geometry	$\frac{q''_{CHF}}{q''_{CHF,Zuber}}$	Dimension	Range
Infinite flat plate	1.14	Width or diameter (L)	$L' \geq 2.7$
Small flat plate	$1.14\frac{A_{heater}}{\lambda_d^2}$	Width or diameter (L)	$0.07 \leq L' \leq 0.2$
Small horizontal cylinder	$\frac{0.94}{R'^{0.25}}$	Radius (R)	$R' \geq 1.2$
Large horizontal cylinder	0.90	Radius (R)	$0.15 \leq R' \leq 1.2$
Large finite body	~ 0.9	Length (L)	$\sim L \geq 4$

1.1.2.4 Transition Boiling

In a temperature controlled system (where wall temperature is held approximately constant rather than heat flux), the C-D region of the boiling curve is referred to as transition boiling. This region is characterized by an unstable vapour blanket which is formed and released from the heater surface at roughly regular intervals [5]. Additionally it is believed that intermittent rewetting of the surface occurs [5].

1.1.2.5 Film Boiling

Also in temperature controlled systems, the C-C' region of the boiling curve is referred to as the film boiling region. This region is characterized by a stable vapour blanket encompassing the heater surface. In this region, convection and conduction are the dominant heat transfer mechanisms [5].

1.2 Outline

In Chapter 1 the motivation of the current experimental program is identified and discussed along with some background information regarding pool boiling of fluids at saturation. Chapter 2 reviews existing literature on nanofluids, identifying production methods as well as existing experimental results for nanofluid pool boiling, highlighting observed impacts on boiling heat transfer and critical heat flux. Chapter 3 provides specifications for the experimental facility. Chapter 4 presents and discusses the results of commissioning tests conducted at atmospheric pressure using a copper heater surface and distilled water. A breakdown of future work including pending improvements to the facility and the future direction of the research program is provided in Chapter 5 while conclusions are summarized in Chapter 6.

Chapter 2

Literature Review

The following chapter contains a review of past literature concerning nanofluids and their potential applications in heat transfer augmentation. First, the preparation methods used to create stable dispersions are reviewed. This was necessary to identify the material requirements for the design of the boiling facility and also to ensure reliable data were collected. Next, results from existing nanofluid pool boiling studies are discussed, identifying observed impacts on the boiling heat transfer performance, critical heat flux, and any heater surface modification.

2.1 Nanofluid Preparation Methods

The methods used for the synthesis of nanofluids can be classified into three categories: one-step physical, one-step chemical, and two-step. One-step methods involve the simultaneous creation of nanoparticles and colloidal dispersion in situ; two-step methods involve the production of dry powders and dispersion in fluids as two separate steps [11].

2.1.1 Two-Step (Dispersion) Method

The dispersion method of nanofluid preparation is the most commonly used and involves the creation of dry nanoparticles followed by the subsequent dispersion into a fluid [11]. Dry nanoparticles can be created through such processes as inert gas condensation, chemical vapour deposition, and mechanical milling; due to van der Waals forces between the particles, the nanoparticles tend to agglomerate, making the production of a stable dispersion difficult [12].

The presence of large agglomerates in nanofluids may cause settling and contribute to erosion and clogging in process systems, causing heat transfer deterioration and similar problems seen with micro-scale particle dispersions. Techniques such as mechanical mixing and ultrasonic vibration are used to break these agglomerates. Additionally, chemical additives such as surfactants and/or pH modification are used to increase the stability of dispersion method nanofluids [11]. Nanofluids produced in this manner have typically achieved stable dispersions with average particle sizes on the order of 50-200 nm, starting with a dry nanoparticle size on the order of 10-20 nm [9].

The addition of surfactants and pH modification may significantly alter the fluid properties of the base fluid and, in turn, their heat transfer performance. These effects may be undesirable and must be considered in experimental studies. Additionally, pH modification may introduce corrosion concerns and surfactants may break down at high temperatures. Oxidation of metallic nanoparticles

following their production creates further difficulties in the synthesis of metallic nanofluids [11]. The main advantage of the two-step method lies in the industrial scale production of the dry nanoparticles, yielding reduced cost and increased practicality of employing the resulting nanofluids in real-world applications. Because of the role of surfactants on the boiling process it is unclear if the observed heat transfer trends for such nanofluids result entirely from the particles or from the surfactant modification of the nucleation process.

2.1.2 One-Step Methods

One-step methods involve the simultaneous creation and dispersion of nanoparticles in a fluid. Physical one-step methods include direct evaporation whereby a material is vaporized in a vacuum [12]. Nanofluids have also been produced using the submerged arc nanoparticle synthesis method whereby a metal electrode is heated by arc sparking while the base fluid is simultaneously vaporized and condensed in a vacuum chamber [13]. An example one-step chemical method was developed by Zhu et al and involved the reduction of copper sulphate under microwave irradiation to produce copper-ethylene glycol nanofluids [14].

One-step methods have the advantages of reduced particle agglomeration, reduced nanoparticle oxidation (in the case of metallic nanoparticles), and more directly controllable nanoparticle size [11]. Disadvantages include difficulties in scaling

production beyond laboratory scale and difficulties in producing nanofluids with high volumetric concentrations of nanoparticles [11].

2.2 Pool Boiling of Nanofluids

Studies into pool boiling heat transfer of nanofluids have yielded mixed results between researchers. Several researchers have observed enhanced boiling heat transfer while others have observed deteriorated boiling heat transfer or little change at all. In one of the first studies, You et al. reported a significant enhancement of CHF (up to 200% increase) in alumina (Al_2O_3) nanofluids at low volumetric concentrations of 0.001 to 0.05 g/L while boiling heat transfer coefficients remained roughly constant [15]. A positive correlation of CHF enhancement was also observed with increasing nanofluid concentration. It was further noted that bubble departure size was increased and bubble departure frequency was decreased.

In a recent review by Taylor et al. [9], it was noted that there was nearly an even three-way split between experimental results which supported increased, decreased, and no effect on boiling heat transfer even when similar heater geometries, base fluids, and nanoparticles were used. In most studies, fouling of the boiling surface from the deposition of nanoparticles was also noted [9].

2.2.1 Surface Modification and Wettability

As noted by Taylor et al. in their review, the majority of nanofluid pool boiling studies have noted particle deposition on the heater surface following boiling [9]. It has been widely reported that this layer of particles is a contributing factor in the CHF enhancement and nucleate boiling heat transfer performance observed in nanofluid boiling. The greater the thickness of the deposited surface, the greater the thermal resistance which suggests a decreased heat transfer coefficient would result [16]. However, the porous nature of the deposited surface may allow some micro-fluidic effect within the coating which may offset some of the thermal resistance.

In a study of water-based nanofluids by Kim et al. [17], nanoparticle fouled surfaces following nanofluid boiling were found to exhibit increased capillary wicking due to the presence of a porous nanoparticle layer. This would allow increased surface re-wettability, delaying the growth of a dry patch during vapour bubble formation contributing to the enhancement of CHF. The group also observed a decreased droplet contact angle following nanoparticle deposition, indicating an increased surface wettability [18]. To further investigate the effect of the nanoparticle layer, pure water was boiled on surfaces fouled by TiO_2 and Al_2O_3. Kim et al. observed that the CHF of pure water boiled on nanoparticle fouled surfaces was enhanced by up to 175% [18]. Using the same experimental apparatus, CHF enhancement observed through the pool boiling of nanofluids was

as high as 115%, indicating that the nanofluids themselves may exhibit a lower CHF than the corresponding pure fluid given an appropriate heater surface treatment [18]. The capillary wicking effect observed from this porous layer of deposited nanoparticles may have an impact on the Marangoni flows previously discussed in section 1.1.2.2.

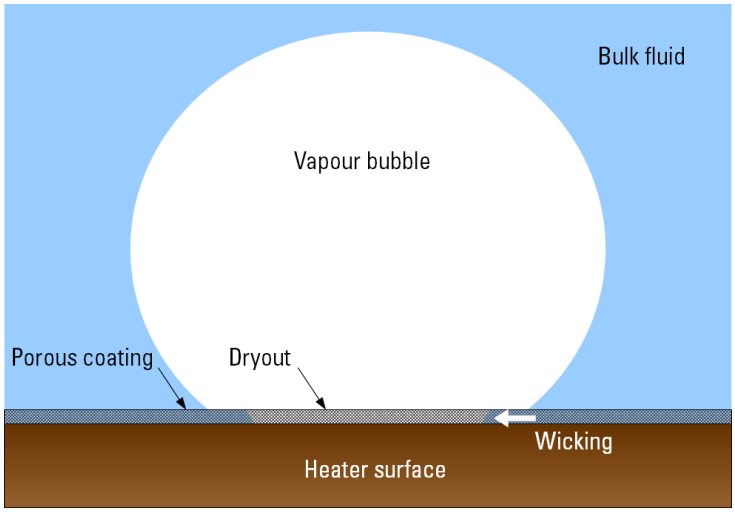

Figure 2-1: Capillary wicking as a mechanism for surface re-wetting in nanofluid pool boiling. The porous coating on the heater surface is composed of deposited nanoparticles following boiling in nanofluids [17]

Similarly, a vertical dip test of nanoparticle fouled boiling surfaces was performed by Kwark et al. [19]. This test involved placing the heater vertically into water and observing the movement of the liquid front. An uncoated heater showed no wicking while a heater boiled in nanofluids showed a wicking head of 2.6 mm. Using high speed video, the wicking front was measured to move at approximately 0.1 m/s. The superficial vapour velocity of pure water (refer to Equation 1.1) was also measured for similar heater geometries to be 0.081 m/s,

suggesting that the speed of the wicking front would be sufficient to rewet the heater surface, delaying CHF [19].

In a study of surface wettability by Coursey et al. [20], CHF enhancement in poorly wetting systems (such as water on copper) were compared to better wetting systems (such as ethanol on glass). It was observed that water-based nanofluids exhibited CHF enhancement and little change in nucleate boiling performance at low particle concentrations while better wetting systems such as ethanol nanofluids showed no CHF enhancement even at high particle concentrations. Additionally, water nanofluids were observed to exhibit a decreased contact angle only after boiling, indicating that the improved surface wettability resulted from nanoparticle deposition as a result of boiling. Furthermore, similar CHF enhancements as those seen with water-based nanofluids were observed with pure water and oxidized copper surfaces but with a lower wall superheat.

In a continuation of the study by You et al, Kwark et al. explored the effect of nanoparticle concentration on nucleate boiling heat transfer and CHF at atmospheric pressure with water based nanofluids [16]. It was noted that CHF enhancement increased with volumetric concentration until a critical value in concentration is reached. Further increases in concentration did not improve CHF but resulted in deteriorated nucleate boiling heat transfer. It was postulated that CHF enhancement resulted from increased surface wettability due to the formation of a porous nanoparticle coating.

As the nanofluid concentration increased, deposition of nanoparticles on the heater surface also increased during boiling. The wettability of the surface was thought to increase up to a critical value where the porosity of the surface could no longer be improved through further deposition. However, continued particle deposition would increase thermal resistance at the heater, impeding boiling heat transfer. Therefore, an optimal nanofluid concentration of 0.025 g/L was found which yielded maximum CHF enhancement with minimum degradation in boiling heat transfer; this concentration was independent of the nanoparticle type tested (diamond, Al_2O_3, CuO) [16].

Additionally, Kwark et al. observed transient behaviours in nanofluid boiling. With a constant heat flux during nucleate boiling, the wall superheat was observed to increase with time, suggesting that heat transfer degrades as boiling continued [16]. Kwark et al. suggested that this was a result of continued nanoparticle deposition during the boiling process, increasing thermal resistance at the heater surface. CHF enhancement was not found to depend on the length of the boiling tests, further supporting their postulation that the CHF enhancement of water-based nanofluids was a function of surface wettability.

The mechanisms behind the deposition of nanoparticles in nanofluid boiling experiments have also been investigated. Kwark et al. hypothesized that the creation of a nanoparticle coating on the heater surface could be a result of particle settling and precipitation, interactions at natural convection, an applied

electric field (emf leakage from the heater), and nucleate boiling [16]. Heater surfaces were prepared using a 0.025 g/L Al_2O_3 nanofluid to test these effects separately and then conducted pool boiling tests with each in pure water. The first surface was placed in the nanofluid for 1 hour with no applied heat (deposition), the second surface was heated at 10 $kW \cdot m^{-2}$ in the nanofluid for 1 hour, the third surface was placed in the nanofluid and subjected to a 2.5 kV/m electric field for 1 hour, and the fourth was heated in the nanofluid until CHF occurred. The first three surfaces showed minimal nanoparticle deposition and exhibited marginal change in CHF when compared to a clean heater surface [16]. The surface prepared via nucleate boiling in the Al_2O_3 nanofluid showed nanoparticle deposition and exhibited a 64% enhancement in CHF in pure water when compared to a clean surface [16]. Thus, it was concluded that the boiling process itself was responsible for the creation of the nanoparticle coating and resulting enhancement in CHF.

Recent studies of copper-water [21] and carbon nanotube (CNT)-water nanofluids [22] by Kathiravan et al. yielded interesting results. The boiling of copper-water nanofluids was observed to cause decreased boiling heat transfer coefficients with increasing nanoparticle concentrations while enhancing CHF; fouling of the boiling surface with a nanoparticle layer was also observed. These observations are consistent with previously reported results. However, no fouling of the boiling surface was observed during CNT-water nanofluid boiling. In this case, CHF degradation was observed with increasing CNT concentration while the boiling

heat transfer coefficient was observed to increase. Kathiravan et al. pointed out that these results were preliminary and suggested that further study was necessary.

2.3 Summary

- The boiling heat transfer characteristics of nanofluids are modified with respect to their base fluids at low particle concentrations. These low concentrations (< 1 g/L) are such that the fluid properties of the nanofluid such as density, viscosity, latent heat of vaporization, and surface tension are not affected.
- Surface fouling following the boiling of nanofluids has been widely reported and investigated as the cause of modified boiling heat transfer. Since the fluid properties are not affected at low concentrations, the Rohsenow correlation suggests that impacts to the nucleate boiling regime are due to this modification (surface factor C_{sf}).
- Nanoparticle fouled surfaces often exhibit improved surface wettability as shown through decreased contact angles using sessile drops in several studies. Additionally, nanoparticle fouled surfaces have been shown to exhibit enhanced capillary wicking through vertical dip tests. These behaviours are observed only following boiling and subsequent fouling by nanoparticles (i.e. – clean surface and nanofluid combinations do not exhibit enhanced wicking or decreased contact angles).

- The deposited layer of nanoparticles can impact the heat transfer coefficient in the nucleate boiling regime. This layer increases the effective thermal resistance between the heated surface and the fluid, increasing wall superheat for a given heat flux when compared to the analogous pure fluid.
- The heat transfer coefficient in the nucleate boiling regime has shown to exhibit transient behaviour (e.g. – with heat flux held constant, the wall superheat increases over time). It has been hypothesized that this results from continued deposition of nanoparticles onto the heater surface over time, with a resulting increase in thermal resistance.
- Conflicting results between research groups with respect to boiling heat transfer performance may result partly from this transient behaviour if these time dependent characteristics of boiling are not taken into account during experiments.
- Nanofluid pool boiling has shown enhanced CHF of up to 200% resulting from improved surface wettability resulting from nanoparticle deposition. This enhancement is more dramatic in more poorly wetting systems (e.g. – water on copper boiling surfaces) when compared to better wetting systems (e.g. – ethanol on copper).
- Studies by Kim et al [18] have suggested that pure fluids boiled on nanoparticle fouled surfaces produced through nanofluid boiling may exhibit further enhanced CHF over nanofluid pool boiling CHF. This

further supports the idea that CHF enhancement in nanofluid boiling is a result of nanoparticle deposition resulting from boiling rather than the presence of dispersed nanoparticles in the fluid.

Chapter 3

Experimental Details

In order to pursue the study of pool boiling, a new experimental facility was designed and constructed. The design requirements for the new facility were as follows:

- The vessel should allow for boiling of pure water as well as nanofluids.
- The boiling surface should be removable so that measurements can be made of surface modifications (if any) caused by the boiling of the nanofluids.
- The volume of the vessel should be minimized such that the amount of nanofluids required can be reduced.
- There should be wall as well as fluid temperature measurements.
- It should allow for the condensation of any generated vapour such that nanofluids and nanoparticles are not released to the environment.

- It should allow for visual and/or laser access of the heater surface for optical measurements of bubble size, nucleation rate, and departure diameter.
- It should allow the boiling surface to be heated at up to 3 MW/m^2 which is the maximum expected critical heat flux for these fluids.

An overview of the test facility is presented in Figure 3-1. The facility consists of a stainless steel vessel constructed of NPS 4 inch piping, approximately 2 L in volume. Two polycarbonate windows located at the midsection of the vessel provide visual access to the boiling surface. An external tank heater is used to maintain the bulk fluid temperature at the saturation point. The boiling surface is an exposed face of a 9.53 mm diameter (0.375 in) copper rod. At the base of the copper rod is a 15.9 mm diameter (0.625 in) copper tube with a cartridge heater embedded. Surrounding the copper test section is an alumino-silicate ceramic insulator to reduce radial heat loss. Heat delivered to the test section is controlled using a variable autotransformer. A cooling tank at the top of the vessel is used to condense rising vapour to keep the fluid level in the tank constant.

Five K-type thermocouples mounted to the test section are used to measure the temperature gradient between the cartridge heater and the boiling surface. These measurements are used to measure the heat flux and estimate the boiling surface temperature. Additionally, high speed video is used to capture the dynamics of the

boiling process. Further details on the apparatus follow in the sections below; detailed drawings of the boiling vessel are attached in Appendix D on page 109.

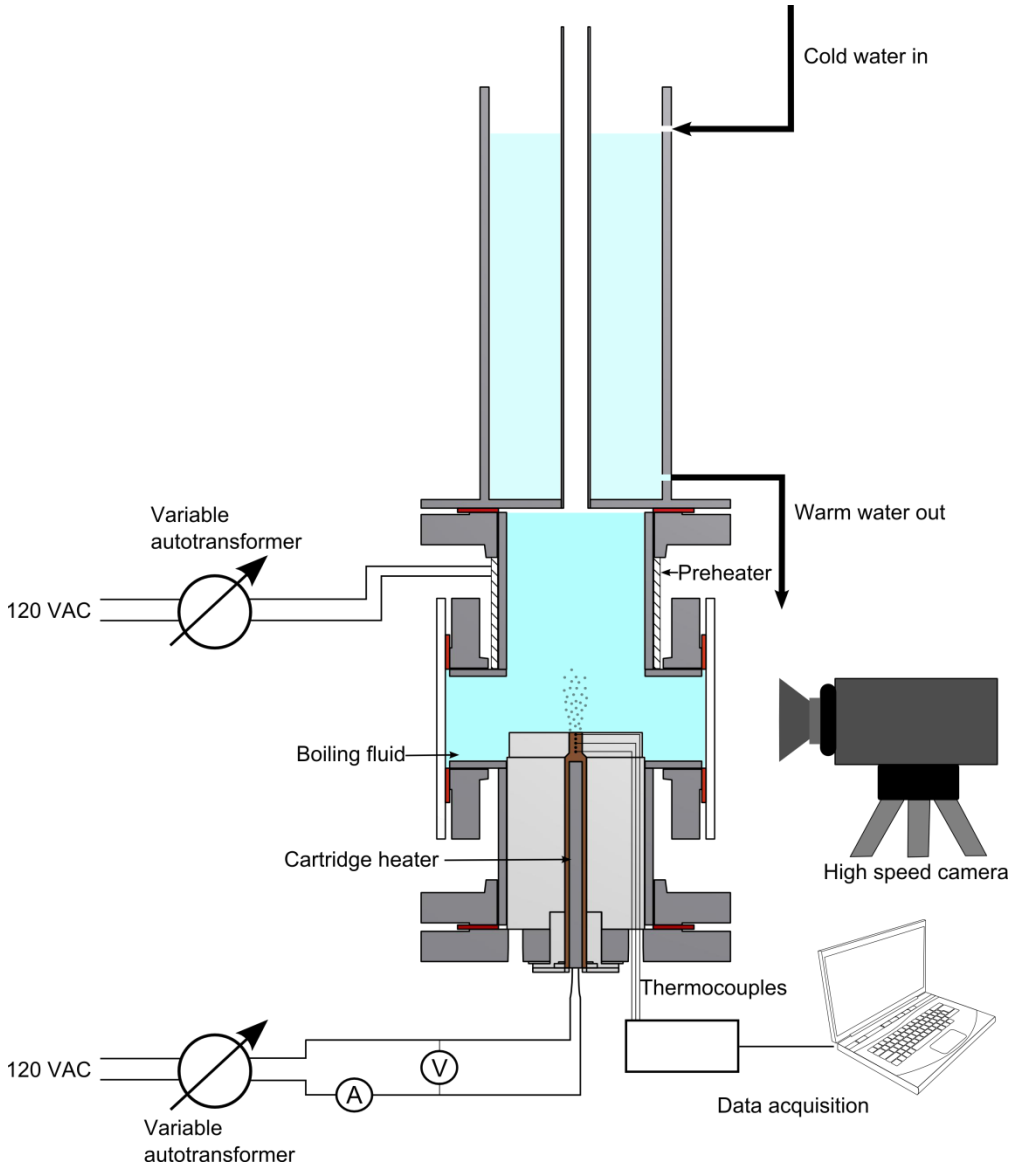

Figure 3-1: Schematic of pool boiling experiment

The facility was commissioned by conducting boiling experiments with distilled water; the results of these tests are presented in Chapter 4.

3.1 Boiling Vessel

3.1.1 Main Tank and Pre-Heater

The body of the boiling vessel is constructed from 102 mm (4 in) nominal diameter schedule 40 stainless steel T304 piping (OD 114.3 mm, 6.02 mm wall thickness). Two viewing ports, constructed of 64 mm (2.5 in) nominal diameter schedule 40 T304 piping (OD 73.02 cm, 5.16 mm wall thickness), are welded to the tank body to provide light and visual access for high speed photography. ANSI B16.5 150 PSI (1.034 MPa) flanges are welded to the extents of the piping and the viewing ports to facilitate connection to the test section and viewing windows. Each viewing window consists of a single 178 mm (7 in) diameter disk of 6.35 mm (0.25 in) thick polycarbonate mated to the viewing port flanges. This arrangement is shown in Figure 3-2. Stainless steel was selected for corrosion resistance and a compatibility with a wide variety of fluids. Standard pipe sizes and flanges were selected for manufacturability concerns. Polycarbonate was selected for the windows during the commissioning tests due to its machinability and compatibility with saturated water at atmospheric pressure.

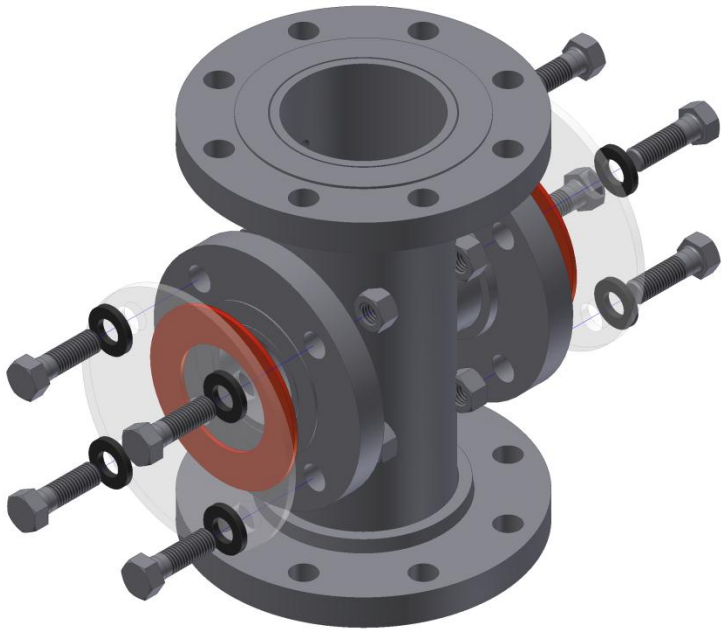

Figure 3-2: Main stainless steel tank assembly showing polycarbonate viewing ports

In order to maintain saturation conditions in the vessel, an external tank heater is used. A 750 W heating tape (Omega DHT051100LD) is wrapped around the tank exterior and the tank assembly is insulated with fibreglass pipe insulation. The heater tape was wrapped around the top half of the tank (above the viewing ports) as the bottom half of the vessel is filled with a ceramic insulator rather than fluid.

3.1.2 Cooling Tank

Attached to the top of the boiling vessel is a cooling tank constructed of 127 mm (5 in) nominal diameter schedule 40 stainless steel T304 piping (OD 141.3 mm, 6.55 mm wall thickness) welded to a 114.3 mm diameter, 6.35 mm (0.25 in) thick stainless steel T304 plate. Additionally, a 12.7 mm (0.5 in) schedule 10 stainless

steel T304 (OD 21.34 mm, 2.77 mm wall thickness) pipe is welded to the steel plate and runs vertically through the tank. This section of pipe vents the tank and acts as a simple condenser. Cool tap water is circulated through the tank via 6.35 mm (0.25 in) PVC tubing connected via ¼ NPT hose fittings located at the top and bottom. A view of this layout is presented in Figure 3-3. Rising steam from the boiling vessel is condensed in this vertical section of the pipe. This prevents the level of fluid in the boiling vessel from dropping during the experiment. In the current design iteration, experiments are conducted at atmospheric pressure; for future work this vent pipe would allow the boiling vessel to be pressurized.

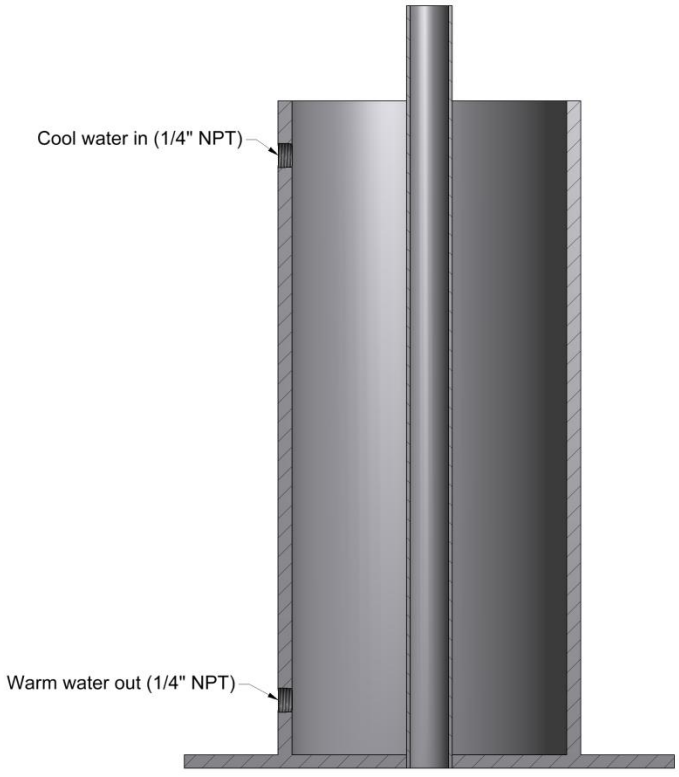

Figure 3-3: Section view of stainless steel cooling tank

3.1.3 Test Section and Heater

The test section and heater are assembled into an ANSI B16.5 150 PSI (1.034 MPa) blind flange. Heat is provided from a cartridge heater and is conducted vertically to the boiling surface through a copper rod. A ceramic insulator is used to limit radial heat loss in the test section. An overview of the assembly is presented in Figure 3-4.

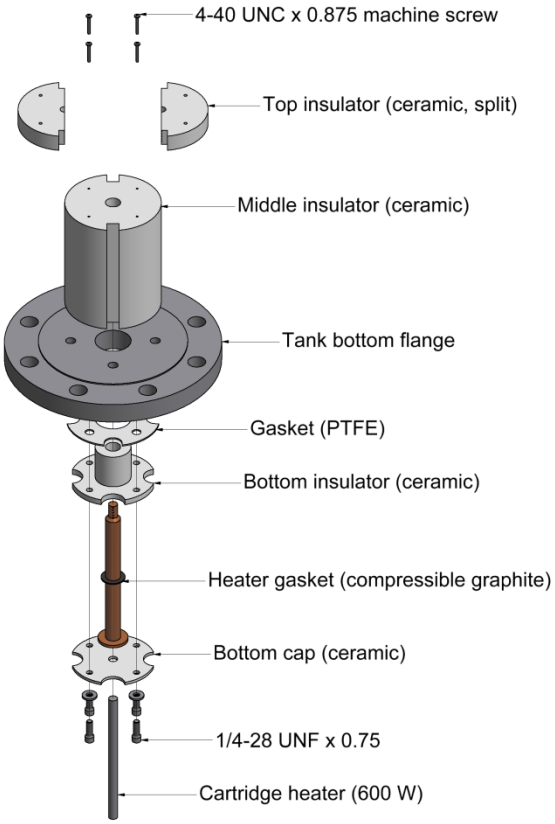

Figure 3-4: Exploded view of test section heater assembly

Heat for the test section is provided from a single 600W stainless steel sheathed 9.53 mm OD x 152.4 mm long (0.375 in x 6 in) cartridge heater (Omega CSH-

206600). The test section is constructed from a single rod of 15.88 mm (0.625 in) diameter C110 copper. Additionally, a 3.78 mm x 31.75 mm OD (1/8" x 1.25") copper disc was brazed to the base of the rod; this provides a surface to seal against the tank internal structures. An overview of the rod geometry is presented in Figure 3-5.

Figure 3-5: Copper rod geometry (dimensions are in inches)

A 9.53 mm (0.375 in) diameter bore at the base of the rod allows for insertion of the cartridge heater. The diameter of the rod is reduced to 9.53 mm (0.375 in) above the heater; this is done to reduce the total required heater power for a given

heat flux at the boiling surface. This narrowed section of copper rod extends approximately 19.1 mm (0.75 in) above the heated section of the rod. Five K-type thermocouples are mounted along this length in order to measure the temperature gradient between the heater and boiling surface. This distance was chosen as a trade-off between minimizing the temperature drop between the cartridge heater and the boiling surface at designed heat fluxes and providing ample space to install the thermocouples. For more details on the test section instrumentation, please refer to section 3.2.

In order to prevent radial heat loss from the copper rod, the test section is mounted in an alumino-silicate ceramic insulator (Aremco 502-1100). This material was selected for ease of machining while being capable of withstanding elevated temperatures (537^{o}C) after heat treatment [23]. The insulator consists of several separate sections as shown in Figure 3-4. The bottom insulator acts as a spacer between the copper test section and the stainless steel flange; a cap made of the same ceramic material holds the copper test section in place. The middle section of the insulator is located at the top of the stainless steel flange. Here, an alumino-silicate sleeve acts both as a thermal insulator and as a means to displace fluid below the viewing window to reduce tank volume. Notches at the side of the sleeve allow for tank drainage and as a passage for thermocouple leads.

The top section of the insulator is split into two; this was done to facilitate permanent mounting of the temperature probes. Details on the temperature probes

are provided in section 3.2.1. Gaps between the copper test section and the ceramic insulator were filled with a high-temperature silicone sealant capable of withstanding temperatures up to 316^{o}C [24].

3.1.4 Heater Control

The applied power to the heaters is controlled by varying the input voltage. Separate variable autotransformers (Tenma 72-110) are used to vary the input voltage to each heater separately between 0 and 130 VAC.

3.2 Measurements and Instrumentation

3.2.1 Test Section Temperature Profile

As discussed in section 3.1.3, five Omega TMTSS-040U K-type sheathed thermocouple probes are mounted in the copper test section between the cartridge heater and the boiling surface at locations shown in Figure 3-5. Relevant specifications are given in Table 3-1. The thermocouple probes were installed at a spacing of 3.18 mm (0.125 in) and at a depth of 4.76 mm (0.188 in) in the test section which corresponds to the centreline of the copper rod.

The probe leads were passed through the tank bottom flange via a multi-conductor feed-through compression fitting (Omega MFT-040-5). The probes were permanently mounted to the copper rod using silver solder; this method was chosen for reduced response time and high reliability once the heater was

assembled. Sheathed thermocouple assemblies were selected for their compatibility with the selected feed-through fittings.

Table 3-1: Temperature probe specifications

Type and Model	Location	Specifications
K-type thermocouple KMTSS-040U	Copper test section	• Stainless steel T304 sheath • 1.02 mm (0.040 in) sheath diameter • Ungrounded tip • Range: $0 < T < 1250^{o}C$ • Accuracy: Greater of $1.1^{o}C$ or 0.4%
T-type thermocouple TMTSS-125G	Boiling vessel fluid Cooling tank fluid	• Stainless steel T304 sheath • 3.18 mm (0.125 in) sheath diameter • Grounded tip • Range: $0 < T < 350^{o}C$ • Accuracy: Greater of $0.5^{o}C$ or 0.4%

3.2.2 Bulk Fluid Temperature

Measurements of the bulk fluid temperature in the boiling vessel are made using two Omega TMTSS-125G T-type sheathed thermocouple temperature probes. Relevant specifications are given in Table 3-1. The probes are sealed and fed through the tank side wall using compression tube fittings (Omega BRLK-18-18). The probes are located at two vertical locations; the first is at the centre of the vessel at the same height as the centre of the viewing port while the second is located at the top of the vessel. The depth of the probes varies as well; the top probe is located at the radial centre of the tank while the lower probe is installed

near the tank wall. This configuration was chosen to minimize interaction of the rising vapour bubbles with the probes.

A third Omega TMTSS-125G T-type thermocouple probe is used to monitor the water temperature in the cooling tank.

3.2.3 Data Acquisition

All experimental measurements are recorded using a National Instruments cDAQ-9178 data acquisition system. The thermocouple probes are measured using a National Instruments NI-9213 thermocouple module operating in high resolution mode. This module is capable of measuring up to 16 thermocouples of different types (J, K, T, E, N, B, R, and S) using an internal cold junction reference at a sampling rate of up to 1 Hz per channel [25]. Relevant specifications are listed in Table 3-2. Temperature measurements were logged once per second.

Applied power to the test section is measured using a National Instruments NI-9205 analog voltage module. Relevant specifications are listed in Table 3-2. The NI-9205 module is capable of measuring voltages in the ±10 V range; therefore a Hammond PT120CF instrumentation transformer (120 VAC primary side, 5 VAC secondary side) is used to step the applied voltage to the heater down to the appropriate range. Additionally a 0.1 Ω resistor (1% tolerance, 5 W) is used as a shunt to measure the applied current. The voltage and current measurements were

calibrated against a Fluke 87 V digital multi meter. Results of this calibration are included in Appendix B on page 96.

Table 3-2: Data acquisition specifications

Type	Model	Specifications
Thermocouple module	NI 9213 16 channel thermocouple module [25]	• K and T thermocouple sensitivity (high resolution mode): 0.02°C • Cold-junction compensation accuracy: 0.8°C typical, 1.7°C maximum • 1 Hz sampling rate per channel (high resolution mode) • Operating temperature range: 0°C < T < 70°C
Voltage module	NI 9205 16 channel differential voltage module [26]	• Sensitivity (± 10 V mode): 96 µV • Absolute accuracy: 6.2 mV • 1 kHz sampling rate per channel • Operating temperature range: -40°C < T < 70°C
Instrumentation transformer	Hammond PT120CF [27]	• Accuracy: 1%
Digital multi meter	Fluke 87 V [28]	• Voltage AC accuracy: ± 0.7% + 2 digits • Operating temperature range: -20°C < T < 55°C

To facilitate the viewing of live data from the temperature and voltage probes while simultaneously recording the measurements to a file, a LabView front end was created; an example screenshot appears in Figure 3-6. The LabView front end displays instantaneous temperature readings from all probes in addition to displaying applied heater power to the test section. Additionally, a temperature versus time plot for the test section probes and a first-order estimate of test section

heat flux is provided as an aid the experimenter. For details on how heat flux was estimated, please refer to Chapter 4, section 4.1.1.

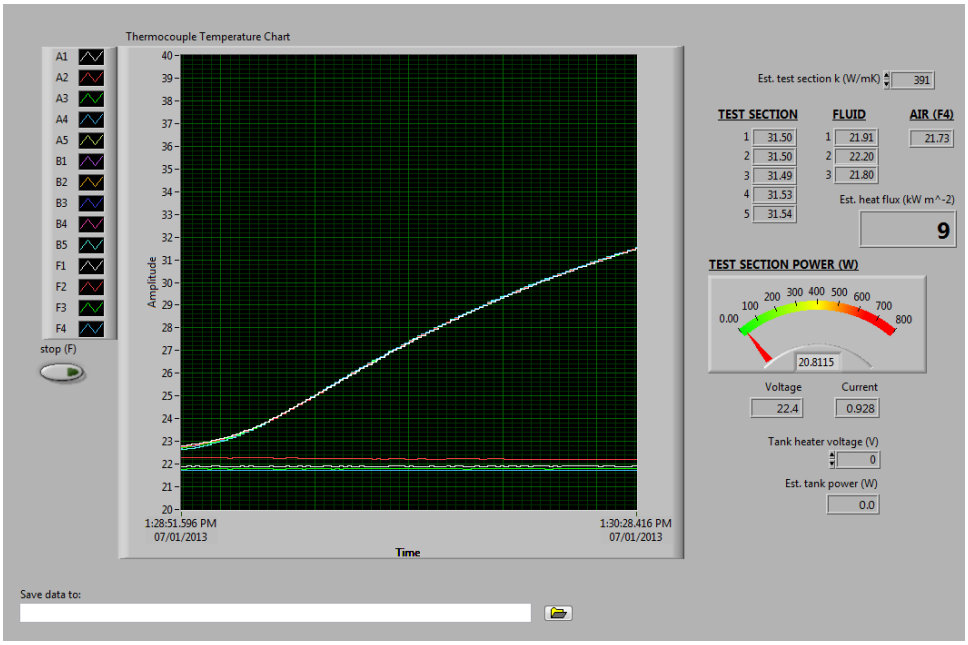

Figure 3-6: LabView front end for displaying live data and data logging

3.2.4 High Speed Video

The dynamics of the boiling process were captured using high speed video. A Photron SA5 high speed camera fitted with a 105 mm macro lens (Nikon Micro-Nikkor 105 mm f/2.8) was utilized. Back-illumination was provided by a single 250 W halogen lamp. A photograph of the arrangement is provided in Figure 3-7.

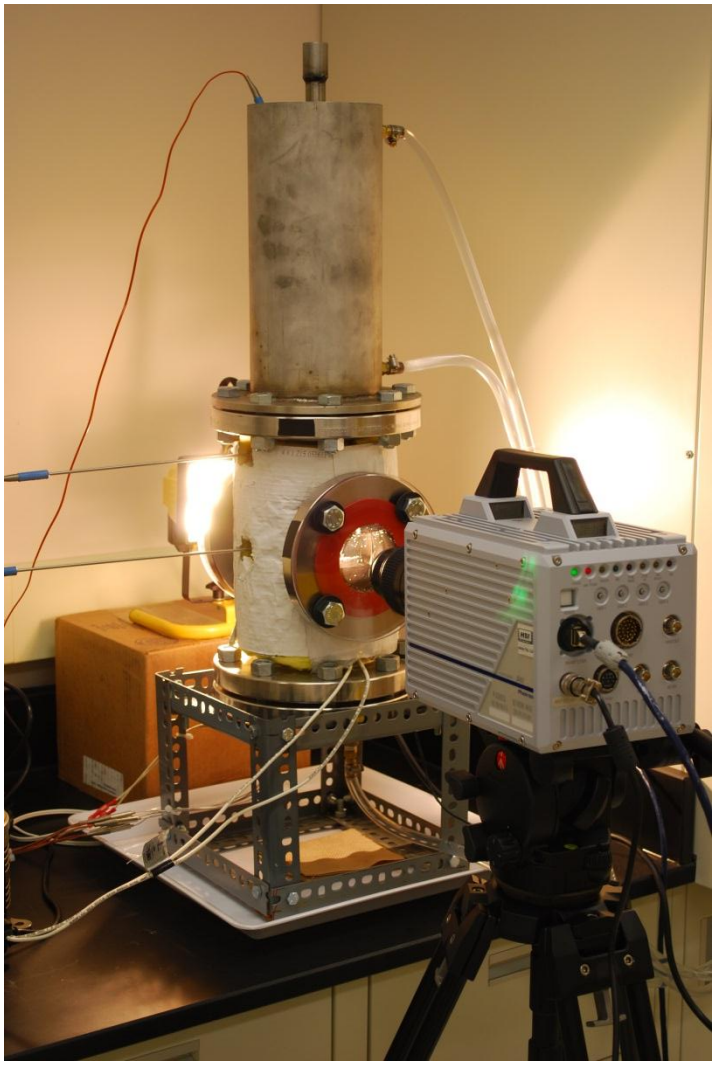

Figure 3-7: Photograph of experimental apparatus showing high speed camera

Images were captured in greyscale at 2500 frames per second and a resolution of 1024 x 640. For the magnification and camera placement employed, the imaging spatial resolution was approximately 39 pixels per mm (1000 pixels per in).

3.3 Experimental Procedures

3.3.1 Boiling Surface and Vessel Preparation

Prior to assembling the tank and following any instance that the tank was drained, the boiling surface was polished and cleaned. Wet-sanding of the top surface of the copper rod was conducted in two steps; first with 1200 grit emery paper followed by 1500 grit emery paper. Following polishing, the surface was flushed with distilled water.

Similarly, the tank interior components were cleaned each time the tank was drained. First, the polycarbonate windows were removed and flushed with distilled water. The tank internal walls and welds were inspected for any oxidation. Any visible oxidation was removed using sandpaper (60 grit). The tank internals were then degreased using acetone. The windows were then re-attached and the tank body bolted to the lower flange containing the test section.

Prior to attaching the cooling tank, the vessel was rinsed by filling with approximately 2 L of room temperature distilled water and then draining. Next, the tank was re-filled with 2 L of room temperature distilled water. Approximately 1 cm of vertical space was kept between the fluid level at room temperature and the top of the vessel to accommodate fluid expansion at elevated temperatures. This gas gap also acted as an insulating layer between the fluid in the cooling tank and the bulk fluid in the vessel. This served to minimize

convective currents resulting from nearly saturated fluid in the boiling vessel being in contact with the base plate of the cooling tank. Finally, the cooling tank was bolted to the top of the vessel and filled with cold tap water.

3.3.2 Boiling Curve Measurement

From a cold start (room temperature), the preheater was first used to bring the bulk fluid temperature to saturation. In the experiments, approximately 500 W of electrical power was applied to the preheater (accomplished by adjusting the preheater autotransformer to a range between 95 V and 100 V). During the preheat stage, the test section applied power remained at 0 W. The preheat stage lasted approximately 90 minutes.

Once the bulk fluid temperature had stabilized at saturation, the test section power was gradually increased. Initially, the power was set to 80 W by adjusting the test section autotransformer and verifying the power level in the LabView front-end. The test section power was held constant while the temperatures were allowed to stabilize. Once stabilized, a high speed video clip of the boiling was captured and saved. The test section power was increased such that the estimated heat flux reported by the LabView front end increased by 50 – 100 $kW \cdot m^{-2}$ and the measurements repeated. This procedure was repeated until near CHF conditions are reached. For the commissioning tests conducted with distilled water, the test section heat flux was kept below 1200 $kW \cdot m^{-2}$. Please refer to section 4.1.3 for more details on this CHF prediction.

Throughout the experiment, the temperature of the tap water in the upper cooling tank was simultaneously monitored. Cold water was not continuously circulated through the cooling tank; the drain valve was closed and the tank was filled with cold tap water. The PVC tubing connected to the tank is rated up to 65^{o}C; as such, the tank was drained and refilled with cold tap water once the water at the base of the cooling tank was seen to reach 60^{o}C. It is desirable to maintain the water temperature in the cooling tank as high as possible to minimize the effect of any convective currents caused by a large temperature differential between the boiling vessel and the cooling tank.

Chapter 4

Results and Analysis

Commissioning tests of the boiling facility were conducted using distilled water over several days. In each case, the tank was at atmospheric pressure and held at saturation conditions. To provide an example of studying modified heater surface conditions, data was collected for both emery polished copper heater surfaces and oxidized copper surfaces. The oxidized heater surfaces were created using the polished surface boiling experimental runs in addition to leaving the filled tank and heater at ambient conditions for one to four days.

4.1 Data Analysis Methodology

To simplify the data analysis, several assumptions were made:

- Due to the presence of the insulating sleeve along the radial ends of the test section, heat loss in the radial direction was assumed to be negligible. Therefore, heat flux in the test section was assumed to be one-

dimensional in the vertical direction. The validity of this assumption is verified in section 4.3.1.

- All heat conducted through the vertical rod at the top of the test section was assumed to be transferred to the pool.
- The thermal conductivity of the test section was assumed to be constant and corresponding to the value seen near the boiling interface. The impact that this assumption had on the results is examined in section 4.2.4.
- Uncertainties in the temperature measurements which were introduced by the data acquisition system were assumed to be a result of the cold-junction compensation (CJC) error rather than sampling error. This assumption is supported by the data presented in Table 3-2 where the CJC error is specified to be 40 – 90 times the measurement sensitivity.
- Heat flux and wall temperature predictions were made from data assumed to represent steady state behaviour. Experimental measurements were averaged over 20 seconds to reduce the impact of random fluctuations resulting from noise in the readings and temperature variations from bubbles departing the boiling surface.

A MATLAB script was created to process the raw experimental temperature measurements. This script was used to apply calibration data to the temperature probe measurements, estimate bulk fluid temperatures, calculate heat flux and heater wall temperature from temperature profile data, and propagate

experimental uncertainties. Details of these calculations are discussed in the following sections.

4.1.1 Heat Flux and Wall Temperature Estimation

The heat flux through the test section is estimated using Fourier's Law of conduction. Given the thermal conductivity *k* and a temperature gradient ∇T, and no internal heat generation, the heat flux $\overrightarrow{q''}$ is given by [29]:

$$\overrightarrow{q''} = -k\nabla T \tag{4.1}$$

Due to the presence of the ceramic insulator around the radial ends and base of the test section, heat flux is assumed to be one dimensional in the vertical direction. Applying this assumption, Equation 4.1 simplifies to:

$$q_z'' = -k\frac{dT}{dz} \tag{4.2}$$

4.1.1.1 Temperature Gradient

From equation 4.2, given a constant heat flux through the test section (no radial heat loss) and a constant thermal conductivity *k*, the temperature gradient $\frac{dT}{dz}$ is constant; this implies a linear temperature drop. Five equally spaced temperature probes were installed along the test section. The temperature gradient was estimated from the steady state temperature data using a least squares fit to a straight line.

For a given set of steady-state temperature *T* versus position *z* data, a least squares fit to a straight line was performed. Given a straight line in the form $T = a + bz$, the fit parameters can be calculated using the method of determinants to be [30]:

$$a = \frac{1}{\Delta}\left(\sum \frac{z_i^2}{\sigma_{T_i}^2} \sum \frac{T_i}{\sigma_{T_i}^2} - \sum \frac{z_i}{\sigma_{T_i}^2} \sum \frac{z_i T_i}{\sigma_{T_i}^2}\right) \tag{4.3}$$

$$b = \frac{1}{\Delta}\left(\sum \frac{1}{\sigma_{T_i}^2} \sum \frac{z_i T_i}{\sigma_{T_i}^2} - \sum \frac{z_i}{\sigma_{T_i}^2} \sum \frac{T_i}{\sigma_{T_i}^2}\right) \tag{4.4}$$

$$\Delta = \sum \frac{1}{\sigma_{T_i}^2} \sum \frac{z_i^2}{\sigma_{T_i}^2} - \left(\sum \frac{z_i}{\sigma_{T_i}^2}\right)^2 \tag{4.5}$$

The resulting slope *b* from Equation 4.4 was taken as an estimate of the temperature gradient.

4.1.1.2 Wall Temperature Estimation

For the least-squares fit to a straight line method, the fit parameter *a* from Equation 4.3 is taken as the estimate of wall temperature.

4.1.1.3 Test Section Thermal Conductivity

As stated in section 4.1, the thermal conductivity *k* is assumed to be constant along the vertical test section for a given set of steady state temperature data and corresponding to the temperature at T_1. Values for pure copper were obtained from NIST and the relevant temperature range shown in Figure 4-1 [31]. Linear interpolation was used for temperature values between the provided data points.

Given the interpolated thermal conductivity *k* and the temperature gradient $\frac{dT}{dz}$, Equation 4.2 is used to calculate the test section heat flux.

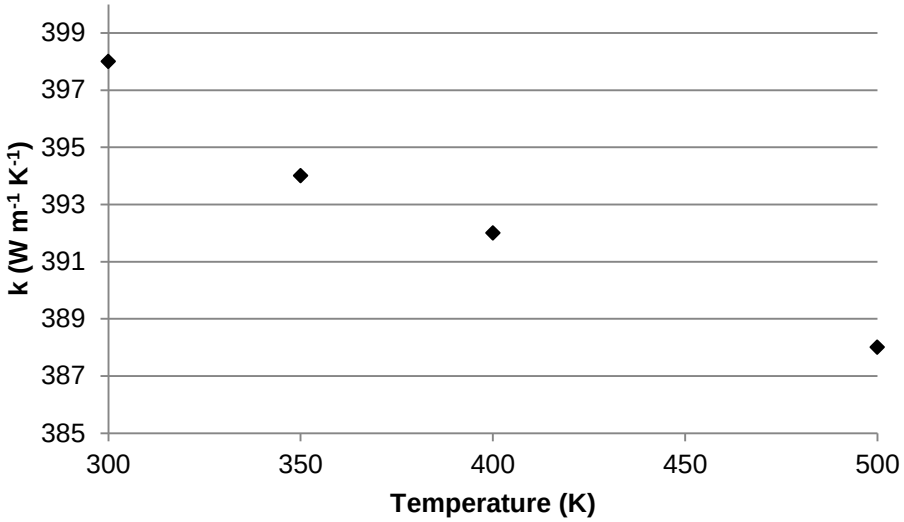

Figure 4-1: Thermal conductivity for pure copper [31]

4.1.2 Bulk Fluid Temperature

As discussed in section 3.2.2, two temperature probes were used to monitor the bulk fluid temperature at two locations during the boiling tests. The average of these two temperature readings for a set of steady-state temperature data was used to estimate the bulk fluid temperature. The bulk fluid temperature was subtracted from the test section wall temperature estimation to obtain the test section wall superheat ΔT_{wall}.

4.1.3 Critical Heat Flux (CHF) Prediction

In performing the commissioning experiments, it was desired to remain below the critical heat flux to prevent damage to the test section surface. As discussed in section 1.1.2.3, the modified Zuber correlation was used (Equations 1.3 through 1.5 and Table 1.1). Given the properties of saturated water at 1 atm and a flat plate heater of diameter D = 9.53 mm [32]:

$$D' = \frac{D}{\left[\frac{\sigma}{g\left(\rho_f - \rho_g\right)}\right]^{1/2}} \tag{1.4}$$

$$D' = \frac{9.53\times10^{-3}\ m}{\left[\frac{5.892\times10^{-2}\ \frac{N}{m}}{9.81\ \frac{N}{kg}\left(958.4\ \frac{kg}{m^3} - 5.976\times10^{-1}\frac{kg}{m^3}\right)}\right]^{1/2}}$$

$$D' = 3.80$$

Based on this characteristic dimension and referring to Table 1.1, the relevant multiplier to the Zuber correlation is 1.14. Referring to Equation 1.3:

$$q''_{CHF} \cong K h_{fg} \rho_g^{1/2} \left[g\sigma\left(\rho_f - \rho_g\right)\right]^{1/4}$$

$$q''_{CHF} \cong$$

$$\left(1.14 \times \frac{\pi}{24}\right)\left(2.257 \times 10^3\ \frac{kJ}{kg}\right)\left(5.976 \times 10^{-1}\ \frac{kg}{m^3}\right)^{1/2}\left[\left(9.81\ \frac{N}{kg}\right)\left(5.892 \times 10^{-2}\ \frac{N}{m}\right)\left(958.4\ \frac{kg}{m^3} - 5.976 \times 10^{-1}\ \frac{kg}{m^3}\right)\right]^{1/4}$$

$$q''_{CHF} \cong 1260 \ \frac{kW}{m^2}$$

Therefore, in conducting the tests the heat flux was not permitted to exceed 1200 $kW \cdot m^{-2}$

4.2 Sources of Error

In order to estimate the standard deviation σ in the calculated heat flux and wall temperature measurements, the uncertainties in the temperature measurements are propagated using the following equation [30]:

$$\sigma_x^2 \cong \sigma_u^2 \left(\frac{\partial x}{\partial u}\right)^2 + \sigma_v^2 \left(\frac{\partial x}{\partial v}\right)^2 + \cdots \tag{4.6}$$

Note that Equation 4.6 assumed co-variance terms are insignificant by assuming that variables are un-correlated. The resulting measurement uncertainties for a 95% confidence interval (2σ error) are summarized in Table 4-1.

Table 4-1: Measurement uncertainties for a 95% (2σ) confidence interval

Measurement	Uncertainty sources and value
Test section temperatures	• NI-9213 (cold junction error) • RTD calibration (sample variance) • ±0.5°C (22°C < T < 228°C)
Bulk fluid temperatures	• NI-9213 (cold junction error) • RTD calibration (sample variance) • ±0.5°C (22°C < T < 150°C)
Wall superheat	• Linear best fit to test section temperature profile • Bulk fluid temperature measurement • ±0.6°C (0°C < $T_{wall} - T_{bulk}$ < 20°C)
Heat flux	• Linear best fit to test section temperature profile • Test section temperature measurements • ± 20 kW·m^{-2} (q'' < 1200 kW·m^{-2})

4.2.1 Temperature Measurement Uncertainty

The instrumentation uncertainty data was first introduced in Table 3-1 and Table 3-2 in section 3.2. As described in Appendix A, prior to installation in the test section, each thermocouple probe was calibrated against a precision RTD thermometer. A least-squares fit to a straight line in the form $T = a + bT_{cal}$ was performed for each set of un-calibrated temperature (T) versus calibrated temperature (T_{cal}) data. The uncertainty in the reference temperature readout was stated to be 0.025°C and deemed insignificant with respect to the uncertainty in the un-calibrated temperature.

Following the calibration, the 1σ uncertainty in the temperature measurement was taken to be $\pm 0.25^{o}$C; this was based on an assumption that the calibrated instrumentation would have at best an accuracy one order of magnitude lower than the reference instrumentation. This was confirmed with comparison of the sample variance of the fitted calibration curves; for further details refer to Appendix A on page 87.

As noted in section 4.1, steady state temperature data was computed as a moving average over 20 seconds:

$$\overline{T_{cal}} = \frac{1}{N}\sum_{i=1}^{N} T_{cal_i} \tag{4.7}$$

Additionally, the sample standard deviation s of the averaged data set was determined using [30]:

$$s_{\overline{T_{cal}}} = \left[\frac{1}{N-1}\sum\left(T_{cal_i} - \overline{T_{cal}}\right)^2\right]^{1/2} \tag{4.8}$$

The larger numerical result of 0.25^{o}C (calibrated temperature uncertainty) and Equation 4.8 and was taken to be the 1σ uncertainty in the average temperature.

4.2.2 Temperature Gradient Uncertainty

As described in section 4.1.1.1, the temperature gradient was determined using Equations 4.3 through 4.5. The variances in the fit parameters were determined

using Equation 4.9; the 1σ uncertainty is taken to be the square root of the variance. [30]

$$\sigma_a^2 = \frac{1}{\Delta}\sum\frac{z_i^2}{\sigma_{T_i}^2} \text{ and } \sigma_b^2 = \frac{1}{\Delta}\sum\frac{1}{\sigma_{T_i}^2} \tag{4.9}$$

4.2.3 Wall Temperature Uncertainty

The uncertainty in the predicted wall temperature has two major components: uncertainty in the least squares linear fit to the temperature data and uncertainty in the distance between the boiling surface and the thermocouples. Equation 4.9 shows the calculation of the variance of the best fit parameters; σ_a or the uncertainty in the best-fit intercept is taken to be one component of the uncertainty in the wall temperature.

Between experimental runs, the test section was polished. This effectively reduced the distance between the boiling surface and the thermocouples. Since the thermocouple spacing was not affected by the surface polishing, this action impacted the wall temperature prediction and not the estimation of the temperature gradient.

Due to the integrated nature of the test section in the insulator, it was not practical to measure the change in vertical distance each time that the surface was polished. Following the experiments, the insulator was disassembled and the thermocouple distance measured to be 1.4 mm (0.055 in), a 0.13 mm (0.005 in) decrease from the original distance. Between manufacturing and the final distance measurement,

five polishing operations had taken place. It was assumed that each operation removed approximately 0.025 mm (0.001 in) material from the test section. Data collected between polishing operations was assumed to have identical thermocouple positioning.

The positional uncertainty of the thermocouple (resulting from measuring error) was taken to be 0.025 mm (0.001 in). Given the slope b from equation 4.4 this positional uncertainty was translated to an uncertainty in the wall temperature using:

$$\sigma_{T_{wall,polishing}} = b \times 2.5 \times 10^{-5}\, m \tag{4.10}$$

Using Equation 4.6, this uncertainty was combined with uncertainty in wall temperature σ_a as calculated from Equation 4.9.

4.2.4 Heat Flux Uncertainty

The assumption that thermal conductivity is constant in the test section introduces an error since the thermal conductivity of copper does decrease with increasing temperature. In the experimental data at high heat fluxes, the test section temperature gradient was at highest about 40^{o}C. Using the data presented in section 4.1.1.3 and a typical temperature difference for high heat flux (>1 MW/m^2) the variation in thermal conductivity of copper for this case is approximately determined below:

$$\Delta k_{Cu} = k_{Cu,T1} - k_{Cu,T5}$$

$$\Delta k_{Cu} = k(122.89℃) - k(161.97℃)$$

$$\Delta k_{Cu} = 392.2 \frac{W}{m \cdot K} - 390.6 \frac{W}{m \cdot K}$$

$$\Delta k_{Cu} = 1.6 \frac{W}{m \cdot K}$$

This bounding case represents a maximum variation of 0.4% from the assumed value. The 1σ uncertainty in the temperature gradient calculated from the best fit to the temperature profile was constant at $\pm 25^{o}C \cdot m^{-1}$, which corresponds to a relative uncertainty of 1% to 10% for the experimental data. Therefore, it was assumed that the variation of thermal conductivity with temperature in the test section did not introduce significant error into the result and this effect was not included. Therefore, given the uncertainty in the temperature gradient σ_b, the uncertainty in calculated heat flux was calculated using:

$$\sigma_{q''} = k_{Cu,T1} \times \sigma_b \tag{4.11}$$

4.3 Experimental Results

4.3.1 Thermocouple Linearity

As discussed in section 4.1.1, the temperature drop across the test section is expected to be linear for the one dimensional case. The linearity of the temperature measurements with respect to position were verified by plotting

measured temperature versus vertical position. This was done to confirm good thermal contact of the thermocouples with the test section and to verify minimal heat loss in the radial direction along the test section length.

The temperature data consistently showed good linearity consistently throughout the experiment at all probe locations. This is demonstrated in Figure 4-2 where temperature profiles for high, medium, and low heat fluxes on the first test day are presented. Parameters from the least squares fit are also presented for each case. To demonstrate continued good thermal contact and insulation of the test section throughout the duration of the tests, temperature profiles from similar heat fluxes on the final day of testing are presented in Figure 4-3. Additionally, sample temperature profiles from each test day are presented in Appendix C on page 101.

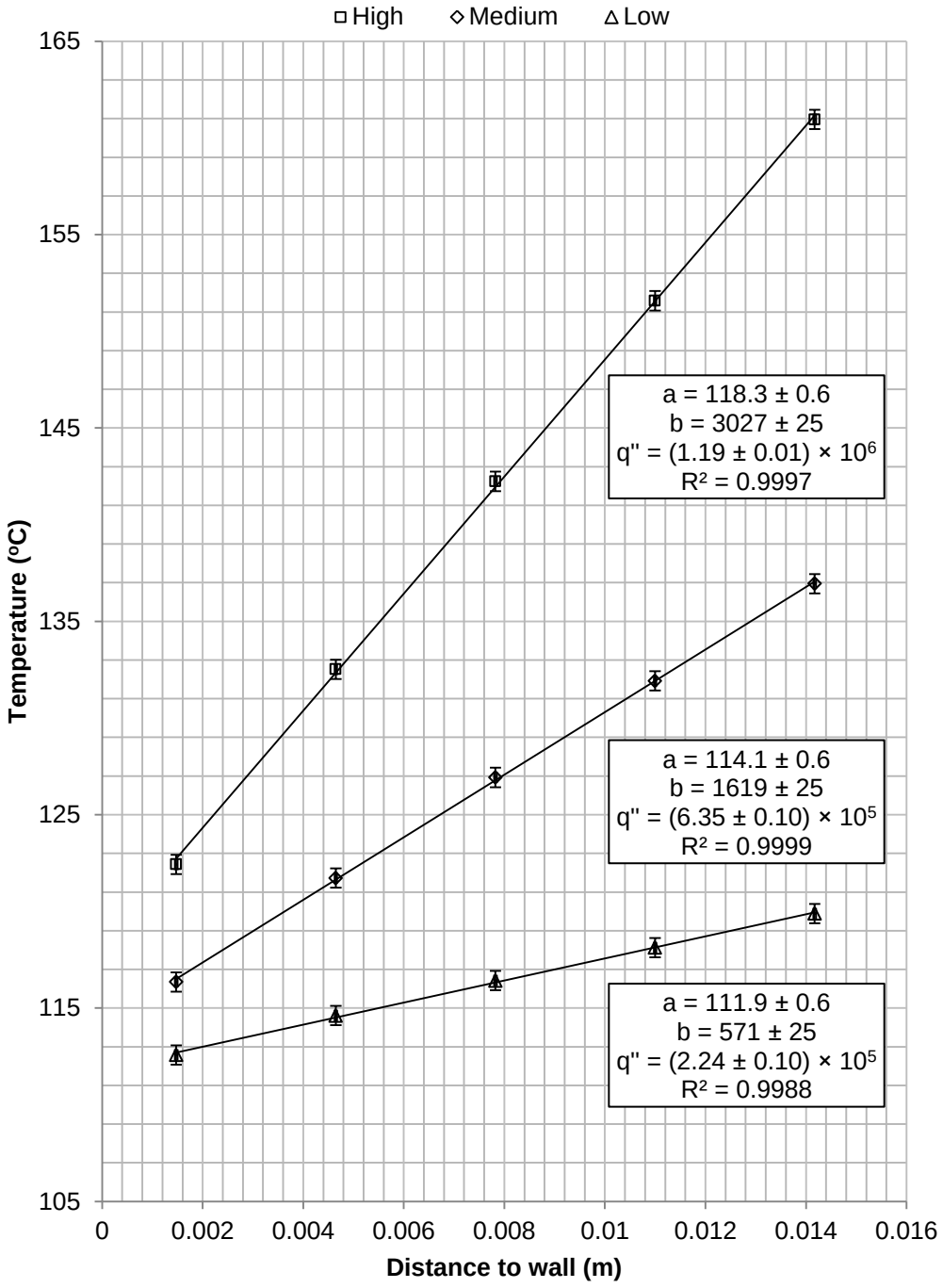

Figure 4-2: Sample temperature gradient data from 13/08/2012. For each linear fit: *a* is the predicted wall temperature (^{o}C), *b* is the fitted slope (^{o}C·m^{-1}), and *q″* is the corresponding heat flux (W·m^{-2})

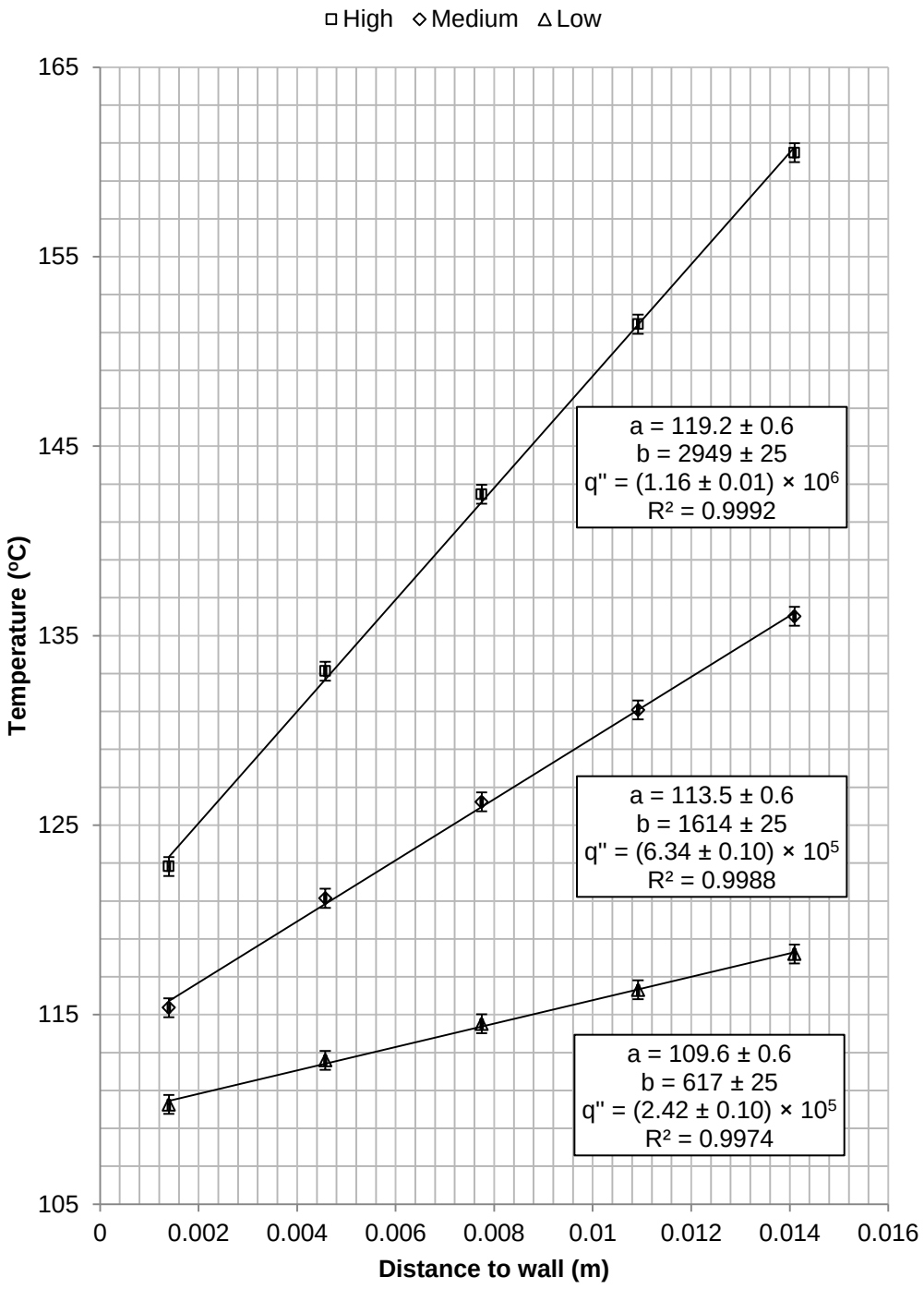

Figure 4-3: Sample temperature gradient data from 20/09/2012. For each linear fit: *a* is the predicted wall temperature (^{o}C), *b* is the fitted slope (^{o}C·m^{-1}), and *q″* is the corresponding heat flux (W·m^{-2})

4.3.2 Comparison to Rohsenow Correlation

The results for heat flux versus wall superheat were collected and plotted. Additionally, the experimental data was compared against the Rohsenow correlation:

$$q'' = \mu_f h_{fg} \left[\frac{\sigma}{g\Delta\rho}\right]^{-\frac{1}{2}} \left(\frac{1}{C_{sf}}\right)^{\frac{1}{r}} \cdot \mathrm{Pr}^{-\frac{s}{r}} \left[\frac{c_p(T_w - T_{sat})}{h_{fg}}\right]^{\frac{1}{r}} \quad (1.2)$$

The correlation was evaluated using data for saturated water at 1 atm [32]. As recommended for water, r was set to 0.33 and s was set to 1 [5]. The correlation was plotted for two C_{sf} values: 0.011 and 0.013. For comparison, saturated water at atmospheric pressure on emery polished copper surfaces, a C_{sf} value of 0.0128 has been recommended; this corresponds to a wall superheat range of 5.5 – 15.5^{o}C and heat fluxes between 28 and 530 kW·m^{-2} [33].

The experimental data was separated into two groups: data for a freshly polished boiling surface and data collected on an unpolished surface (oxidized by a previous pool boiling experiment). The former is presented in Figure 4-4 and the latter is presented in Figure 4-5.

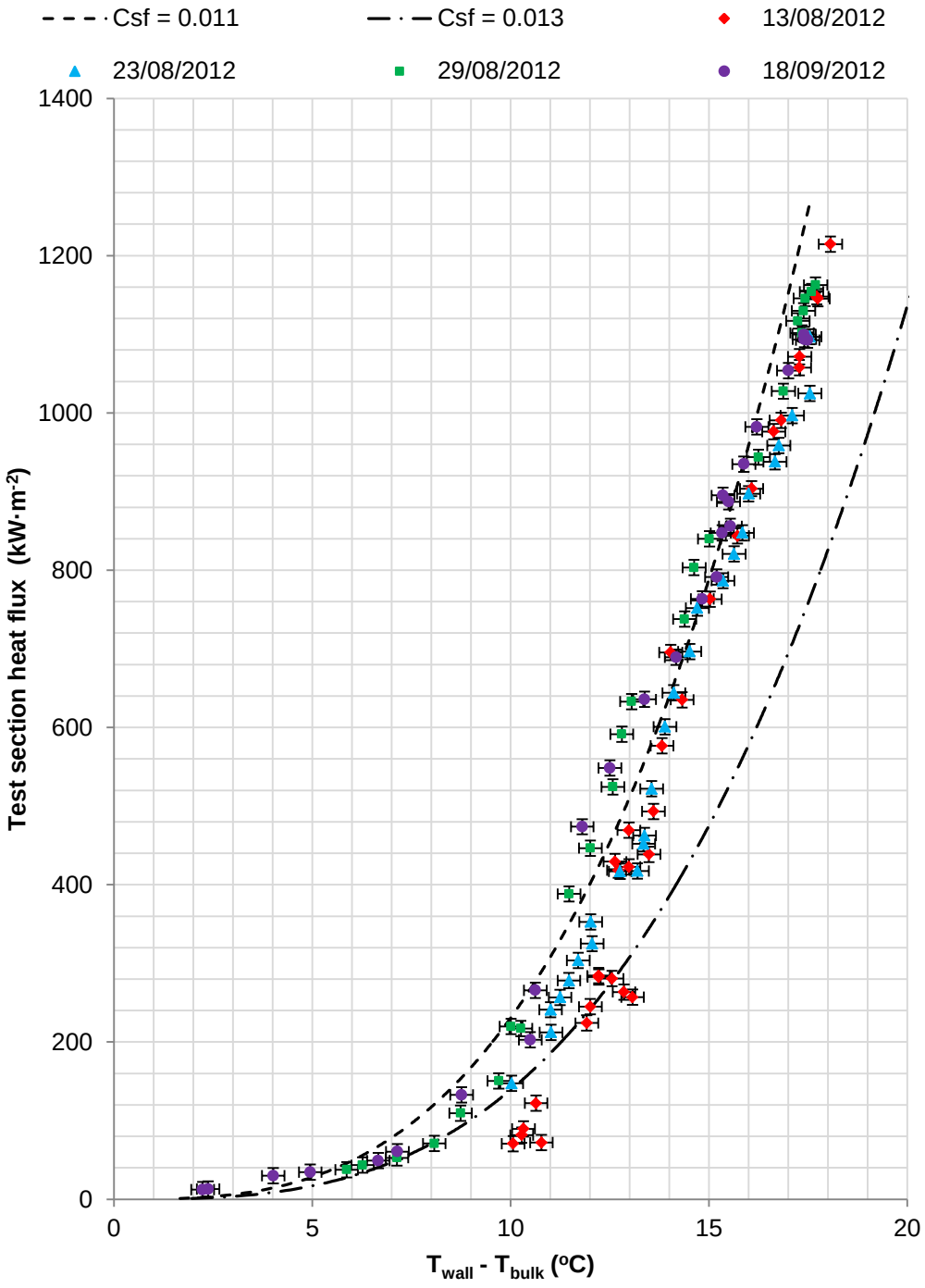

Figure 4-4: Measured heat flux versus wall superheat for polished surfaces. The dashed lines follow the Rohsenow nucleate boiling correlation for saturated water at 1 atm and the indicated value of C_{sf}.

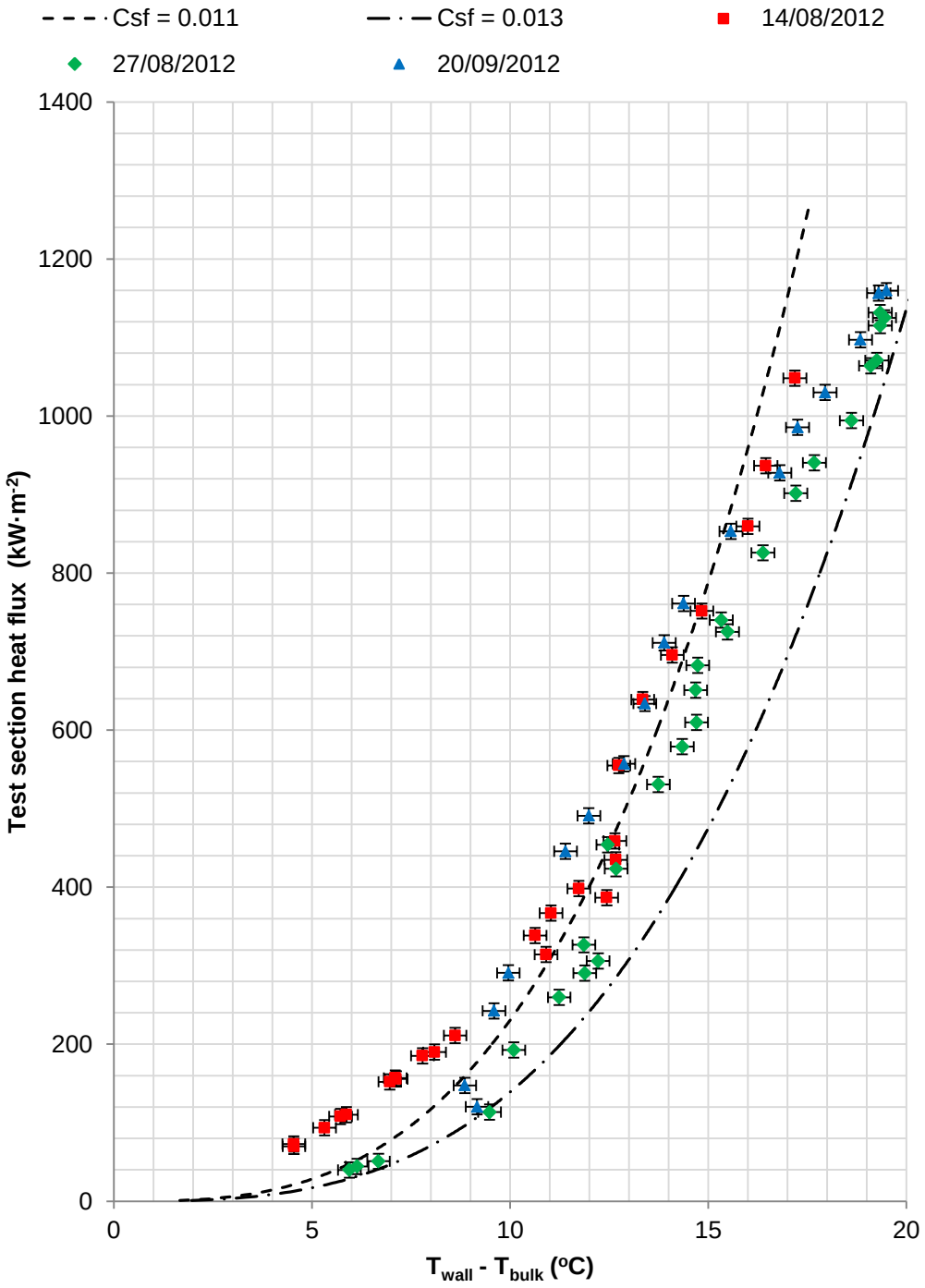

Figure 4-5: Measured heat flux versus wall superheat for unpolished surfaces. The dashed lines follow the Rohsenow nucleate boiling correlation for saturated water at 1 atm and the indicated value of C_{sf}.

4.3.2.1 Polished heater surfaces

For polished boiling surfaces, it was observed that results at high heat fluxes were repeatable day-to-day while a greater spread in results was observed for mid- and low heat fluxes; this is illustrated in Figure 4-4. The data suggests that during the boiling process, the surface conditions at the boiling interface were modified. This was expected as the boiling process was observed to cause discoloration and oxidation of the copper surface, as shown in Figure 4-6. At lower heat fluxes (below 400 $kW \cdot m^{-2}$), the results more closely followed the Rohsenow correlation with C_{sf} = 0.013 while at higher heat fluxes (above 700 $kW \cdot m^{-2}$), the data more closely follows C_{sf} = 0.011.

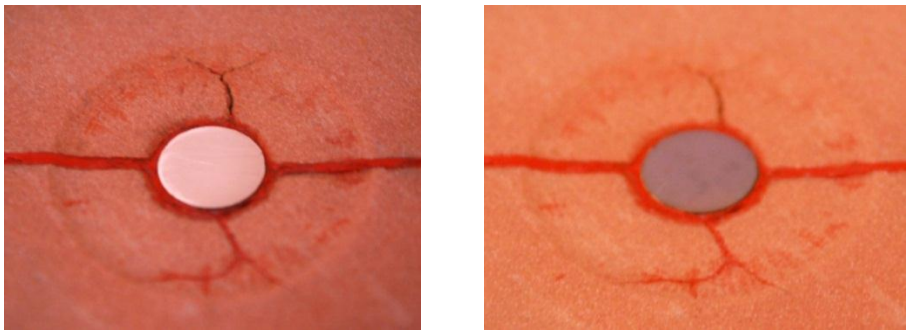

a) b)

Figure 4-6: Polished surface (a) compared to surface after boiling in distilled water (b). The discoloration of the surface is a result of oxidation caused by the boiling process.

4.3.2.2 Unpolished heater surfaces

Data collected for boiling on unpolished surfaces is shown in Figure 4-5. In general, at high heat flux levels, the recorded wall temperature was higher than observed for polished surfaces indicating poorer heat transfer.

For unpolished surfaces, there is a larger spread in the observed boiling curve data. This is likely a result of the surface preparation of the boiling surface being less controlled than for the polished surface boiling cases. The data displayed in Figure 4-5 was collected by repeating the experiment using the same surface preparation and water from a previous day's polished heater experiment. Since the duration of each experiment was not carefully controlled, varying amounts levels of heater oxidation could have occurred following each experimental run using a polished heater. Additionally, the number of days elapsed between "polished" and "unpolished" experiments was not carefully controlled. Time elapsed between runs varied between 1 day (14/08/2012 data), 2 days (20/09/2012 data), and 4 days (27/08/2012 data). A longer delay between experiments may have resulted in a higher level of surface oxidation. This would result in a different value of C_{sf} to be used in the Rohsenow correlation for a valid comparison.

4.3.3 Measurements at Low Heat Flux

It was noted during the commissioning tests that it was difficult to obtain repeatable measurements at low heat flux levels and that the results gathered near

the onset of nucleate boiling (ONB) point were dependent on experimental procedure. This is more clearly shown in Figure 4-7. The difficulties also may have resulted from the relatively coarse adjustments possible using the variable autotransformers at low power levels.

In the discussion of the boiling curve in Chapter 1, section 1.1.2, it was noted that the boiling curve exhibits a discontinuity at ONB; specifically ONB may occur at wall superheats higher than required to sustain nucleate boiling. If the heater power is initially low and gradually increased in the natural convection region, the wall temperature will rise to the point where nucleation sites begin to activate. If the discontinuity in the boiling curve is large and heat flux is held constant, a sharp decline in wall temperature may be observed [5]. Additionally, if applied power to the heater is decreased causing a gradual cool-down of the test section, nucleate boiling could be sustained at lower wall temperatures.

Experimental procedure at low heat flux levels varied between the 13/08/2012 and 14/08/2012 data sets. On 13/08/2012, the heater power was gradually increased in steps from zero until nucleation was observed at $\Delta T_{wall} \approx 10^{o}$C and $q'' \approx 100$ kW·m^{-2}. Following this observation, heater power was increased further to obtain the remaining data for the boiling curve shown in Figure 4-7. As on the previous day, the heater power was gradually increased in steps from zero on 14/08/2012. However, once ONB had occurred, the heater power was lowered in steps to test whether nucleate boiling could be sustained at lower levels of wall

superheat. The outlying data points from 14/08/2012 in Figure 4-7 correspond to these measurements. The heater power was then raised in steps as before to measure the remainder of the boiling curve.

Comparing the high speed video from the two data sets, it is observed that fewer nucleation sites were active for the low heat flux/high wall superheat cases recorded on 13/08/2012 when compared to the low heat flux/low wall superheat cases recorded on 14/08/2012. Example video frames taken at a measured heat flux of approximately 100 $kW \cdot m^{-2}$ are presented in Figure 4-8.

From the 13/08/2012 footage, the majority of the active nucleation sites are located at the perimeter of the boiling surface; one centrally located nucleation site was producing approximately one bubble per 80 ms; this corresponds to the onset of nucleate boiling. Comparatively, the 14/08/2012 footage taken at the lowered heater power following the ONB point shows numerous centrally located nucleation sites producing vapour bubbles more frequently. The lower wall superheat in this case is a result of the improved heat transfer resulting from nucleate boiling. This highlights the impact that procedural variations may have on measurements near ONB. Additionally, this highlights the necessity of studying bubble dynamics alongside heat flux and wall temperature measurements.

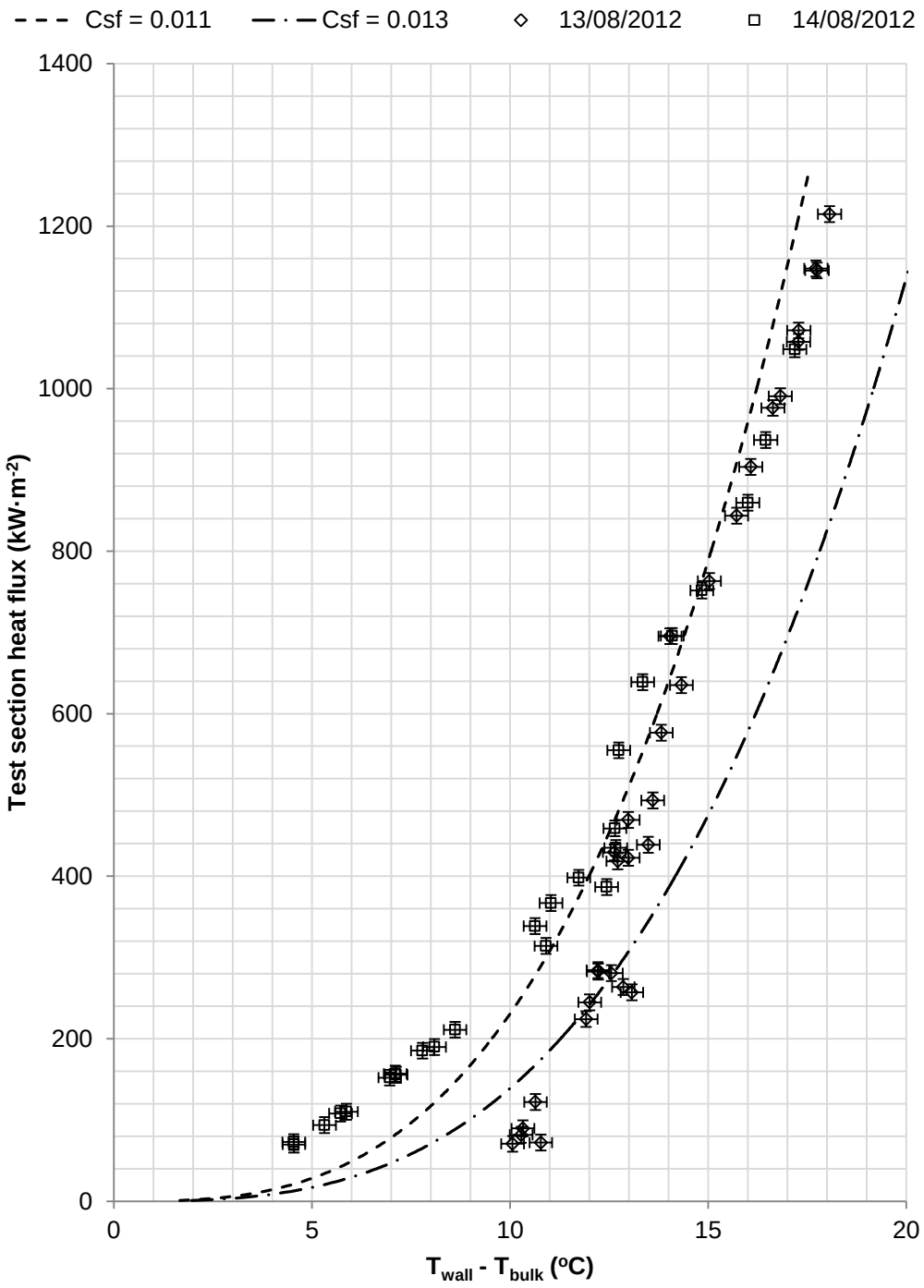

Figure 4-7: Measured heat flux versus wall superheat for 13/08/2012 (polished heater) and 14/08/2012 (unpolished heater) data sets.

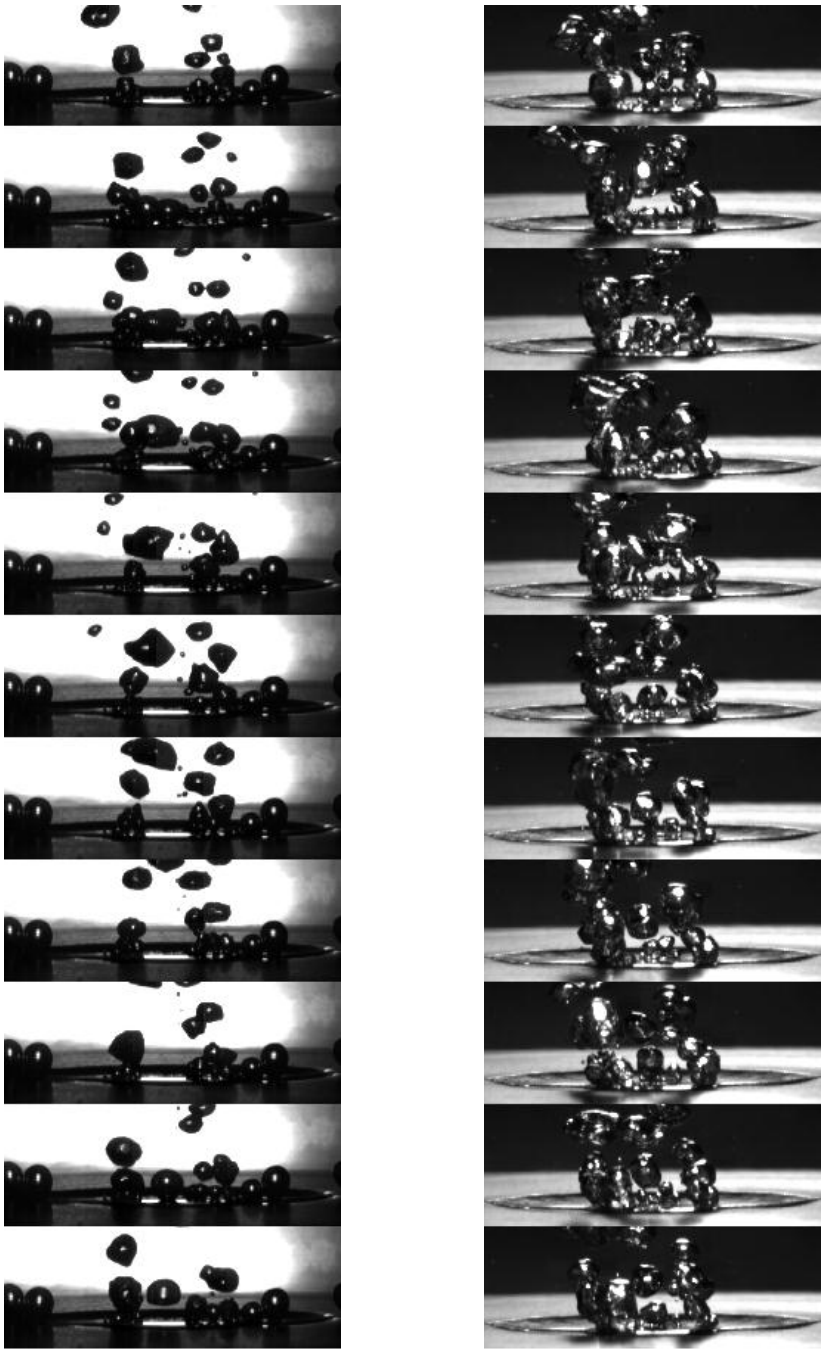

a) ΔT_{wall} = 10.3 ± 0.6 °C
q'' = 90 ± 20 kW·m^{-2}
Heater power = 96 W

b) ΔT_{wall} = 5.9 ± 0.6 °C
q'' = 110 ± 20 kW·m^{-2}
Heater power = 75 W

Figure 4-8: Example high speed video frames from 13/08/2012 (a) and 14/08/2012 (b). Footage shot at 2500 FPS, every 20th frame shown (Δt = 8 ms)

4.4 Bubble Dynamics

The bubble dynamics were captured using high speed video as detailed in section 3.2.4. Sample frames captured at low, medium, and high heat fluxes are shown in Figure 4-9, Figure 4-10, and Figure 4-11, respectively. The high speed video footage was used to qualitatively compare the bubble dynamics between experimental runs at similar heat flux levels. An example comparison is conducted in section 4.3.3.

A full quantitative analysis of the bubble statistics is slated as future work for this experimental program. Such an analysis could be performed through image processing software which would track vapour bubbles as they are formed, grow, and depart from the heater surface. From this, bubble departure size and frequency would be obtained. Currently there are several difficulties in performing this analysis. First, following the activation of several nucleation sites, the overlapping vapour bubbles made it difficult to track the activity at the various sites. Additionally, at higher heat fluxes such as those seen in Figure 4-10, the heater surface becomes obscured by the coalescing vapour bubbles before their departure. A potential remedy to this problem would involve the use of a sheet later to illuminate a single plane of bubbles. This is further discussed in Chapter 5, section 5.2.1.

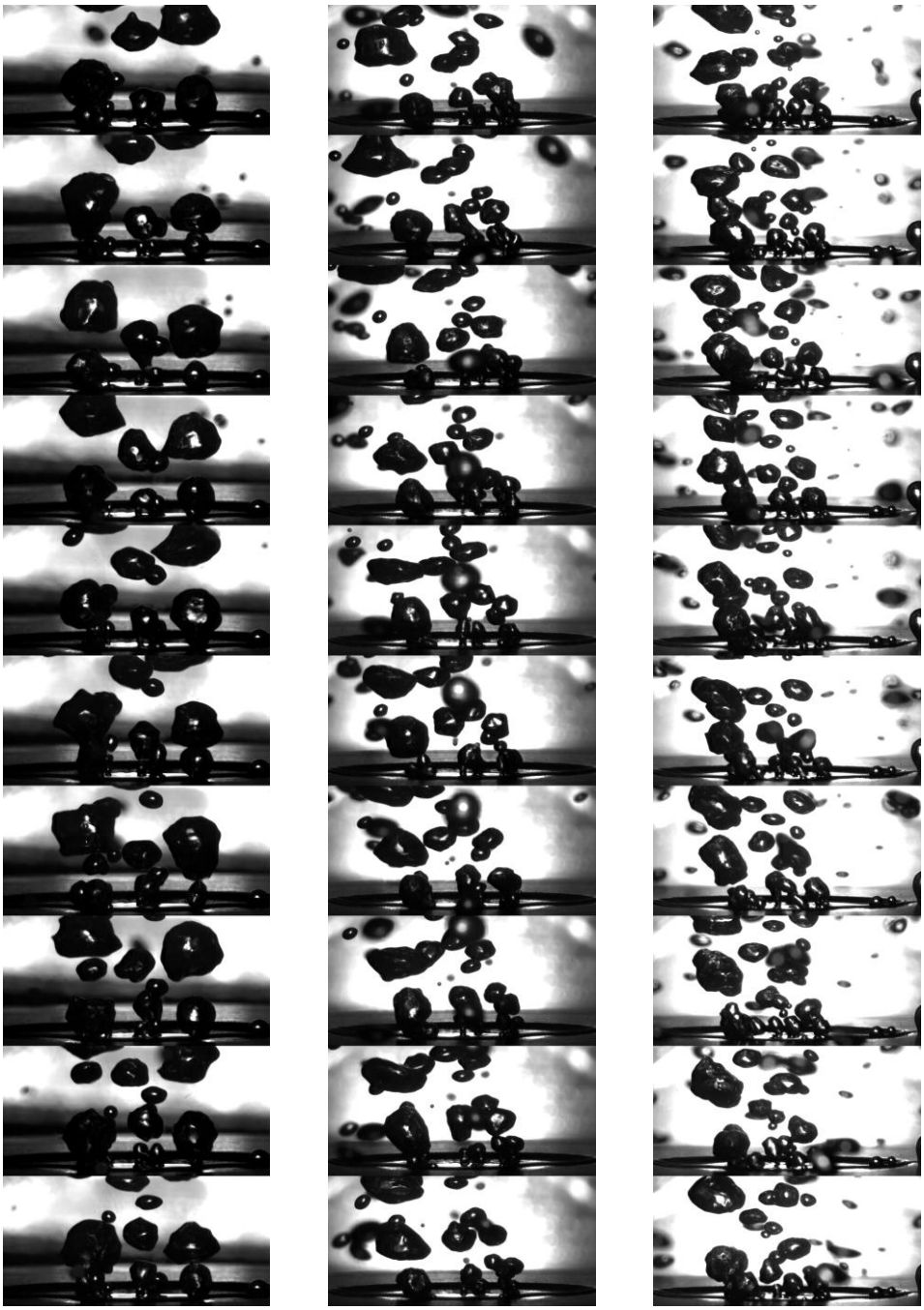

a) ΔT_{wall} = 10.0 ± 0.6 °C, q'' = 150 ± 20 kW·m^{-2}
b) ΔT_{wall} = 9.5 ± 0.6 °C, q'' = 110 ± 20 kW·m^{-2}
c) ΔT_{wall} = 8.8 ± 0.6 °C, q'' = 130 ± 20 kW·m^{-2}

Figure 4-9: Example high speed video frames at low heat flux, from 23/08/2012 (a), 27/08/2012 (b), and 18/09/2012 (c). Footage shot at 2500 FPS, every 20th frame shown (Δt = 8 ms)

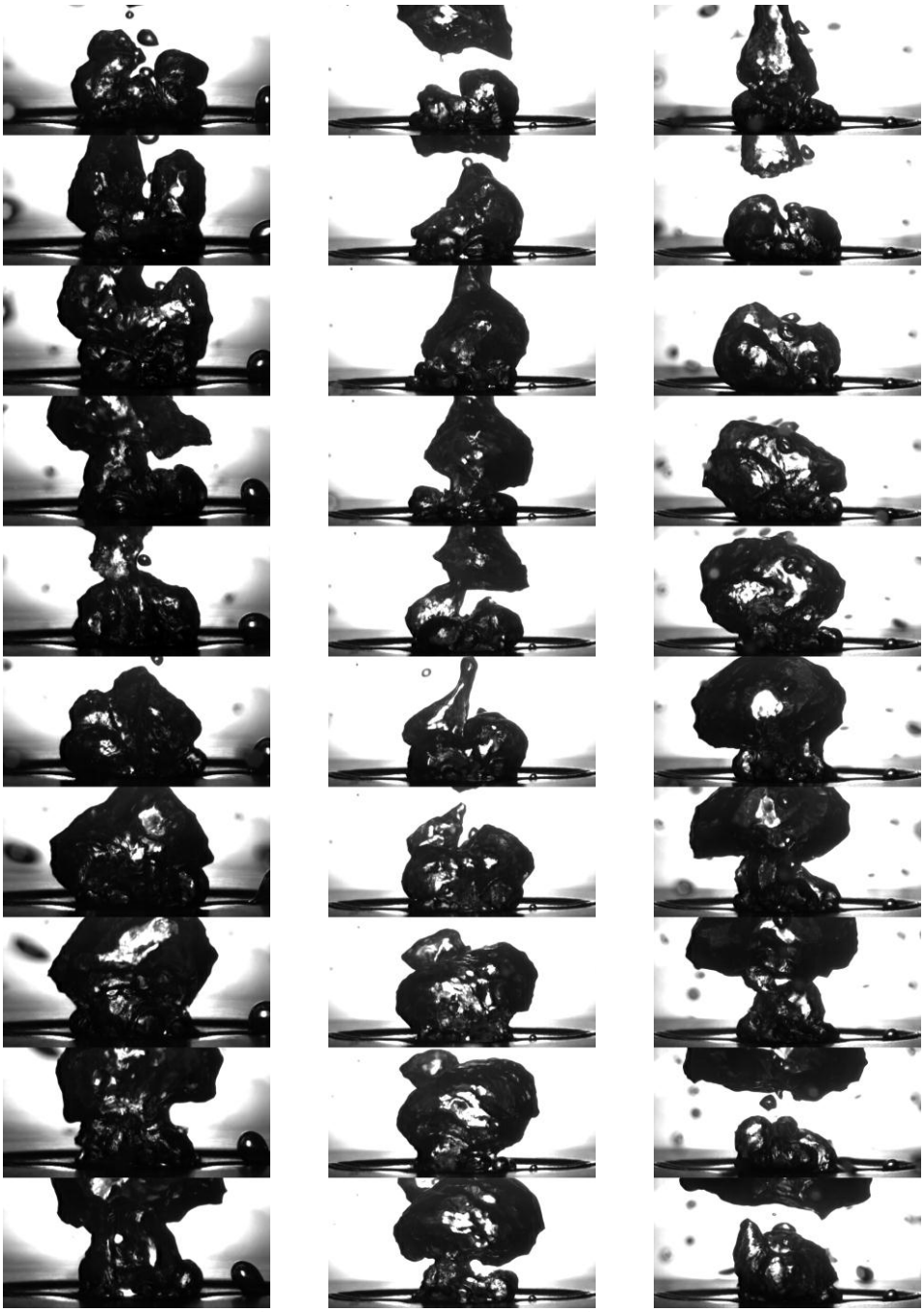

a) ΔT_{wall} = 13.9 ± 0.6 °C
q'' = 600 ± kW·m^{-2}

b) ΔT_{wall} = 14.7 ± 0.6 °C
q'' = 610 ± kW·m^{-2}

c) ΔT_{wall} = 13.4 ± 0.6 °C
q'' = 640 ± kW·m^{-2}

Figure 4-10: Example high speed video frames at high heat flux, from 23/08/2012 (a), 27/08/2012 (b), and 18/09/2012 (c). Footage shot at 2500 FPS, every 20th frame shown (Δt = 8 ms)

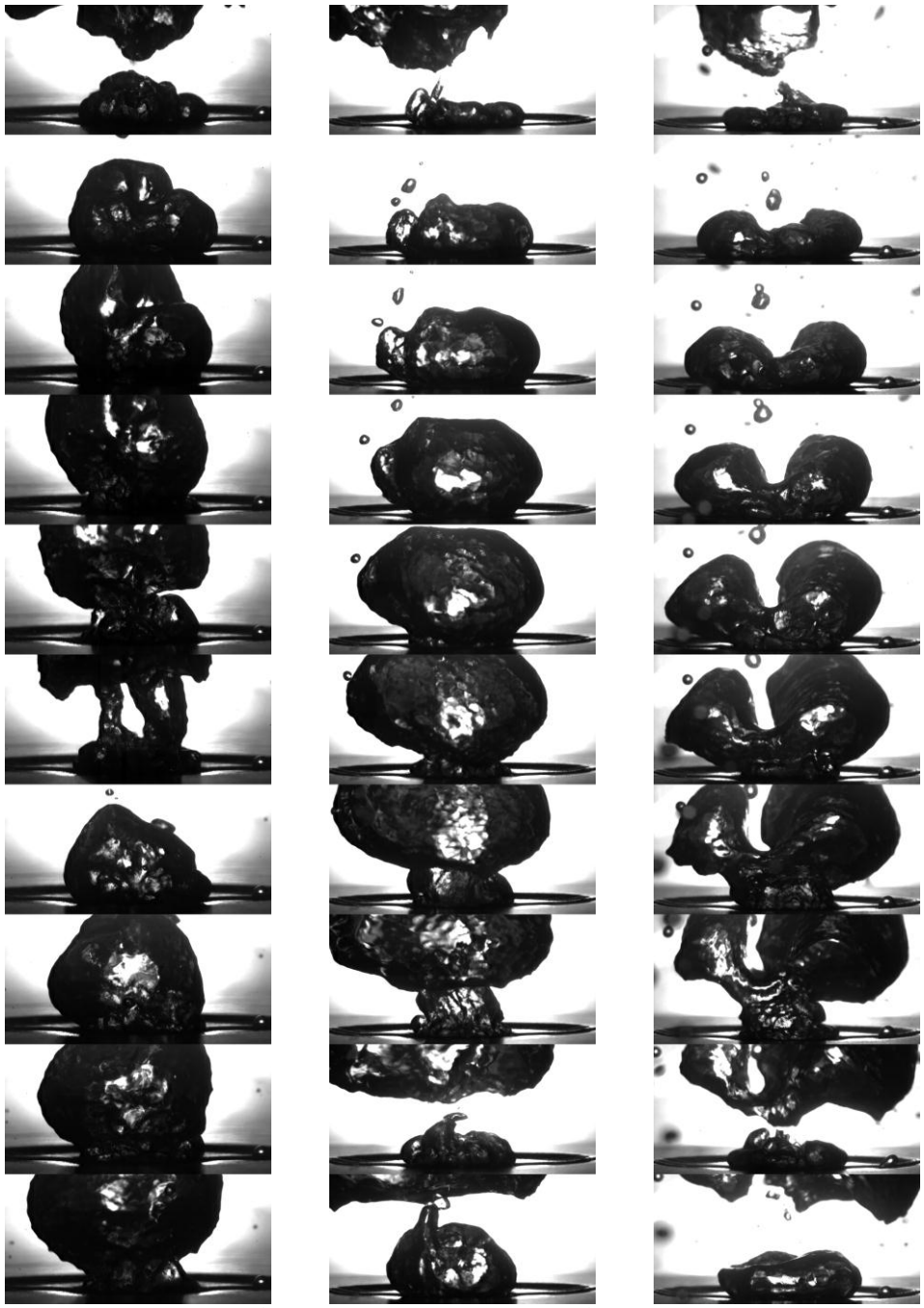

a) ΔT_{wall} = 17.5 ± 0.6 °C
q'' = 1100 ± kW·m^{-2}

b) ΔT_{wall} = 19.3 ± 0.6 °C
q'' = 1130 ± kW·m^{-2}

c) ΔT_{wall} = 17.5 ± 0.6 °C
q'' = 1100 ± kW·m^{-2}

Figure 4-11: Example high speed video frames near CHF, from 23/08/2012 (a), 27/08/2012 (b), and 18/09/2012 (c). Footage shot at 2500 FPS, every 20th frame shown (Δt = 8 ms)

4.5 Test Section Heat Loss

In order to estimate the maximum heat flux that could be delivered to the test section, heat losses from the test section were estimated. For each data point measured for the boiling curve, the thermal power conducted through the test section was estimated by multiplying the measured heat flux by the copper rod cross sectional area:

$$P_{test} = q'' \times \frac{\pi D^2}{4}$$

$$P_{test} = q'' \times \frac{\pi\left(\frac{3}{8}\times 2.54\times 10^{-2}\ m\right)^2}{4}$$

The percentage of heat generated from the cartridge heater that was conducted through the test section was taken as the ratio of the test section power to the measured heater power. These results are plotted in Figure 4-12. The percentage of heater power conducted was observed to level off above 200 W applied heater power. This sample was used to calculate a mean and standard deviation of 31.2 ± 0.6%.

The maximum heater power was specified to be 600 W. Assuming that the behaviour shown in Figure 4-12 holds at higher power, this suggests a test section power of 187 ± 4 W at a heater power of 600 W. Given the test section diameter of 9.53 mm, this suggests a maximum heat flux of (2.62 ± 0.06) MW·m^{-2}.

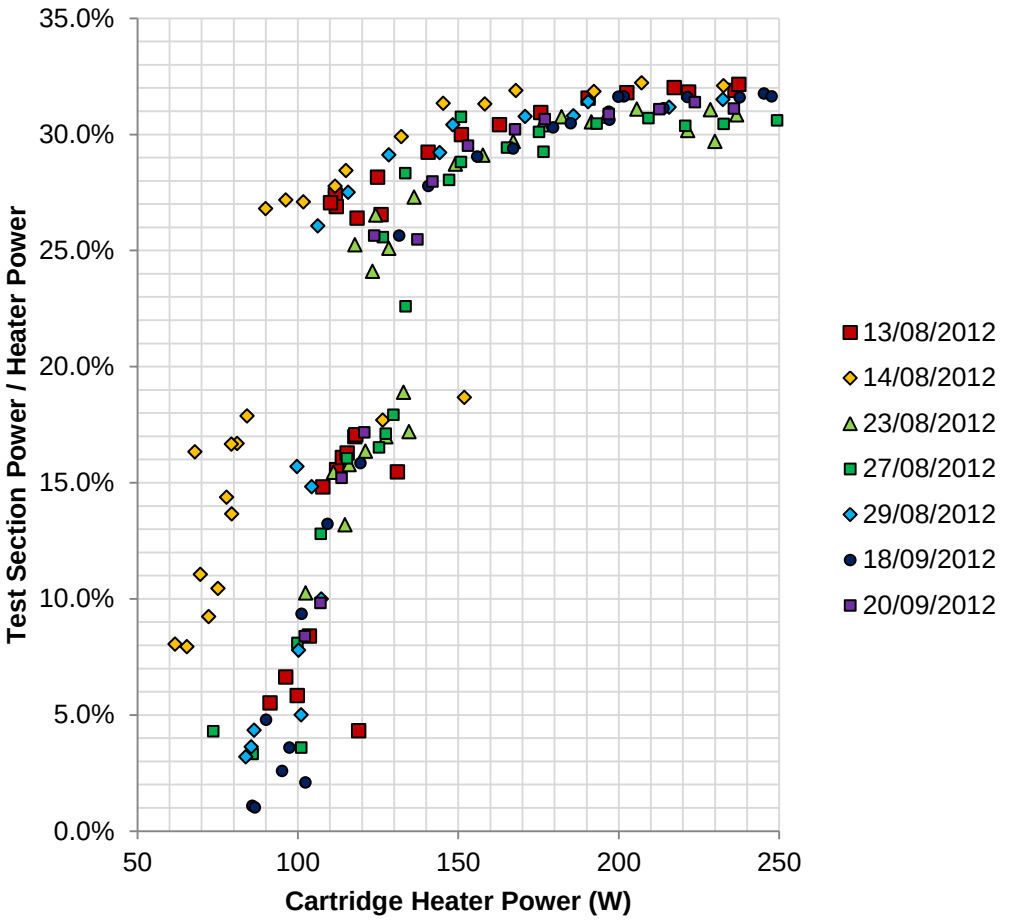

Figure 4-12: Percentage of heater power conducted through test section as a function of heater power

Chapter 5

Future Work

5.1 Improvements to Experimental Facility

In conducting the commissioning tests, several difficulties were encountered with the current iteration of the boiling vessel and test section design. These issues are outlined below along with a discussion of which aspects should be refined prior to conducting boiling experiments using nanofluids.

5.1.1 Removable Boiling Interface

A removable and replaceable boiling surface was a requirement for the boiling facility which has yet to be satisfied. The motivation behind a replaceable boiling surface was to allow easier study and comparison of the surface conditions following each test. A fresh boiling surface each time would also allow for tighter control of surface conditions prior to each test. For such a system to be successful, attachment and removal of the boiling surface must be non-destructive, cause

minimal modification to the surface, and cause a minimal temperature drop at the interface between the test section and the boiling surface.

In the original design, the boiling surface was to consist of a 0.53 mm (0.021 in) thick C110 copper plate. The copper plate was to be affixed to the test section using thermally conductive epoxy (Omega OB-200). Several difficulties were encountered with this arrangement. First, the epoxy required curing at elevated temperatures (200^{o}C for two hours). This was observed to cause discolouration and/or oxidation of the copper plates. Additionally, the epoxy was specified to have a conductivity of 1.4 $W \cdot m^{-1} \cdot K^{-1}$ (9.6 $BTU \cdot in \cdot hr^{-1} \cdot ft^{-2} \cdot {}^{o}F^{-1}$) [34]. This was noted to cause a sizable temperature drop at the interface between the test section and the boiling interface (36^{o}C at 1 $MW \cdot m^{-2}$ and a 50 micron thickness). This would not only require higher heater powers to overcome this loss but would introduce additional uncertainties to the wall temperature measurement resulting from having to model this interface. Alternative options such as brazing the surface to the test section were briefly explored but not pursued since such a process would modify the surface before examination.

Rather than relying conducting heat through the same interface holding the boiling surface in place, possible solutions to this problem would rely on direct thermal contact between the boiling interface and the test section. A removable cap to the heater assembly could be made to bolt to the existing ceramic insulator; the cap would apply clamping force which would hold a copper plate against the

test section. A thin layer of thermal grease would then be used to reduce contact resistance between the boiling surface and the test section. While the temperature drop across this interface would still need to be modelled, the temperature drop would be smaller than with the conductive epoxy.

5.1.2 Improved Sealing of Test Section

Proper sealing of the tank is essential to prevent the release of potentially hazardous nanofluids during the experiment. This is equally important if future experiments are to be conducted at elevated or reduced pressures.

In the current design, the test section is inserted from the base of the tank and is sealed against the ceramic insulator using a compressible graphite gasket. A 1.3×10^{-4} m (0.005 in) gap exists between the insulator and the test section which was filled with a high temperature silicone. The ceramic cap used to clamp the test section in place proved to be brittle and was not able to compress the graphite gasket to a high enough degree to provide a reliable seal. The base was sealed using the same high temperature silicone; this arrangement introduced additional difficulties which are outlined below.

5.1.2.1 Test section and insulator gap

The silicone did not provide a reliable seal between the radial walls of the test section and the insulator. At high heat fluxes, the temperatures along the radial walls of the test section are sufficient enough for any gap to be voided. At lower

heat fluxes in the natural convection region prior to the onset of nucleate boiling at the axial end of the test section, temperatures at the radial walls of the test section cause boiling to occur. As vapour pockets are formed, spurious releases of vapour bubbles are observed at the split of the top insulator of the heater assembly and at the perimeter of the boiling surface. Additionally, as the gap is gradually voided, unstable temperature readings are seen. This limits the usefulness of the boiling facility for conducting measurements in the natural convection region of the boiling curve. Improved sealing of the test section at the top of the heater assembly would be required before such a study could be performed.

5.1.2.2 Test Section Temperature Limit

The use of high temperature silicone to seal the test section at the base of the tank introduces a limit to which the test section can safely be heated. The silicone is specified to withstand up to 260^{o}C continuously and 316^{o}C for short time periods [24]. This seal is located at the base of the test section directly adjacent to the location of the heater. Therefore, this location is likely to exhibit temperatures higher than seen at the instrumentation located at the top of the test section.

The boiling facility was designed for a maximum heat flux of approximately 3 MW·m^{-2}. Referring to Equation 4.2, at this heat flux level the temperature drop across the instrumented section of the test section would be approximately 120^{o}C.

$$\Delta T = \frac{q_z'' \times \Delta z}{k}$$

$$\Delta T \approx \frac{(3\times10^{6}\ W\cdot m^{-2})(0.6\times0.0254\ m)}{3.9\times10^{2}\ W\cdot m^{-1}\cdot K^{-1}} \approx 120℃$$

The wall superheat at this heat flux is not known but it is likely that with elevated temperatures adjacent to the cartridge heater that the upper temperature limits of the silicone may be exceeded at high heat flux levels.

5.1.2.3 Insulator Porosity

The ceramic material chosen for the insulator was found to be porous to water. Since the base of the insulator assembly was exposed at the base of the tank, an additional aluminum cap and silicone was used to prevent a slow leak at the base of the tank during the distilled water tests. This problem would need to be addressed before performing tests with nanofluids. While a slow leak of nanofluids from the base of the tank is undesirable, an additional difficulty could arise if different nanofluids are tested. Since the ceramic material is porous and nanofluids may become entrained in this material, cleaning the heater assembly to prevent cross-contamination between nanofluid tests would be difficult.

For the current design iteration, alumino-silicate was chosen for the insulator material for its ability to withstand temperatures above 500^{o}C. Initially PTFE was selected but was replaced due to its upper working temperature limit of 260^{o}C. A potential solution could be to use a hybrid PTFE insulator with a ceramic lining at the interface to the test section. Surfaces exposed to fluid and the exterior of the tank could be made of PTFE to seal the porous insulating material.

5.1.3 Heater Control at Low Power

As covered in section 4.3.3, the coarse voltage adjustment possible with the variable autotransformer to the test section heater was a factor which hindered the gathering data points near the onset of nucleate boiling. If finer measurements are desired at low powers, the variable autotransformer could be replaced with a voltage supply capable of finer control at low voltages. For example, a DC power supply could be used for this application. This modification to procedure may only be necessary at lower voltages since the variable autotransformer offered sufficient control at high voltages.

5.2 Future Research Activities

Following any necessary improvements are made to the experimental facility, data for nanofluid pool boiling can be obtained. The future direction of the research program is outlined below.

5.2.1 Quantitative Analysis of Bubble Dynamics

In order to quantitatively measure the bubble dynamics, the next step is to develop a procedure for processing the existing captured high speed video using shadowgraphic techniques. With image processing, vapour bubbles could be tracked as they are formed, grow, and depart from the heater surface. From this, bubble departure size and frequency could be obtained. An alternative, more labour intensive method would involve manually analyzing the video footage

frame-by-frame. Given a scale reference from the boiling surface dimensions, pixel counts could be converted to physical dimensions and a time reference is given from the camera frame rate. This work can begin immediately in parallel to improvements to the facility since existing high speed video footage from the commissioning tests is readily available.

Should image processing of the existing footage prove not feasible due to the presence of overlapping vapour bubbles, further imaging techniques could be explored. One possible option is the use of particle image velocimetry (PIV). PIV techniques use a sheet-laser oriented perpendicular to the imaging plane. The laser is pulsed at a high frequency which is synchronized to a high speed camera; objects or tracer particles in the path of the laser reflect this light and are captured on video. Such a technique may increase the ease in which vapour bubbles in a single plane of interest can be examined.

The use of PIV may introduce additional concerns which need to be addressed. For such a system to be workable, optical access at the top of the tank is required which would require a rethinking of the cooling tank design. If the vapour bubbles alone are not sufficient for tracking movement via PIV, the use of tracer particles may be required. Should this be the case, control tests using distilled water with and without tracer particles would be required to measure their impact on boiling heat transfer.

5.2.2 Preparation and Characterization of Nanofluids

Prior to gathering pool boiling data with nanofluids, these nanofluids need to be prepared and characterized. For a greater level of consistency, commercially produced nanoparticle dispersions have been selected over preparing dispersions in-house using a two-step process. In preparation for the next stages of the experiment, high concentration Al_2O_3, SiO_2, and TiO_2 dispersions in water have been obtained from NanoAmor [35]. These dispersions range in concentration from 150 – 300 g/L and have no added surfactants or dispersants. These dispersions would then be diluted to the desired concentration for use in the boiling experiments (< 1 g/L).

To account for any impact that dispersed particle size has on boiling performance, it is also necessary to characterize the average particle size in the nanofluids since particles may form agglomerations during preparation. A technique such as dynamic light scattering (DLS) could be used to characterize the nanofluids before and after boiling.

5.2.3 Boiling of Nanofluids and Surface Characterization

Following the preparation and characterization of the nanofluids, nanofluid boiling experiments can begin. First, to test the effect of nanofluid concentration on boiling performance, a single nanofluid type will be tested at varying

concentration levels. These tests can also be repeated using various nanoparticle types.

Characterization of the boiling surface will also be conducted. Metrics such as fluid contact angle and surface roughness should be gathered both before and after experiments in water and nanofluids to examine how the surface conditions change during boiling. Additional analysis using scanning electron microscopy (SEM) will also be conducted. If significant surface modification is observed following boiling in nanofluids, tests could be conducted using nanofluid modified surfaces in distilled water.

Chapter 6

Conclusion

A pool boiling experiment has been designed and constructed at McMaster University to allow for the study the boiling of water-based nanofluids. The facility has been commissioned by conducting tests with saturated distilled at atmospheric pressure in the nucleate boiling region. Tests were conducted at heat flux levels up to 1200 $kW \cdot m^{-2}$ and at wall superheat levels up to 19.5^{o}C. Wall superheat and heat flux uncertainties were estimated to be ±0.6^{o}C and ±20 $kW \cdot m^{-2}$, respectively. For the installed test section, heat flux is limited to 2.62 ± 0.06 $MW \cdot m^{-2}$.

Heat flux versus wall superheat data was compared to the Rohsenow correlation and found qualitatively agree using surface factor C_{sf} = 0.011. Results were found to have a high degree of repeatability at heat flux levels higher than 600 $kW \cdot m^{-2}$. A high speed video system for the capture and analysis of bubble dynamics was also tested and used for qualitative comparisons between experimental runs. This

system was tested at 2500 FPS and at an imaging resolution of 39 pixels per mm, but is capable of 10 000 FPS measurements at the same spatial resolution.

With minor modifications to the new facility, the study of saturated water-based nanofluid pool boiling can begin. Future work will focus on implementing replaceable boiling surfaces to increase the degree of control over surface preparation and to aid in surface characterization before and after boiling. Additional work may involve sealing the porous ceramic insulator installed around the test section to avoid cross contamination of boiling fluids between tests. Quantitative analysis of the existing high speed footage can additionally begin with the development of an image processing toolkit for bubble tracking while future measurements may involve the use of particle image velocimetry.

Bibliography

[1] **Choi, S. U. S. and Eastman, J. A.** Enhancing thermal conductivity of fluids with nanoparticles. *ASME International Mechanical Engineering Congress & Exposition.* 1995, Vol. 231, pp. 99-105.

[2] **Maxwell, J. C.** *Treatise on Electricity and Magnetism.* Oxford : Clarendon Press, 1873.

[3] **Das, S. K., Choi, S. U. S. and Patel, H. E.** Heat Transfer in Nanofluids - A Review. *Heat Transfer Engineering.* 2006, Vol. 27, 10, pp. 3-19.

[4] **Wen., D., et al.** Review of nanofluids for heat transfer applications. *Particuology.* 2009, Vol. 7, pp. 141-150.

[5] **Collier, John G. and Thome, John R.** *Convective Boiling and Condensation.* 3rd edition. Oxford : Oxford University Press, 1996.

[6] **Morris, S. and Chen, S. H.** Rayleigh-Bénard and Bénard-Marangoni convection. *The Experimental Nonlinear Physics Group.* [Online] [Cited: February 8, 2013.] http://www.physics.utoronto.ca/~nonlin/thermal.html.

[7] **Todreas, N. E. and Kazimi, M. S.** *Nuclear Systems I - Thermal Hydraulic Fundamentals.* New York : Taylor & Francis, 1990.

[8] **Petrovic, S., Robinson, T. and Judd, R. L.** Marangoni heat transfer in subcooled nucleate pool boiling. *International Journal of Heat and Mass Transfer.* 2004, Vol. 47, 23, pp. 5115-5128.

[9] **Taylor, R. A. and Phelan, P. E.** Pool boiling of nanofluids: Comprehensive review of existing data and limited new data. *International Journal of Heat and Mass Transfer.* 2009, Vol. 52, 23, pp. 5339-5347.

[10] **Kim, S. J., et al.** Surface wettability change during pool boiling of nanofluids and its effect on critical heat flux. *International Journal of Heat and Mass Transfer.* 2007, Vol. 50, 19, pp. 4105-4116.

[11] **Wu, D., et al.** Critical issues in nanofluids preparation, characterization, and thermal conductivity. *Current Nanoscience.* 2009, Vol. 5, 1, pp. 103-112.

[12] **Moffat, J. R., et al.** Recent progress on nanofluids and their potential applications. [ed.] V. M. Starov. *Nanocolloids.* Boca Raton : CRC Press, 2010.

[13] **Lo, C. H., et al.** Fabrication of copper oxide nanofluid using submerged arc nanoparticle synthesis system (SANSS). *Journal of Nanoparticle Research.* 2005, Vol. 7, 2, pp. 313-320.

[14] **Zhu, H. T., Lin, Y. S. and Yin, Y. S.** A novel one-step chemical method for preparation of copper nanofluids. *Journal of Colloid and Interface Science.* 2004, Vol. 277, 1, pp. 100-103.

[15] **You, S. M., Kim, J. H. and Kim, K. H.** Effect of nanoparticles on critical heat flux of water in pool boiling heat transfer. *Applied Physics Letters.* 2003, Vol. 83, 16, p. 3374.

[16] **Kwark, S. M., et al.** Pool boiling characteristics of low concentration nanofluids. *International Journal of Heat and Mass Transfer.* 2010, Vol. 53, 5, pp. 972-981.

[17] **Kim, H. D. and Kim, M. H.** Effect of nanoparticle deposition on capillary wicking that influences the critical heat flux in nanofluids. *Applied Physics Letters.* 2007, Vol. 91, 1, p. 14104.

[18] **Kim, H. D., Kim, J. and Kim, M. H.** Experimental studies on CHF characteristics of nano-fluids at pool boiling. *International Journal of Multiphase Flow.* 2007, Vol. 33, 7, pp. 691-706.

[19] **Kwark, S. M., et al.** Nanocoating characterization in pool boiling heat transfer of pure water. *International Journal of Heat and Mass Transfer.* 2010, Vol. 53, 21.

[20] **Coursey, J. S. and Kim, J.** Nanofluid boiling: the effect of surface wettability. *International Journal of Heat and Fluid Flow.* 2008, Vol. 29, 6, pp. 1577-1585.

[21] **Kathiravan, R., et al.** Preparation and pool boiling characteristics of copper nanofluids over a flat plate heater. *International Journal of Heat and Mass Transfer.* 2010, Vol. 53, 9, pp. 1673-1681.

[22] **Kathiravan, R., et al.** Pool boiling characteristics of multiwalled carbon nanotube (CNT) based nanofluids over a flat plate heater. *International Journal of Heat and Mass Transfer.* 2011, Vol. 54, 5, pp. 1289-1296.

[23] **Aremco Products Inc.** Machinable & Dense Ceramics - Technical Bulletin A1. [Online] [Cited: December 20, 2012.] http://www.aremco.com/wp-content/uploads/2010/11/A01_12.pdf.

[24] **Imperial Manufacturing Group.** Hi-temperature Silicone Sealant (red). [Online] [Cited: July 16, 2012.] http://www.imperialgroup.ca/fireplace_maintenanceproducts.cfm?c=385.

[25] **National Instruments.** NI 9213 Data Sheet. [Online] [Cited: December 20, 2012.] http://sine.ni.com/ds/app/doc/p/id/ds-69/lang/en.

[26] —. NI 9205 Data Sheet. [Online] [Cited: December 20, 2012.] http://sine.ni.com/ds/app/doc/p/id/ds-190/lang/en.

[27] **Hammond Manufacturing.** Potential Transformers Low Voltage. [Online] [Cited: July 11, 2011.] http://www.hammondmfg.com/PTs.htm.

[28] **Fluke Corporation.** Fluke 80 Series V Digital Multi Meters: Specifications. [Online] [Cited: December 21, 2012.] http://www.fluke.com/fluke/usen/Digital-Multimeters/Fluke-80-Series-V.htm?PID=56135.

[29] **Çengel, Y. A., Turner, R. H. and Cimbala, J. M.** *Fundamentals of Thermal-Fluid Sciences.* Boston : McGraw-Hill, 2008.

[30] **Bevington, P. R. and Robinson, D. K.** *Data Reduction and Error Analysis.* 3rd edition. New York : McGraw-Hill, 2003.

[31] **National Institute of Standards and Technology.** NSRDS-NBS 8: Thermal Conductivity of Selected Materials. [Online] November 25, 1966. [Cited: July 16, 2012.] http://www.nist.gov/data/nsrds/NSRDS-NBS-8.pdf.

[32] **Excel Engineering.** X Steam - Properties for water and steam. [Online] [Cited: January 27, 2012.] http://xsteam.sourceforge.net/.

[33] **Pioro, I. L.** Experimental evaluation of constants for the Rohsenow pool boiling correlation. *International Journal of Heat and Mass Transfer.* 1999, Vol. 42, 11, pp. 2003-2013.

[34] **Omega Engineering.** OB-200 Epoxy Adhesive. [Online] [Cited: July 27, 2012.] http://www.omega.com/manuals/manualpdf/M0063.pdf.

[35] **Nanostructured & Amorphous Materials, Inc.** NanoAmor - About Us. [Online] [Cited: February 2013, 5.] http://www.nanoamor.com/about_us.

[36] **Omega Engineering.** Precision RTD Thermometer. [Online] [Cited: January 8, 2013.] http://www.omega.com/Temperature/pdf/DP250.pdf.

[37] —. Transition Junction Style Probes with High Temperature Molded Construction. [Online] [Cited: December 20, 2012.] http://www.omega.com/Temperature/pdf/JMTSS.pdf.

[38] —. Thermocouple Accuracy and Color Codes. [Online] [Cited: December 20, 2012.] http://www.omega.com/toc_asp/frameset.html?book=Temperature&file=tc_colorcodes.

Appendix A

Thermocouple Calibration

To reduce the measurement error resulting from the temperature measurements, the thermocouples used in the experiment were calibrated against a high-precision resistive temperature detector (RTD) probe (Omega DP251 precision RTD thermometer with PRP-3 probe). This system is specified to have 0.025^{o}C accuracy over a range of -50^{o}C to 250^{o}C [36]. The sheathed thermocouple probes were placed in an insulated and heated oil bath with the temperature monitored by the RTD. The heater power was adjusted and the RTD and thermocouple temperature readings were allowed to stabilize. The oil bath was assumed to be at a uniform temperature. To reduce systematic errors, the thermocouple hookup wire and data acquisition device channels used during calibration were identical to those used during the experiment.

A least squares fit to a straight line was performed for each data set (thermocouple reading versus RTD reading). The resulting relationship in the form $y = mx + b$ was used to relate thermocouple measurements (y) to calibrated temperatures (x).

To provide an estimate of the uncertainty in the calibrated temperature σ_T, the sample variance is used [30]:

$$\sigma_T^2 \cong s^2 = \frac{1}{N-m}\sum(y_i - \bar{y}) \tag{A.1}$$

Here, *N* is the number of data points for the calibration curve, *m* is the number of fit parameters, y_i are the thermocouple measurements and $\bar{y}$ is the result from the best fit equation:

$$\sigma_T \cong s = \sqrt{\frac{1}{N-2}\sum(y_i - a - bx_i)} \tag{A.2}$$

Finally, it was assumed that the resulting calibrated measurements would have an uncertainty of at least one order of magnitude worse than the reference instrument. Therefore, the calibrated temperature uncertainty was taken to be the larger of 0.25°C and the result from Equation A.2. In order to better estimate the uncertainties, several calibrations would have been conducted (before and after experimental runs) and the resulting sample variance used as this would capture any instrumentation drifts in calibration. However, the permanent installation of the probes in the facility made this impractical.

A.1 T-type Thermocouples (Fluid)

All temperature probes are of Omega TMTSS-125G type (0.125 in diameter stainless steel T304 grounded tip).

Table A-1: T-type thermocouple calibration data

RTD (^{o}C)	TF1 (^{o}C)	TF2 (^{o}C)	TF3 (^{o}C)	TF4 (^{o}C)
21.09	20.5810	20.5643	20.5530	20.5468
24.89	24.3942	24.3818	24.3703	24.3695
30.07	29.5937	29.6001	29.5914	29.5968
35.30	34.8541	34.8678	34.8578	34.8685
40.08	39.7046	39.7119	39.7150	39.7257
45.10	44.7428	44.7456	44.7502	44.7649
49.90	49.5306	49.5218	49.5225	49.5265
54.94	54.6096	54.6081	54.5966	54.6029
60.05	59.7417	59.7340	59.7272	59.7386
64.80	64.5237	64.5246	64.5186	64.5339
69.96	69.7141	69.7106	69.7117	69.7249
75.10	74.8856	74.9004	74.8876	74.9013
79.90	79.7038	79.7012	79.6966	79.7145
85.33	85.1672	85.1522	85.1449	85.1531
89.76	89.6119	89.5976	89.5910	89.5958
95.03	94.8954	94.8888	94.8821	94.8968
100.07	99.9683	99.9558	99.9546	99.9744
104.00	103.9133	103.9084	103.8985	103.9185
110.40	110.3271	110.3215	110.3167	110.3332
115.40	115.3516	115.3448	115.3392	115.3590
118.60	118.5785	118.5644	118.5615	118.5835
123.35	123.3348	123.3275	123.3280	123.3480
129.30	129.3257	129.3276	129.3119	129.3374
134.60	134.6449	134.6481	134.6404	134.6697
140.25	140.2957	140.3004	140.2932	140.3214
145.50	145.5561	145.5624	145.5531	145.5836
150.15	150.2413	150.2478	150.2426	150.2737

Table A-2: T-type thermocouple calibration results

ID	TF1	TF2	TF3	TF4
a	-0.58699	-0.59084	-0.59635	-0.59934
b	1.0047	1.0047	1.0047	1.0049
s	0.0190	0.0194	0.0212	0.0232

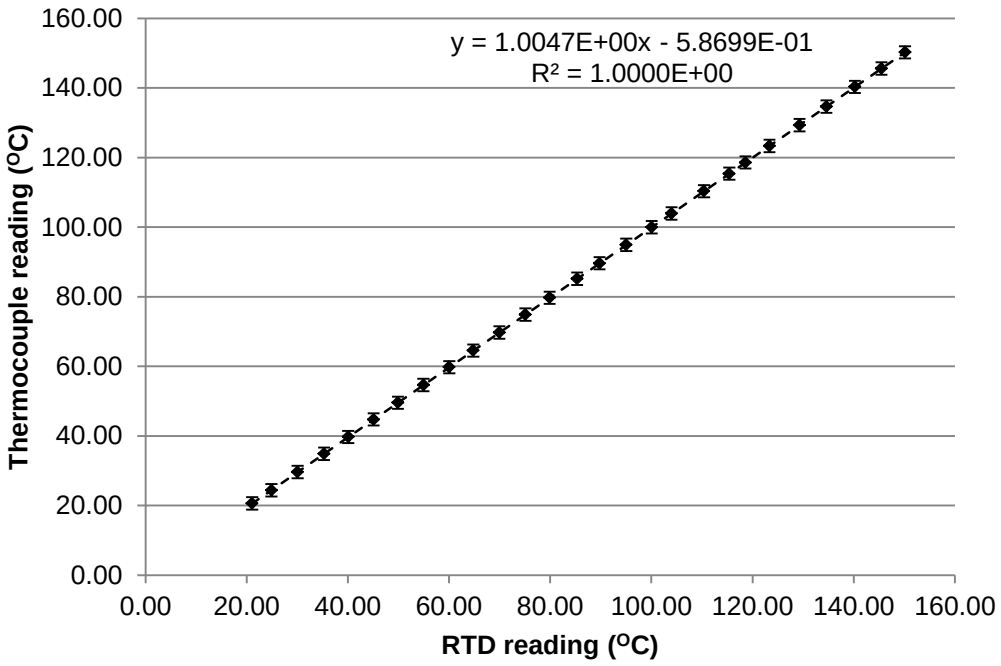

Figure A-1: Thermocouple TF1 calibration results

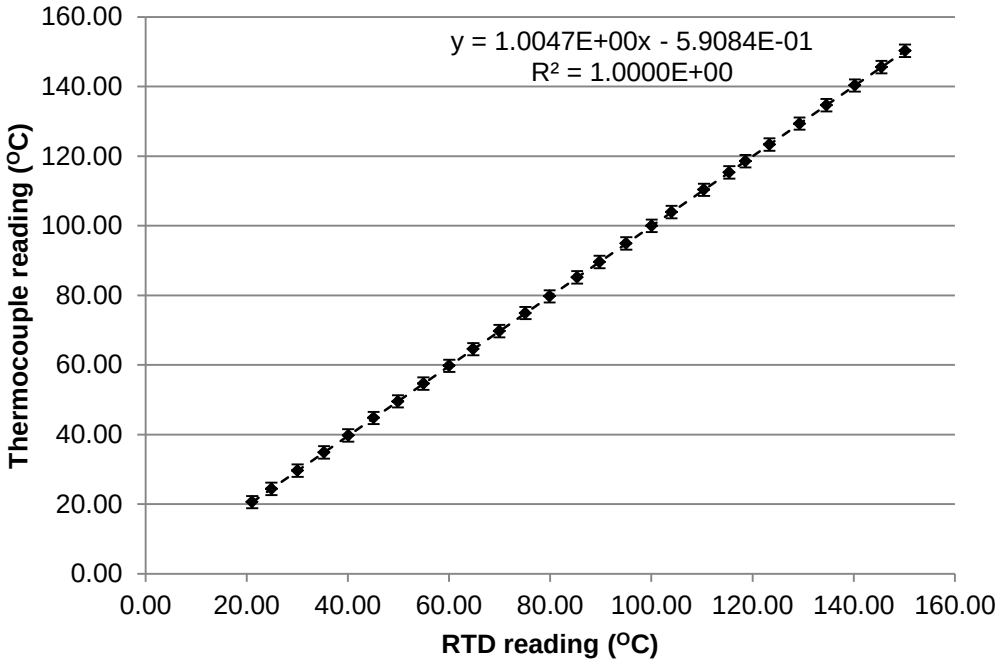

Figure A-2: Thermocouple TF2 calibration results

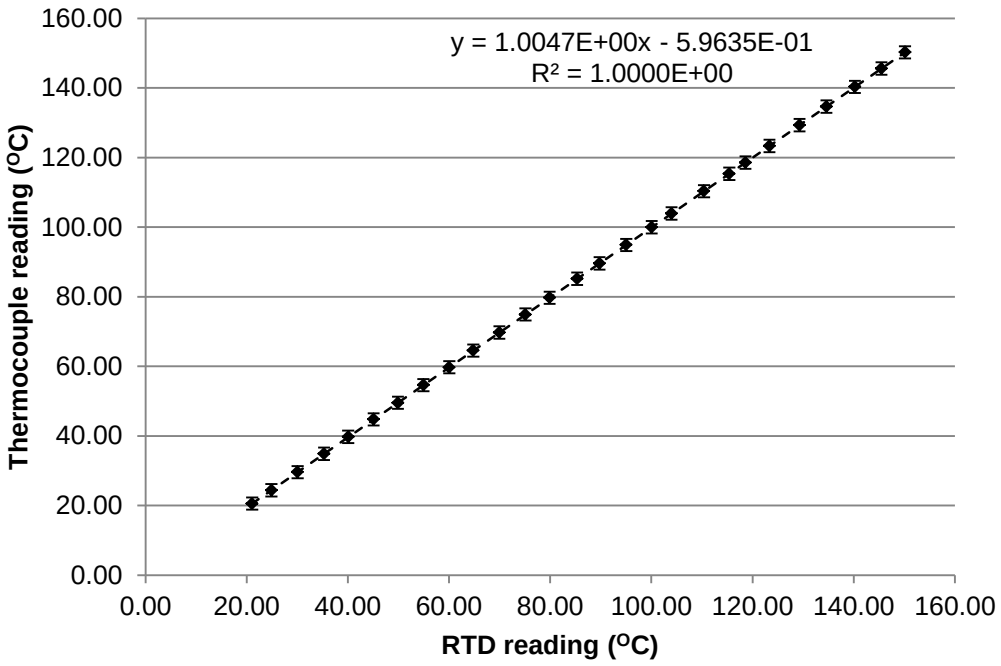

Figure A-3: Thermocouple TF3 calibration results

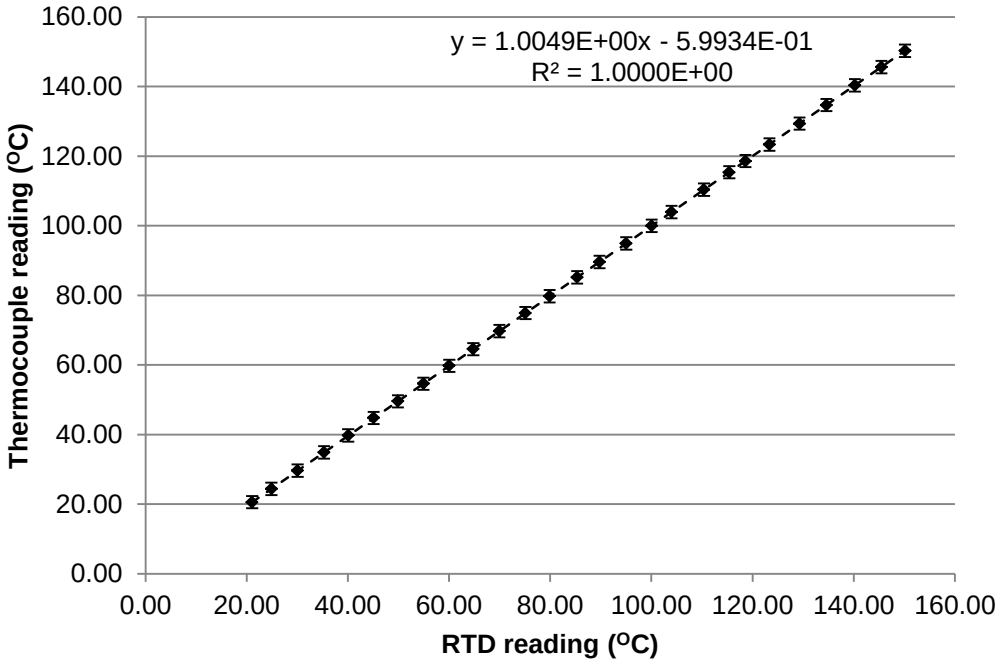

Figure A-4: Thermocouple TF4 calibration results

A.2 K-type Thermocouples (Test Section)

All temperature probes are of Omega KMTSS-040G type (0.040 in diameter stainless steel T304 ungrounded tip).

Table A-3: K-type thermocouple calibration data

RTD (^{o}C)	A1 (^{o}C)	A2 (^{o}C)	A3 (^{o}C)	A4 (^{o}C)	B5 (^{o}C)
21.81	21.4830	21.4306	21.3913	21.3718	21.3320
30.07	29.5801	29.5168	29.4943	29.4657	29.4092
40.06	39.4218	39.3552	39.3295	39.3072	39.2537
50.12	49.3666	49.2811	49.2558	49.2420	49.1765
60.22	59.3516	59.2556	59.2372	59.2270	59.1599
70.28	69.3114	69.2078	69.1753	69.1955	69.1198
80.39	79.3781	79.2468	79.2162	79.2421	79.1714
93.57	92.5657	92.4029	92.3659	92.4227	92.3578
101.10	100.1347	99.9673	99.9169	99.9959	99.9274
111.92	111.0630	110.8734	110.8339	110.9189	110.8366
120.50	119.7543	119.5612	119.5125	119.6057	119.5148
123.10	122.3864	122.1924	122.1502	122.2414	122.1405
127.50	126.8767	126.6615	126.6185	126.7118	126.6100
131.80	131.2790	131.0538	131.0017	131.1111	130.9909
141.00	140.6266	140.3932	140.3471	140.4582	140.3403
150.70	150.4302	150.1747	150.1415	150.2618	150.1405
159.30	159.0748	158.8181	158.7775	158.9035	158.7652
169.50	169.2974	169.0315	168.9963	169.1239	168.9924
181.20	180.9487	180.6799	180.6455	180.7998	180.6676
190.00	189.7470	189.4858	189.4210	189.5819	189.4469
199.10	198.8400	198.5559	198.4880	198.6419	198.4704
200.50	200.2255	199.9451	199.8832	200.0388	199.8786
210.85	210.5422	210.2522	210.1838	210.3435	210.1829
219.85	219.4745	219.2021	219.1395	219.3116	219.1732
228.85	228.4229	228.1566	228.0995	228.2650	228.1155

Table A-4: K-type thermocouple calibration results

ID	A1	A2	A3	A4	B5
a	-0.89749	-0.93452	-0.95419	-1.0036	-1.0321
b	1.0027	1.0015	1.0013	1.0024	1.0018
s	0.231	0.229	0.230	0.229	0.223

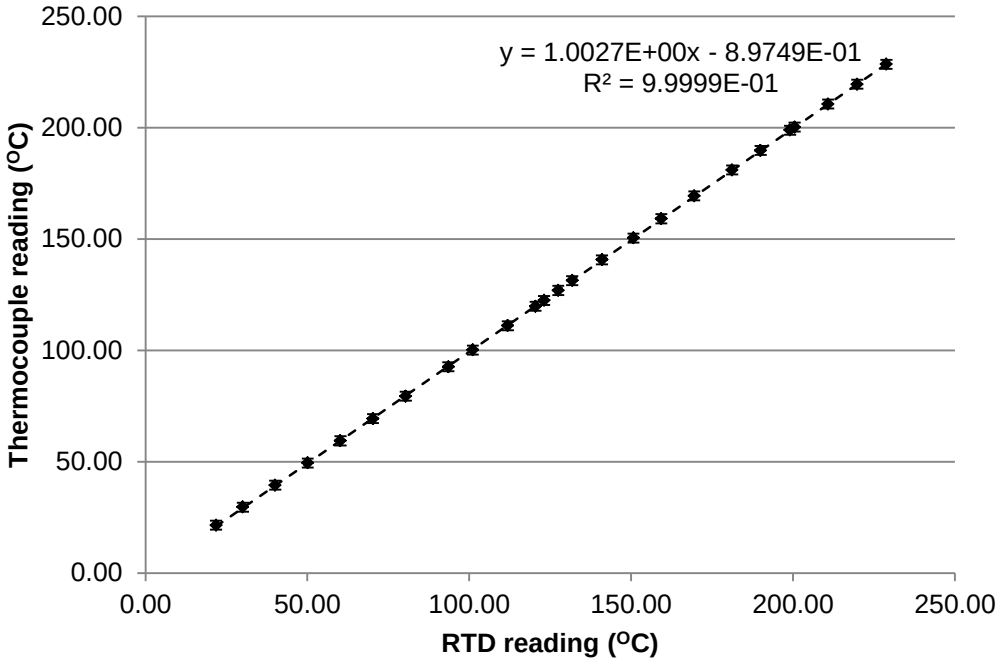

Figure A-5: Thermocouple A1 calibration results

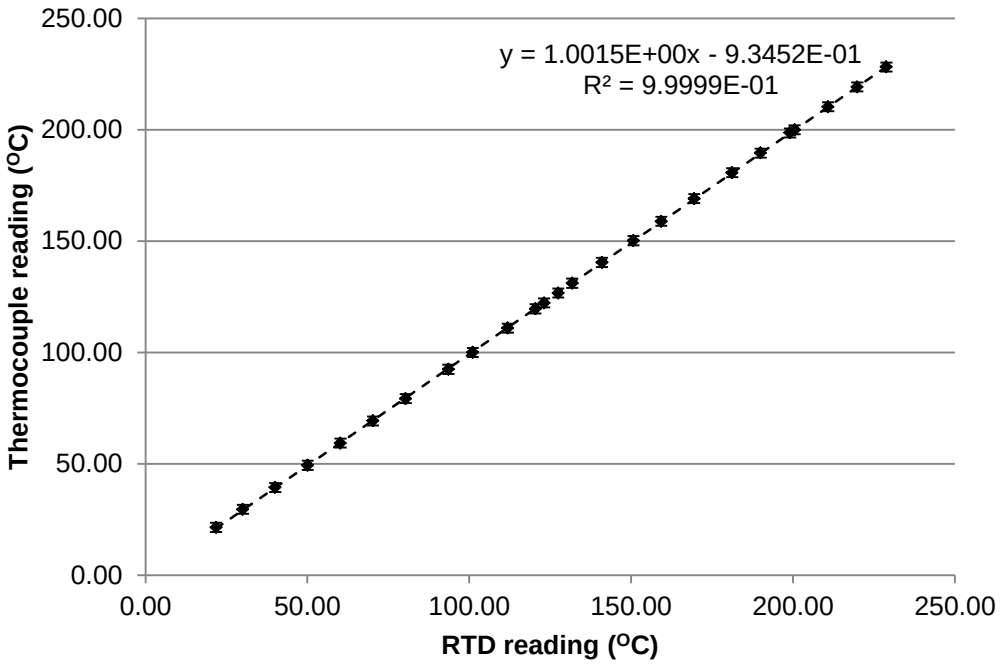

Figure A-6: Thermocouple A2 calibration results

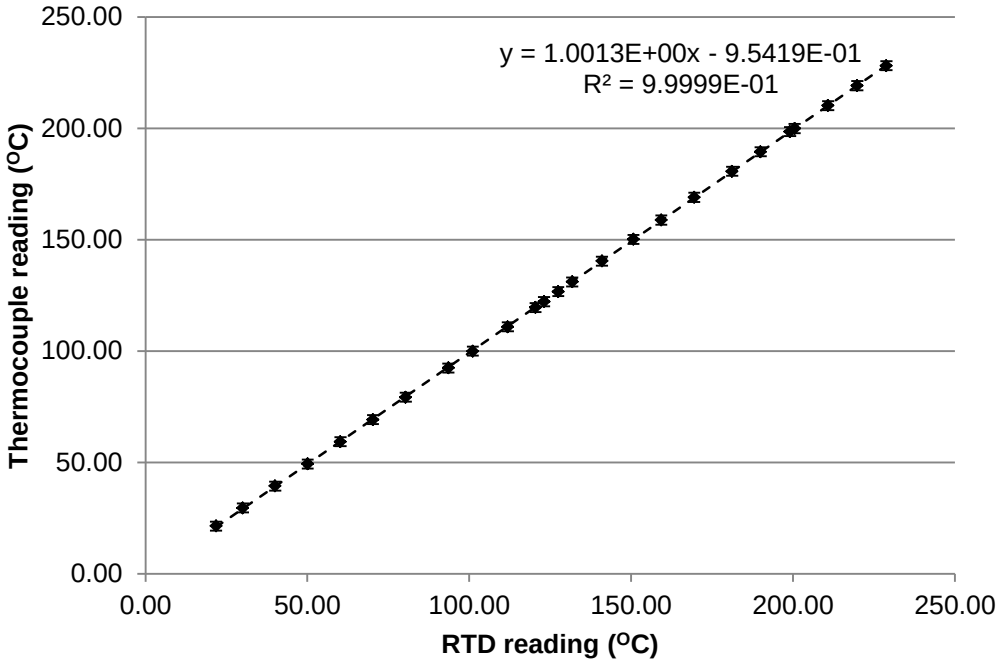

Figure A-7: Thermocouple A3 calibration results

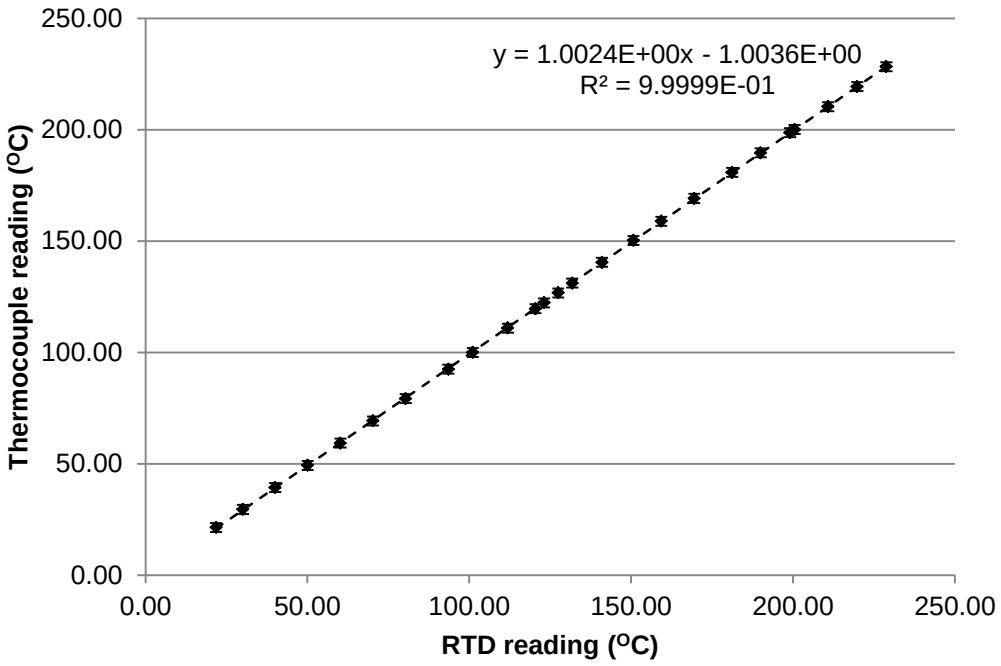

Figure A-8: Thermocouple A4 calibration results

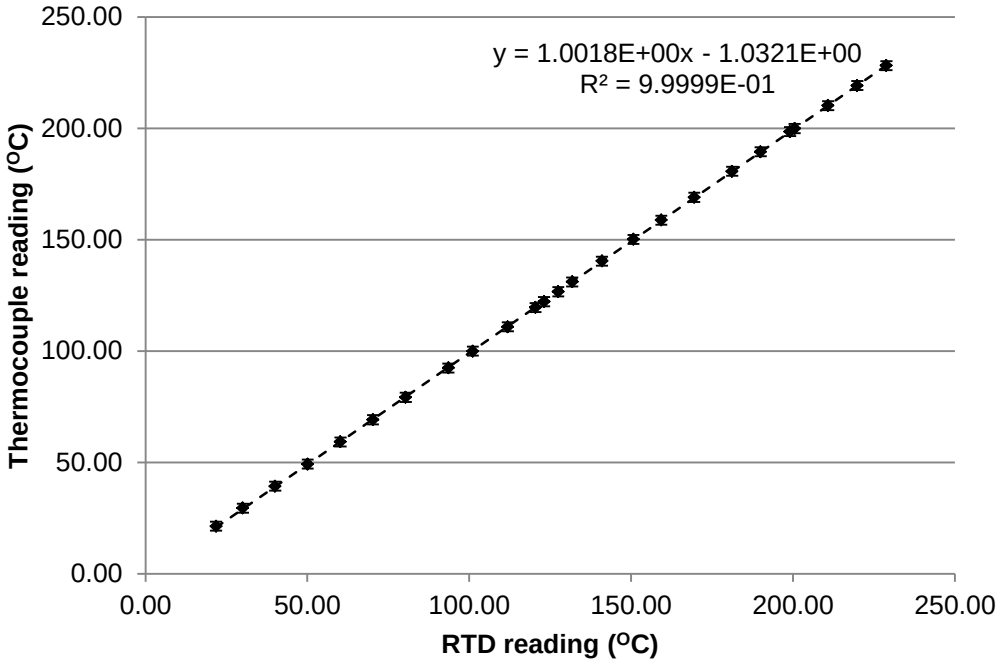

Figure A-9: Thermocouple B5 calibration results

Appendix B

Heater Power Calibration

The applied voltage and current to the test section heater (Omega CSH-206600) were logged using a National Instruments NI-9205 voltage module. A Hammond PT120CF instrumentation transformer was used to step the voltage measurement into the ± 10 V range of the NI-9205 module. Additionally a 0.1 Ω resistor (1% tolerance, 5 W) was used as a shunt to measure the applied current. The voltage and current measurements were calibrated against a Fluke 87 V digital multi-meter. Heater power was taken to be the product of the measured voltage and current.

B.1 Heater Voltage

A constant AC voltage was applied to the heater and measured using a Fluke 87V multi-meter. Additionally, the voltage output of the transformer was measured at the data acquisition system (DAQ). This procedure was repeated for several data points. This configuration is shown in Figure B-1.

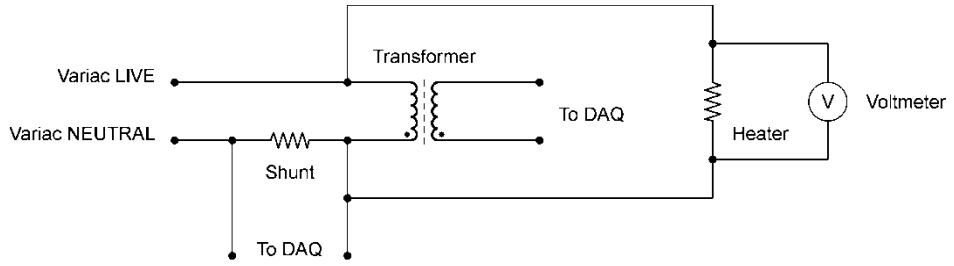

Figure B-1: Heater voltage measurement calibration procedure

The Fluke 87V meter was set to auto-range and measure RMS AC voltage. The DAQ was set at a sampling rate of 1 kHz and RMS amplitude measured using the LabView "Amplitude and Level Measurements" module. An exponential smoothing filter with τ = 0.005 was applied. The calibration results are tabulated in Table B-1 and are plotted in Figure B-2.

Table B-1: Voltage calibration measurements

Transformer (DAQ V_{RMS})	Voltmeter (V_{RMS})
0.0004	0.00
0.4323	10.42
0.8401	20.23
1.2470	30.02
1.6805	40.47
2.1135	50.90
2.528	60.85
2.930	70.7
3.367	81.1
3.775	91.0
4.262	102.6
4.595	110.7
5.025	121.0
5.402	130.1

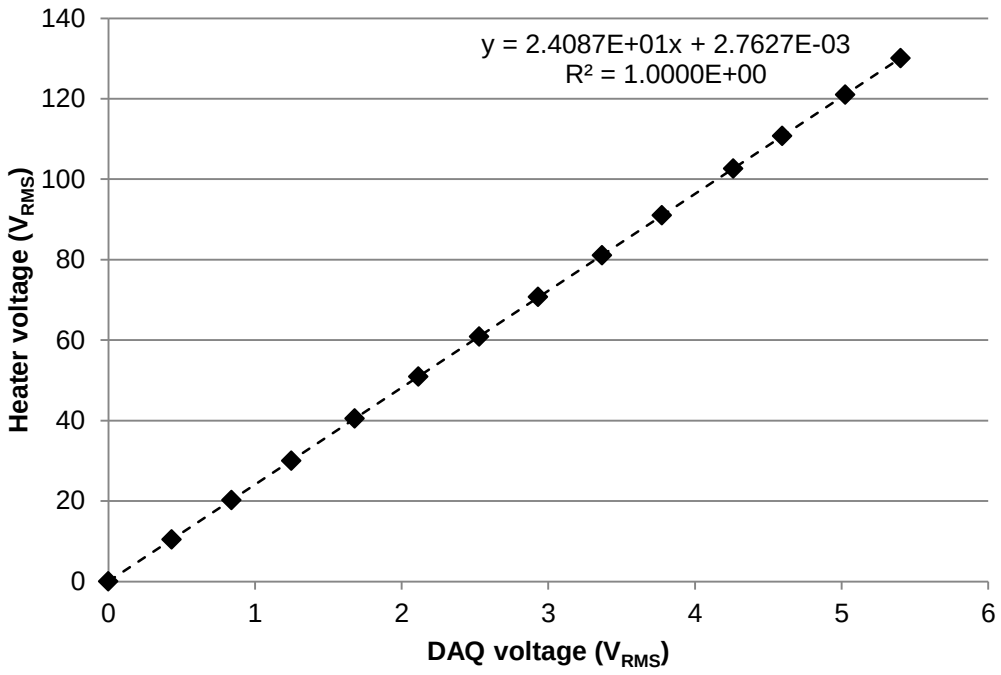

Figure B-2: Heater voltage versus acquired voltage

A simple linear regression was performed with the data; the fit parameters shown in Figure B-2 were used in the LabView routine to calculate the heater voltage from the DAQ measurement of the transformer voltage.

B.2 Heater Current

A constant AC voltage was applied to the heater and the resulting current measured using a Fluke 87V multi-meter. Additionally, the voltage output of the shunt was measured at the data acquisition system (DAQ). This procedure was repeated for several data points.

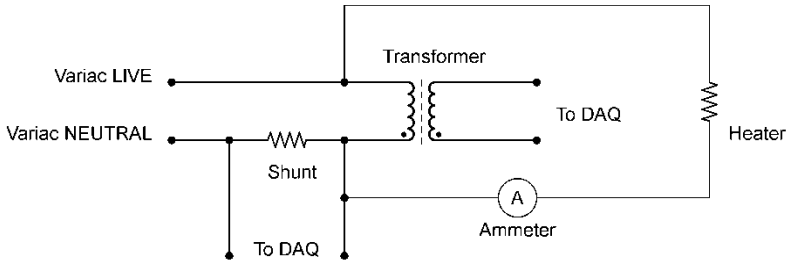

Figure B-3: Heater current measurement calibration procedure

The Fluke 87V meter was set to measure RMS AC amperage; the 400 mA range was used for currents below 400 mA, otherwise the 10 A range was selected. The DAQ was set at a sampling rate of 1 kHz and RMS amplitude measured using the LabView "Amplitude and Level Measurements" module. An exponential smoothing filter with τ = 0.005 was applied. The calibration results are tabulated in Table B-2 and are plotted in Figure B-4.

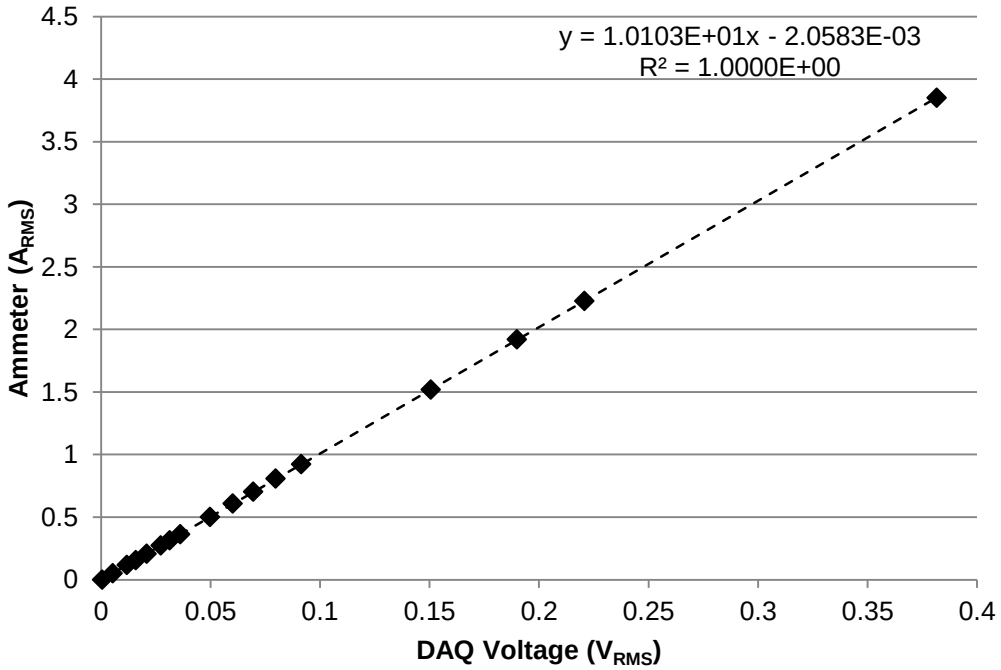

Figure B-4: Heater current versus acquired shunt voltage

Table B-2: Current calibration results

Shunt (DAQ mV_{RMS})	Ammeter (A_{RMS})
0.60	0.00000
5.44	0.05225
11.84	0.1175
15.90	0.1574
20.88	0.2079
27.30	0.2729
31.44	0.3144
36.20	0.362
49.80	0.502
60.20	0.608
69.60	0.703
79.80	0.808
91.50	0.924
220.70	2.227
150.60	1.52
189.90	1.92
381.60	3.85

A simple linear regression was performed with the data; the fit parameters shown in Figure B-4 were used in the LabView routine to calculate the heater current from the DAQ measurement of the shunt voltage.

Appendix C

Thermocouple Linearity Data

In order to confirm good thermal contact of the thermocouples with the test section, the linearity of the temperature measurements with respect to position were verified by plotting measured temperature versus vertical position. The temperature data consistently showed good linearity consistently throughout the experiment at all probe locations. Sample temperature profiles from each test day are presented on the following pages.

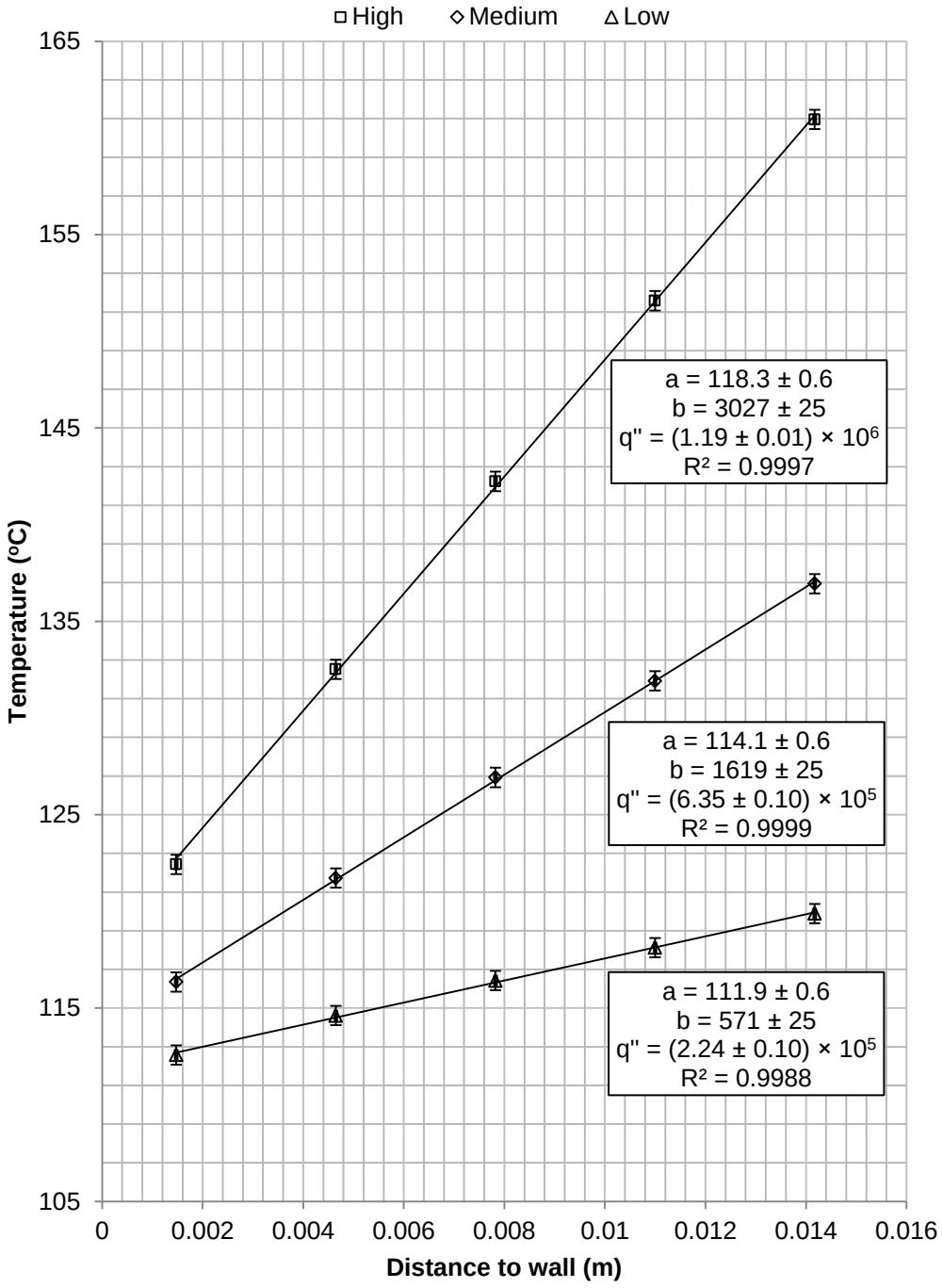

Figure C-1: Sample temperature gradient data from 13/08/2012. For each linear fit: *a* is the predicted wall temperature (^{o}C), *b* is the fitted slope (^{o}C·m^{-1}), and *q″* is the corresponding heat flux (W·m^{-2})

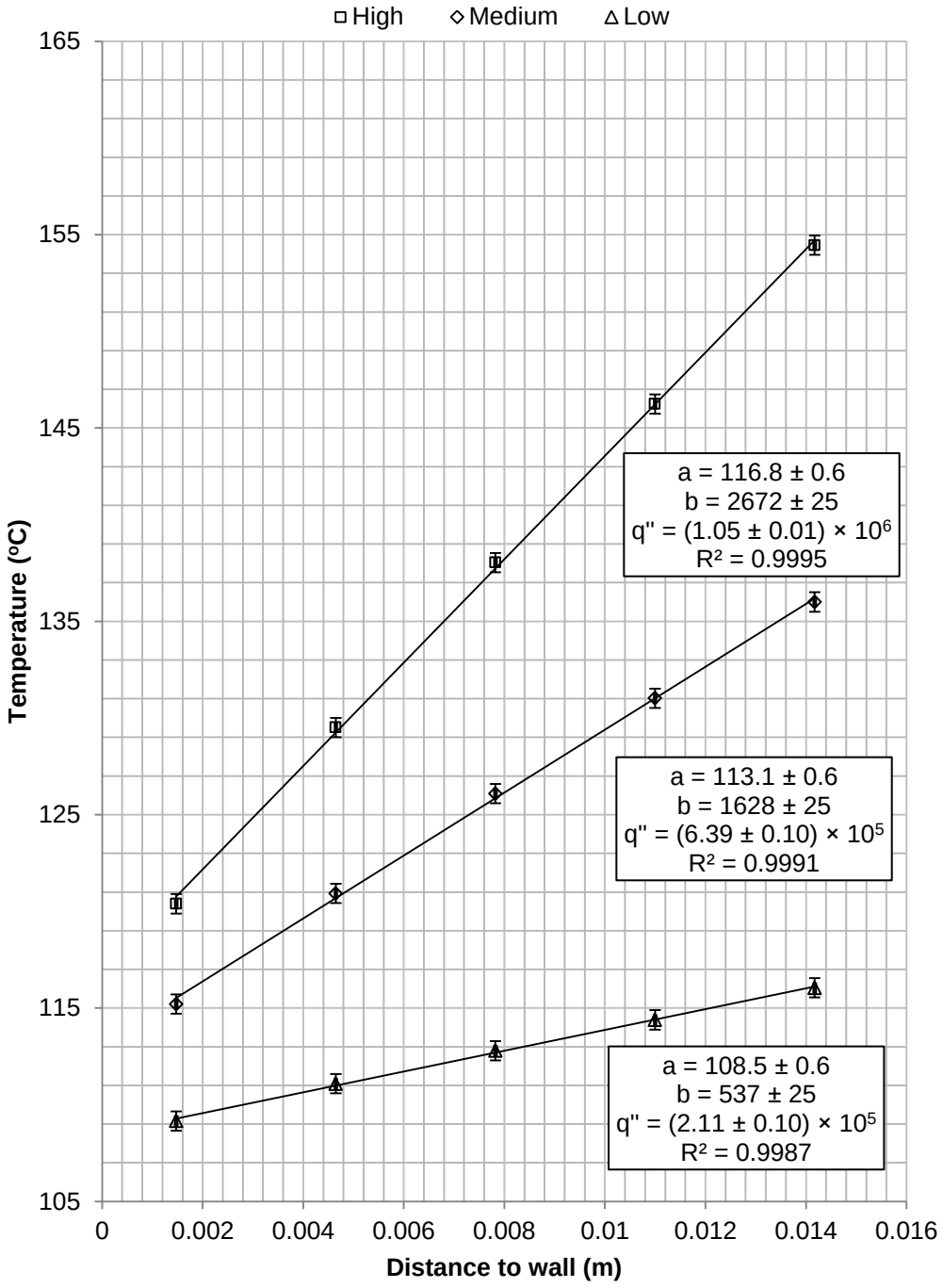

Figure C-2: Sample temperature gradient data from 14/08/2012. For each linear fit: *a* is the predicted wall temperature (°C), *b* is the fitted slope (°C·m^{-1}), and *q″* is the corresponding heat flux (W·m^{-2})

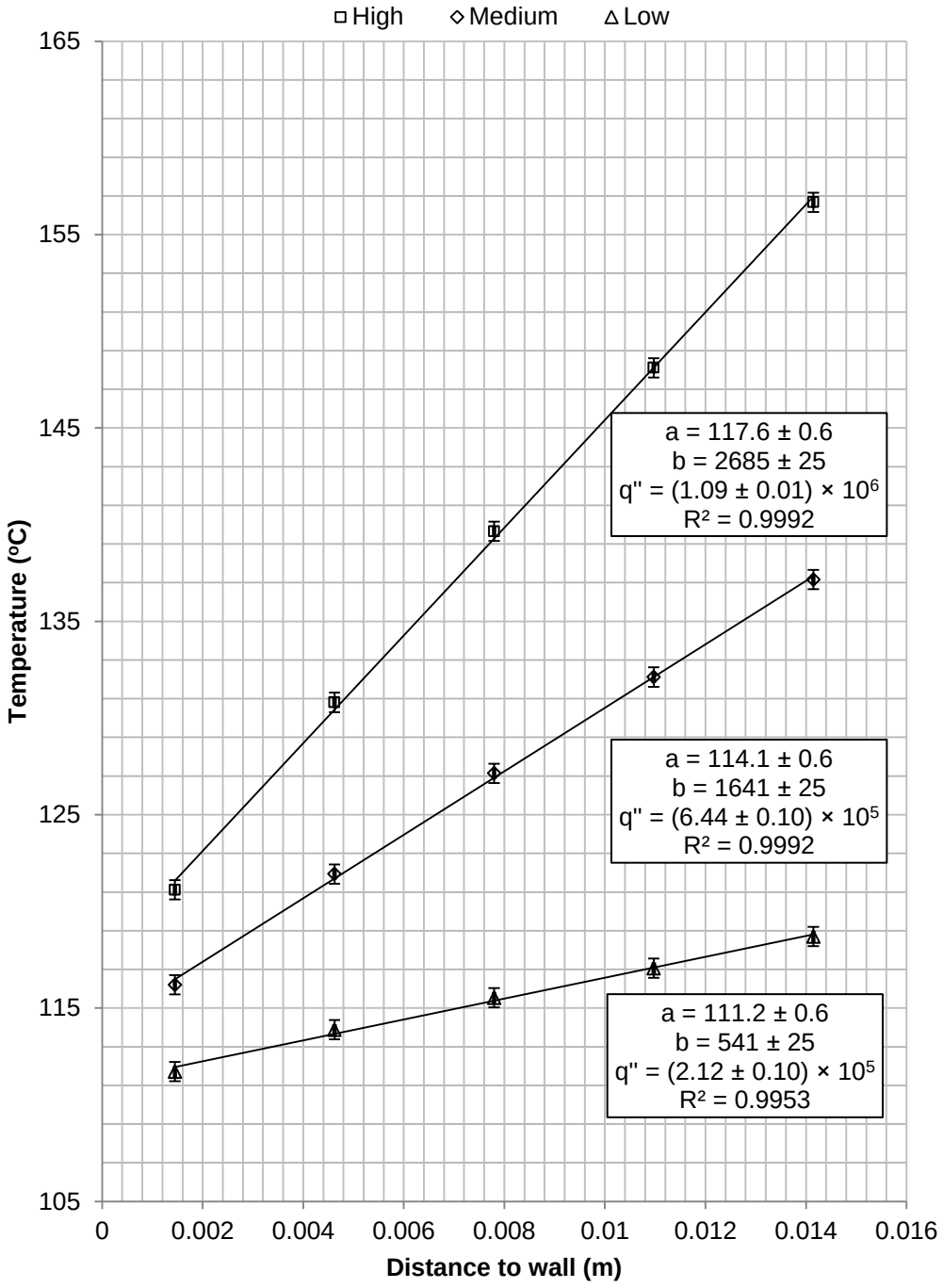

Figure C-3: Sample temperature gradient data from 23/08/2012. For each linear fit: *a* is the predicted wall temperature (^{o}C), *b* is the fitted slope (^{o}C·m^{-1}), and *q″* is the corresponding heat flux (W·m^{-2})

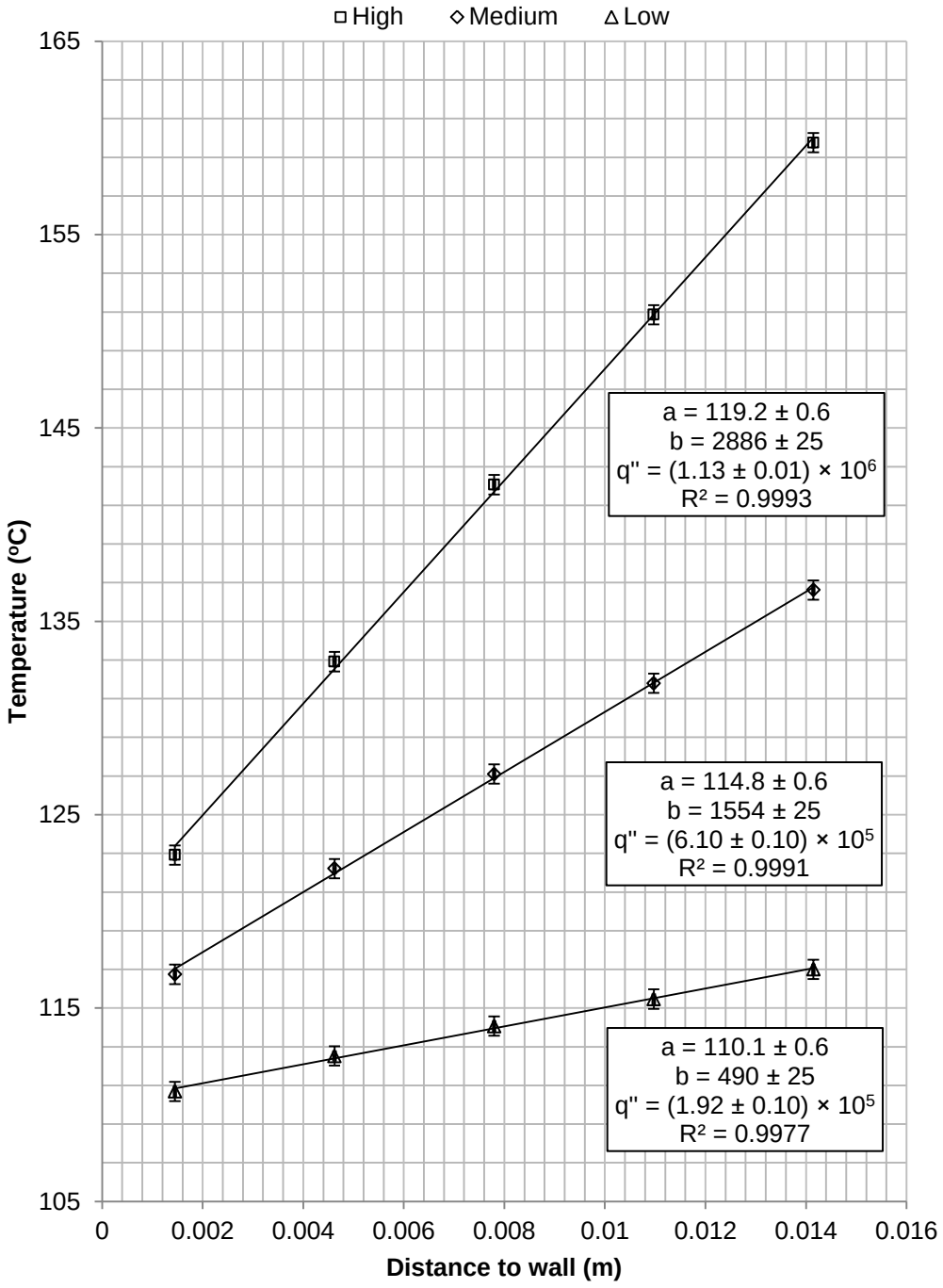

Figure C-4: Sample temperature gradient data from 27/08/2012. For each linear fit: *a* is the predicted wall temperature (^{o}C), *b* is the fitted slope (^{o}C·m^{-1}), and *q″* is the corresponding heat flux (W·m^{-2})

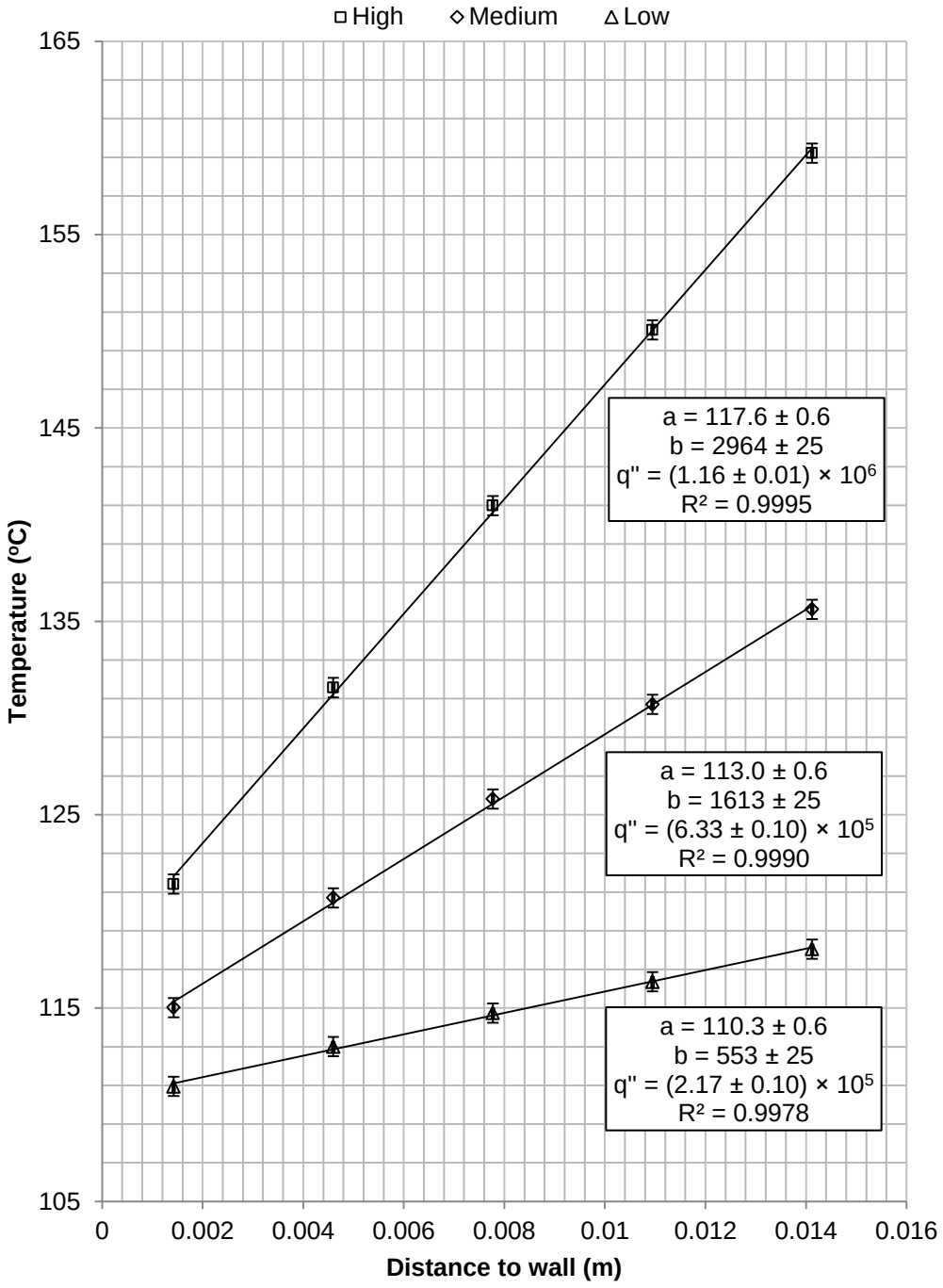

Figure C-5: Sample temperature gradient data from 29/08/2012. For each linear fit: *a* is the predicted wall temperature (^{o}C), *b* is the fitted slope (^{o}C·m^{-1}), and *q″* is the corresponding heat flux (W·m^{-2})

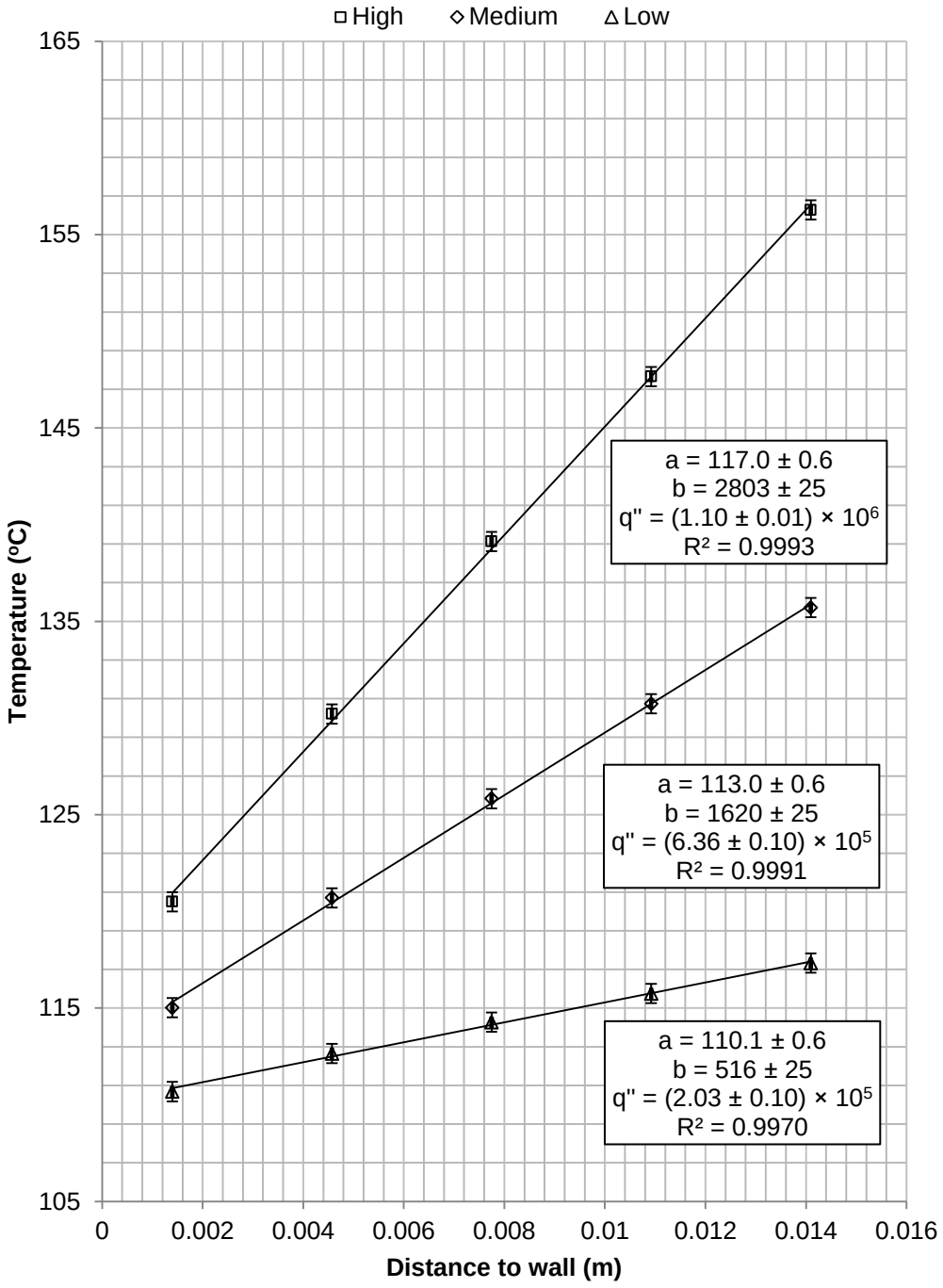

Figure C-6: Sample temperature gradient data from 18/09/2012. For each linear fit: *a* is the predicted wall temperature (ºC), *b* is the fitted slope (ºC·m^{-1}), and *q″* is the corresponding heat flux (W·m^{-2})

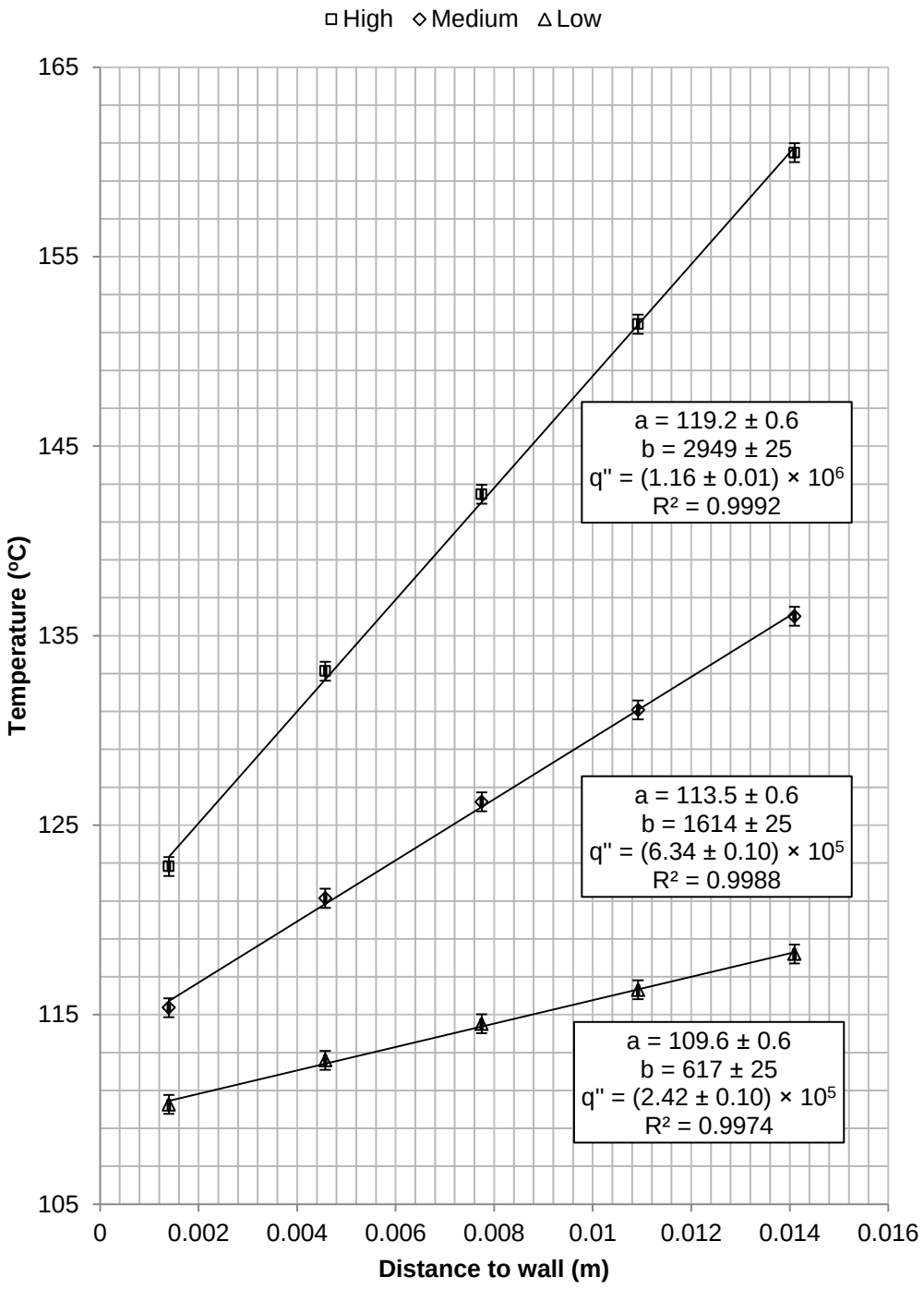

Figure C-7: Sample temperature gradient data from 20/09/2012. For each linear fit: *a* is the predicted wall temperature (°C), *b* is the fitted slope (°C·m^{-1}), and *q″* is the corresponding heat flux (W·m^{-2})

Appendix D

Boiling Facility Drawings

Construction plans for the various parts included in the new pool boiling facility are attached on the following pages. All dimensions are in inches and the selected material is indicated on each page. Please note that the drawings have been reduced from full size pages for inclusion here and as such are not to scale.

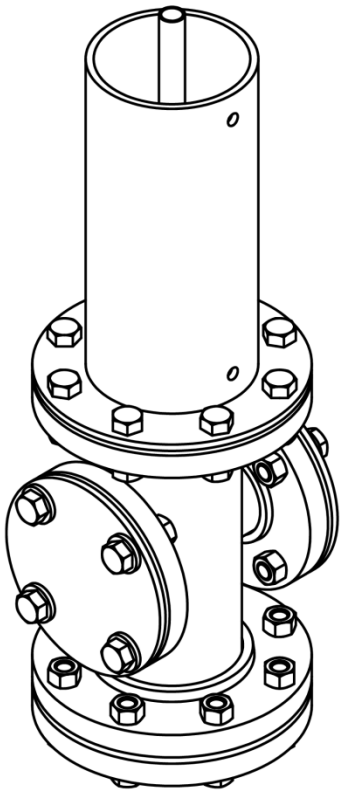

ISO (ASSEMBLED)

DRAWN James	27/10/2011	
CHECKED		
QA		TITLE
MFG		Boiling tank assembly
APPROVED		SIZE A | DWG NO full_tank_assy_v3 | REV 3
		SCALE | SHEET 1 OF 2

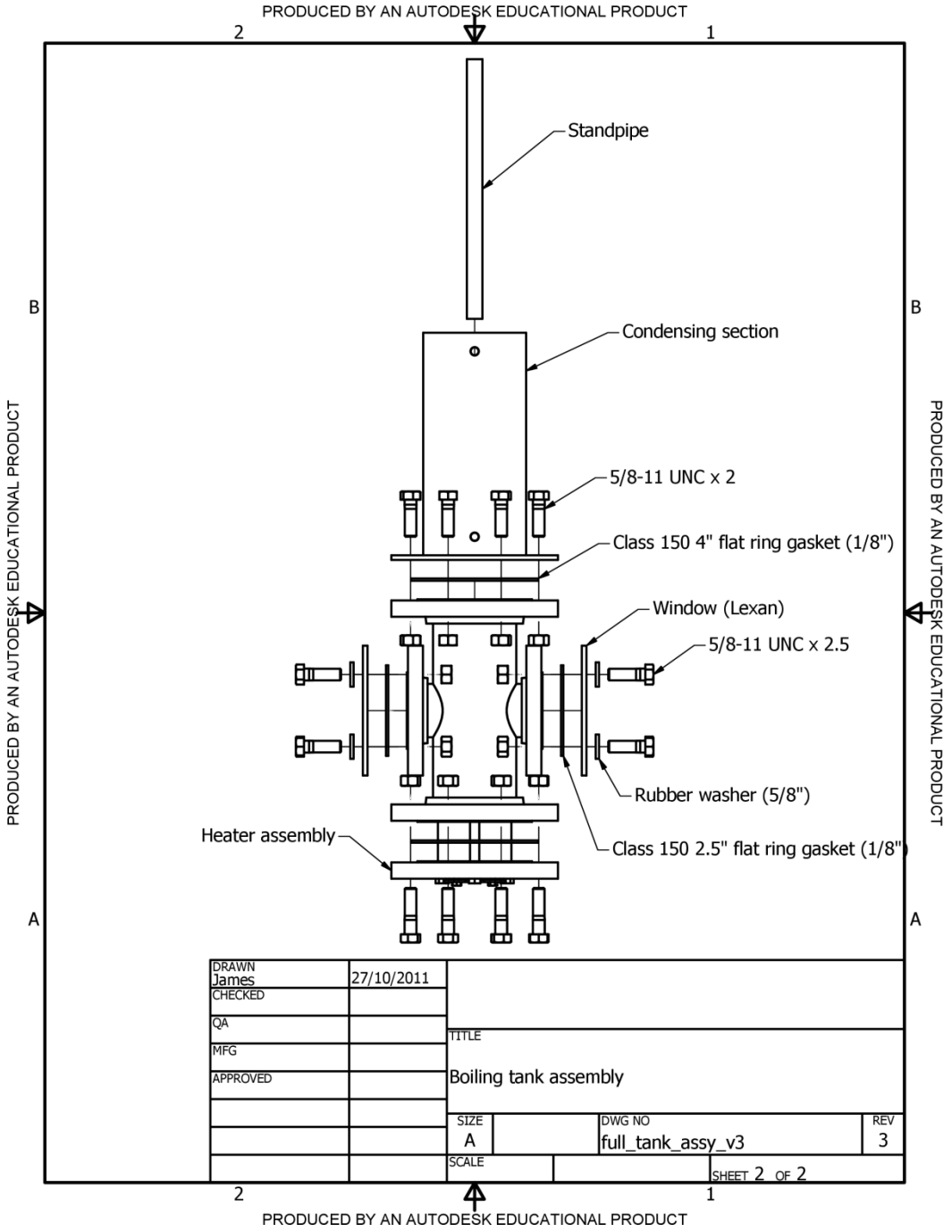
PRODUCED BY AN AUTODESK EDUCATIONAL PRODUCT
Standpipe
Condensing section
5/8-11 UNC x 2
Class 150 4" flat ring gasket (1/8")
Window (Lexan)
5/8-11 UNC x 2.5
Rubber washer (5/8")
Heater assembly
Class 150 2.5" flat ring gasket (1/8")
DRAWN James
27/10/2011
CHECKED
QA
MFG
APPROVED
TITLE
Boiling tank assembly
SIZE A
DWG NO full_tank_assy_v3
REV 3
SCALE
SHEET 2 OF 2

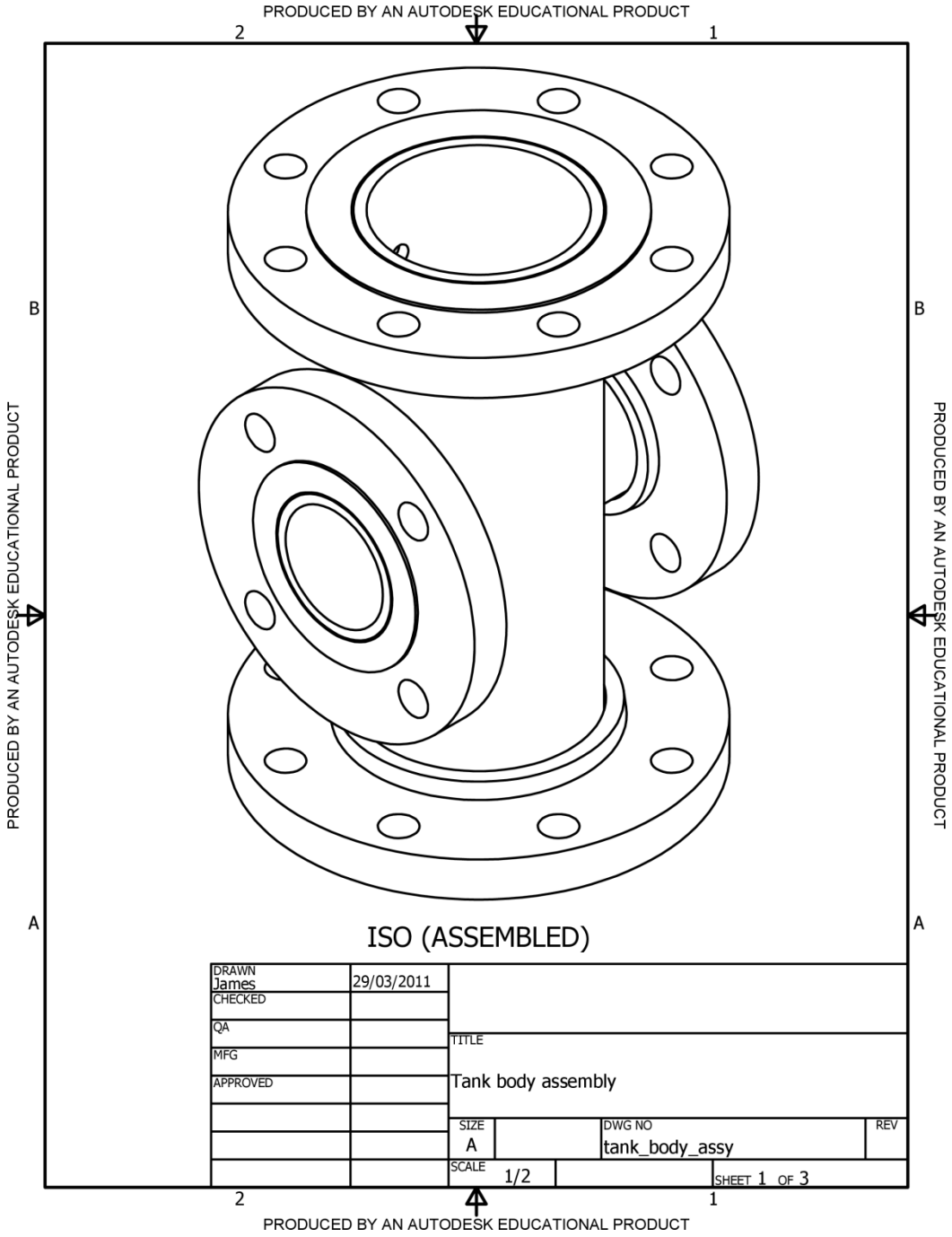
PRODUCED BY AN AUTODESK EDUCATIONAL PRODUCT
PRODUCED BY AN AUTODESK EDUCATIONAL PRODUCT
PRODUCED BY AN AUTODESK EDUCATIONAL PRODUCT
PRODUCED BY AN AUTODESK EDUCATIONAL PRODUCT
ISO (ASSEMBLED)
DRAWN James 29/03/2011
CHECKED
QA
MFG
APPROVED
TITLE
Tank body assembly
SIZE A
DWG NO tank_body_assy
REV
SCALE 1/2
SHEET 1 OF 3

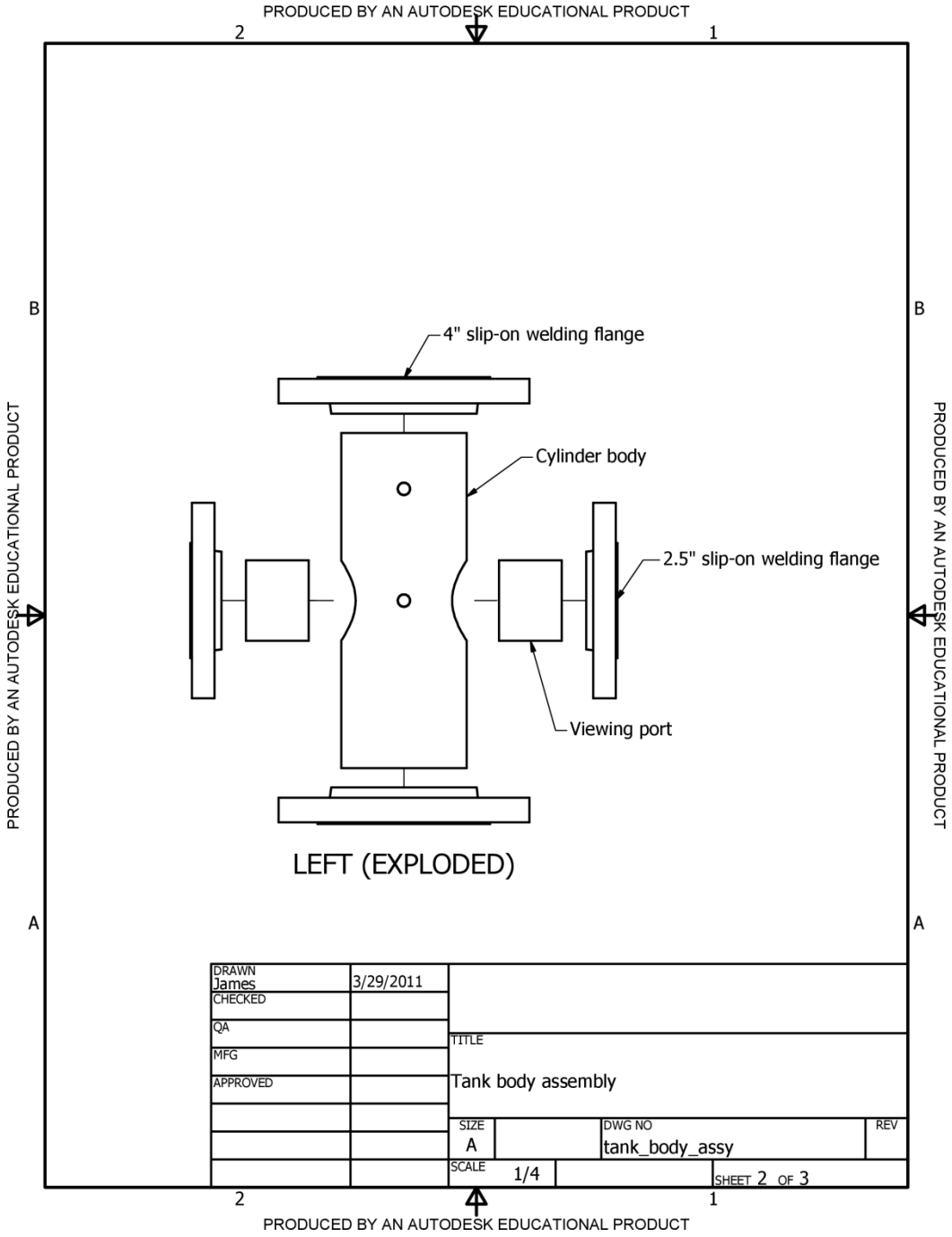
PRODUCED BY AN AUTODESK EDUCATIONAL PRODUCT
PRODUCED BY AN AUTODESK EDUCATIONAL PRODUCT
PRODUCED BY AN AUTODESK EDUCATIONAL PRODUCT
PRODUCED BY AN AUTODESK EDUCATIONAL PRODUCT
4" slip-on welding flange
Cylinder body
2.5" slip-on welding flange
Viewing port
LEFT (EXPLODED)
DRAWN James 3/29/2011
CHECKED
QA
MFG
APPROVED
TITLE
Tank body assembly
SIZE A
DWG NO tank_body_assy
REV
SCALE 1/4
SHEET 2 OF 3

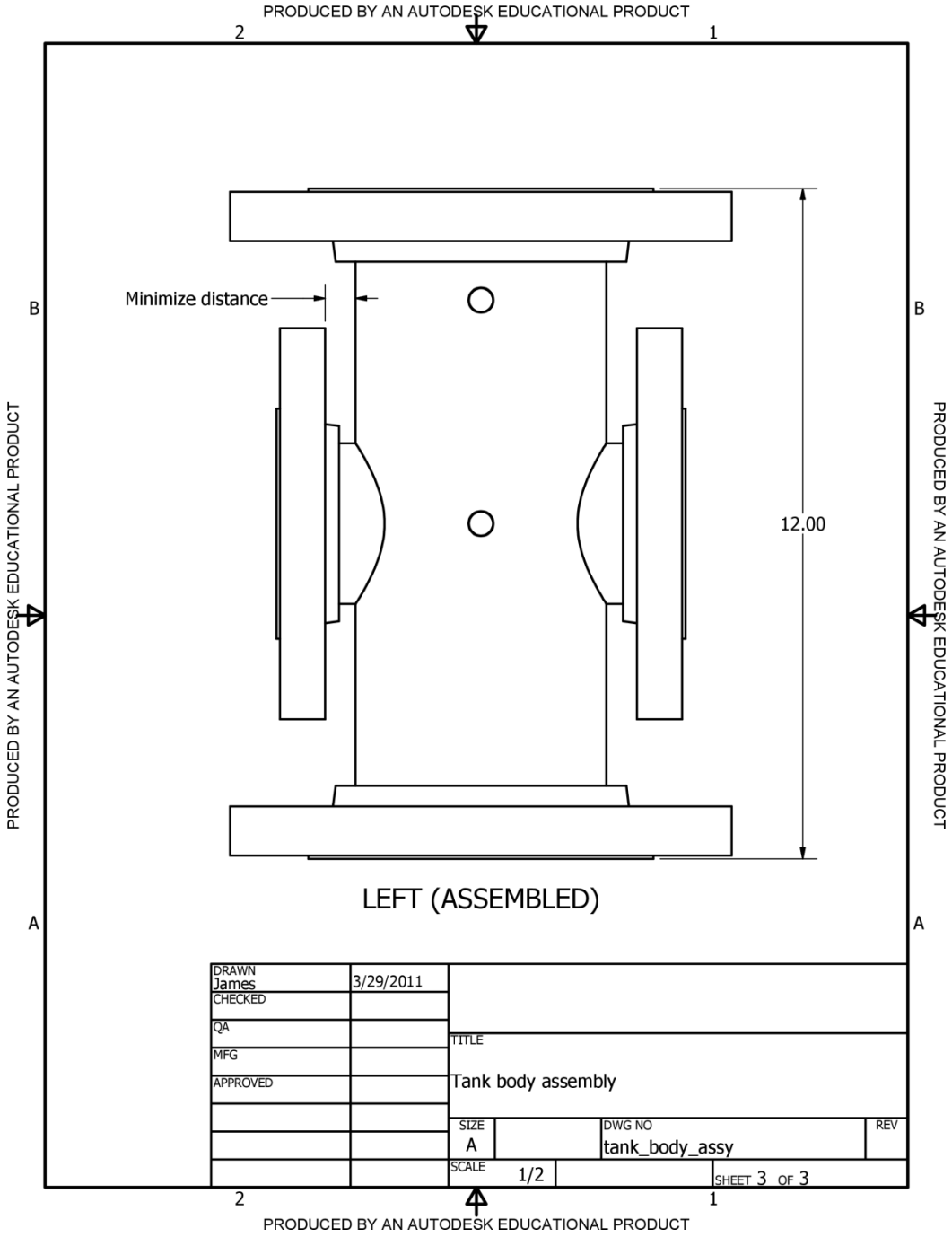
PRODUCED BY AN AUTODESK EDUCATIONAL PRODUCT
Minimize distance
12.00
LEFT (ASSEMBLED)
DRAWN James 3/29/2011
CHECKED
QA
MFG
APPROVED
TITLE
Tank body assembly
SIZE A
DWG NO tank_body_assy
REV
SCALE 1/2
SHEET 3 OF 3

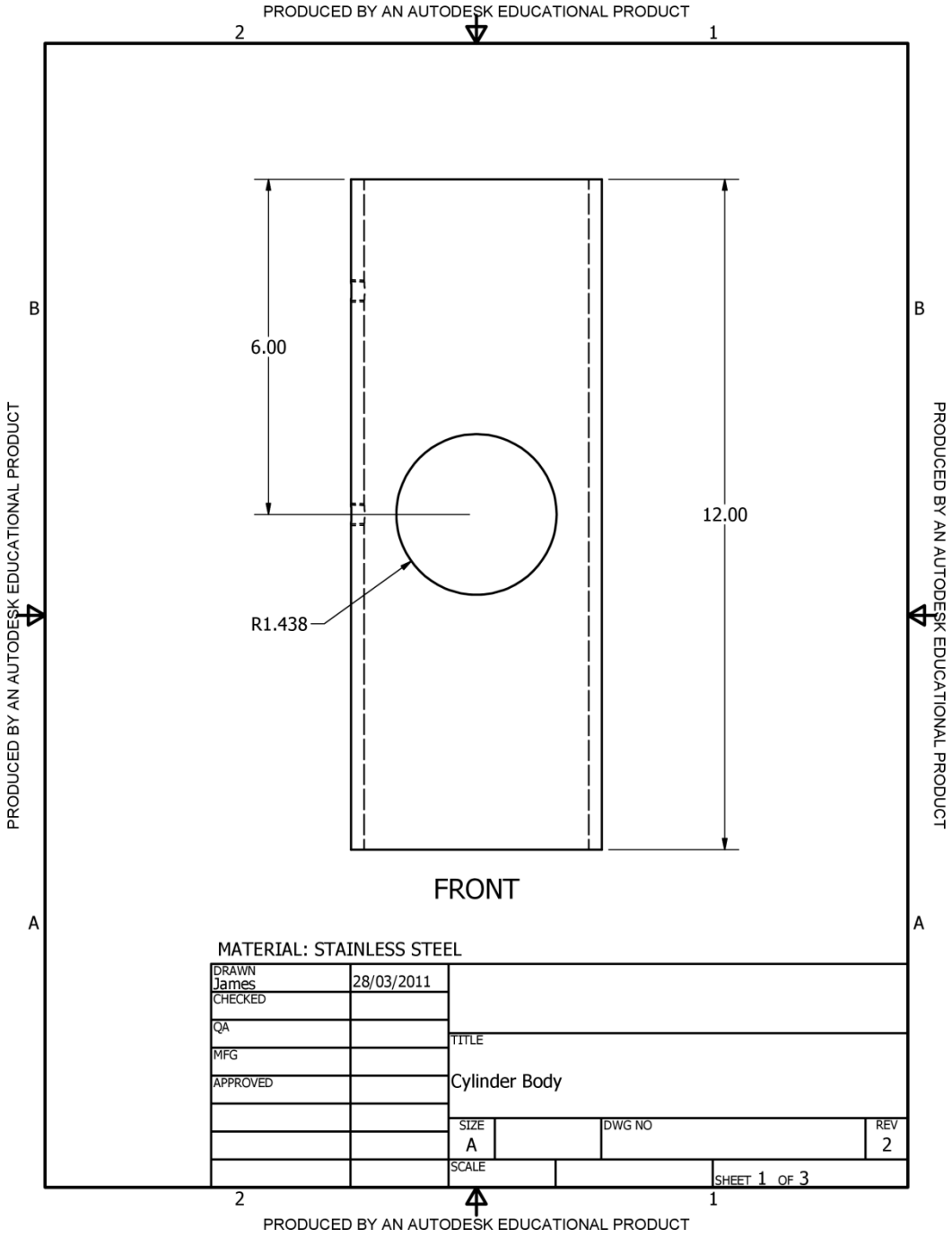
PRODUCED BY AN AUTODESK EDUCATIONAL PRODUCT
PRODUCED BY AN AUTODESK EDUCATIONAL PRODUCT
PRODUCED BY AN AUTODESK EDUCATIONAL PRODUCT
PRODUCED BY AN AUTODESK EDUCATIONAL PRODUCT
6.00
12.00
R1.438
FRONT
MATERIAL: STAINLESS STEEL
DRAWN James 28/03/2011
CHECKED
QA
MFG
APPROVED
TITLE
Cylinder Body
SIZE A
DWG NO
REV 2
SCALE
SHEET 1 OF 3

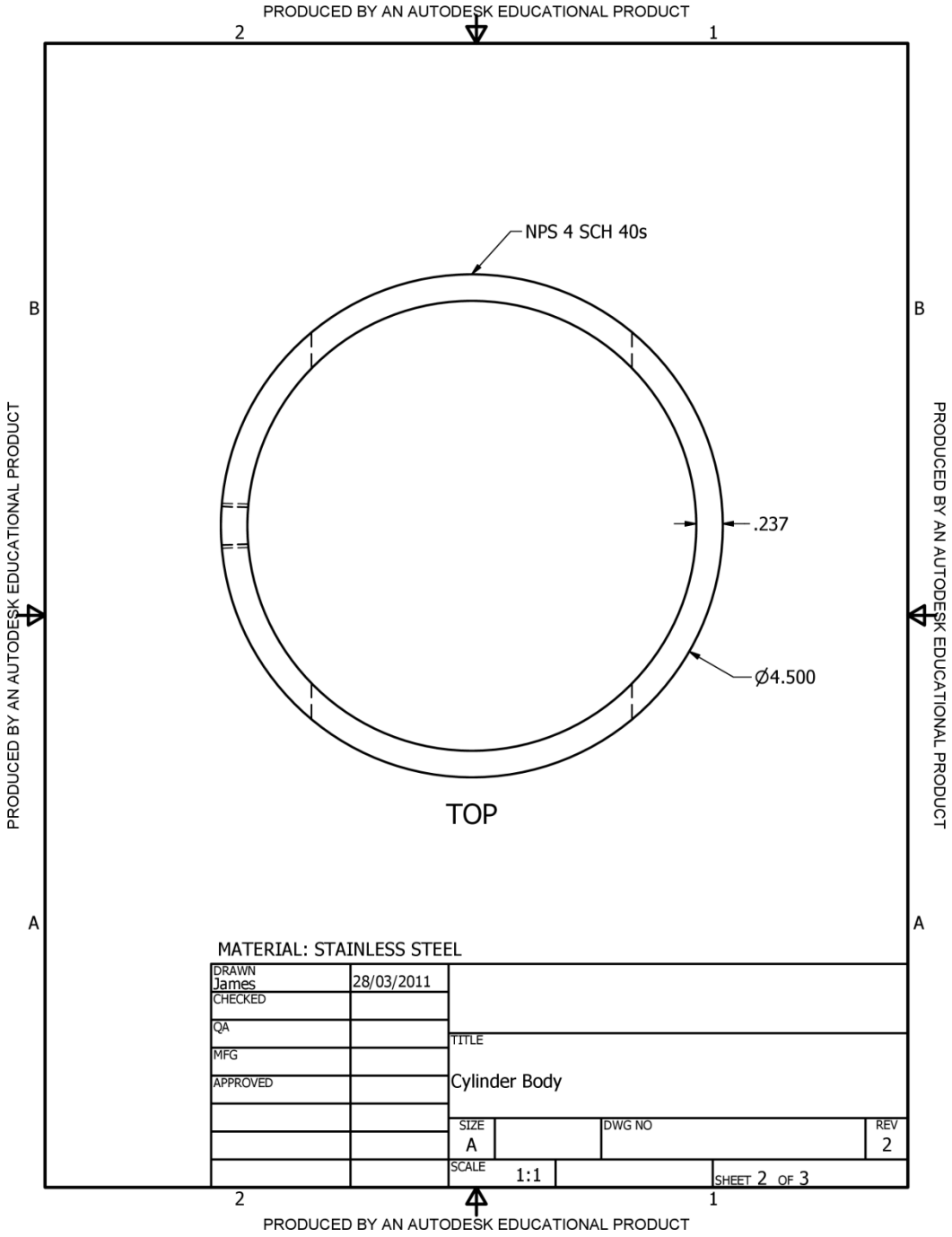
PRODUCED BY AN AUTODESK EDUCATIONAL PRODUCT
NPS 4 SCH 40s
.237
Ø4.500
TOP
MATERIAL: STAINLESS STEEL
DRAWN James 28/03/2011
CHECKED
QA
MFG
APPROVED
TITLE
Cylinder Body
SIZE A
DWG NO
REV 2
SCALE 1:1
SHEET 2 OF 3

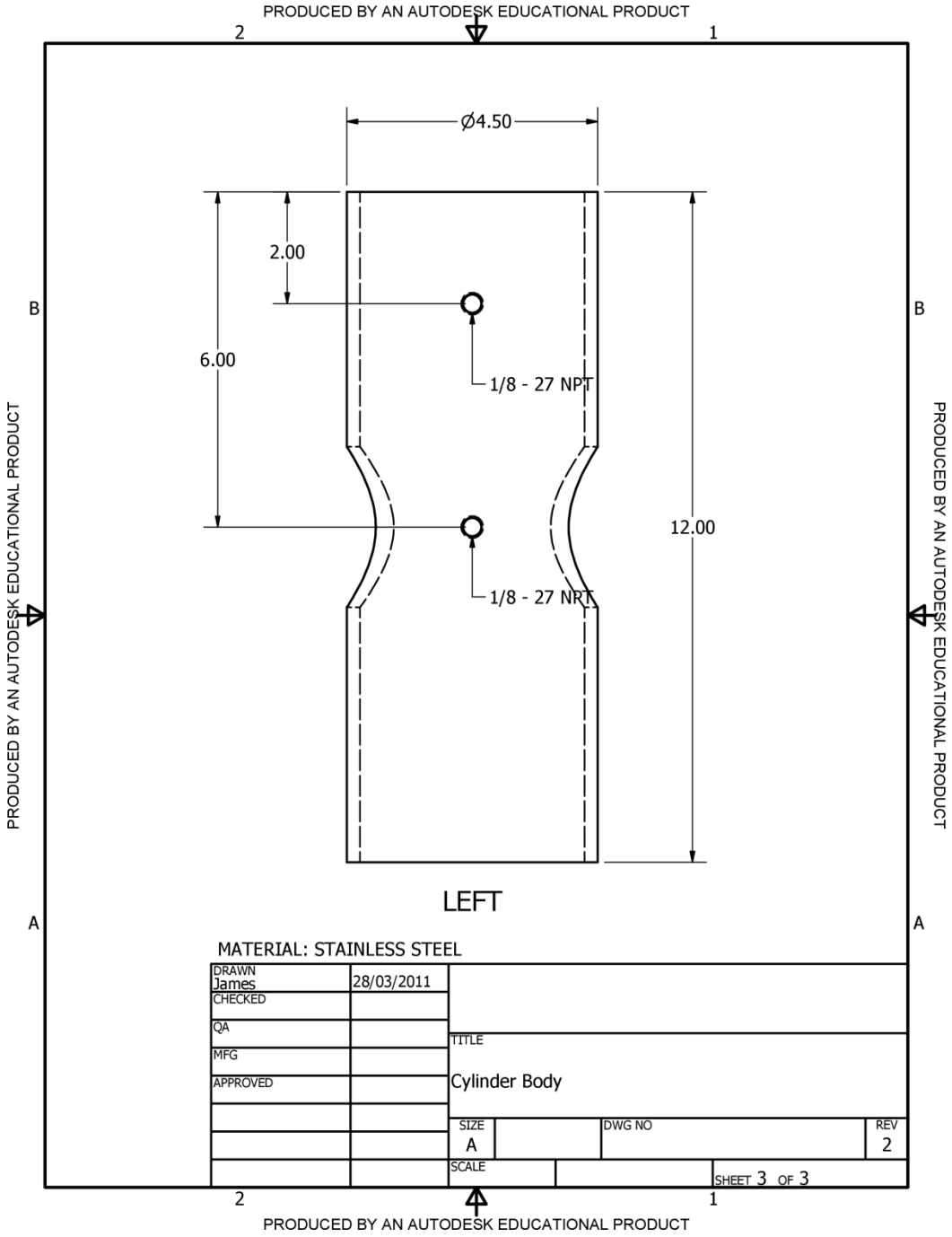
PRODUCED BY AN AUTODESK EDUCATIONAL PRODUCT
Ø4.50
2.00
6.00
12.00
1/8 - 27 NPT
1/8 - 27 NPT
LEFT
MATERIAL: STAINLESS STEEL
DRAWN James 28/03/2011
CHECKED
QA
MFG
APPROVED
TITLE
Cylinder Body
SIZE A
DWG NO
REV 2
SCALE
SHEET 3 OF 3

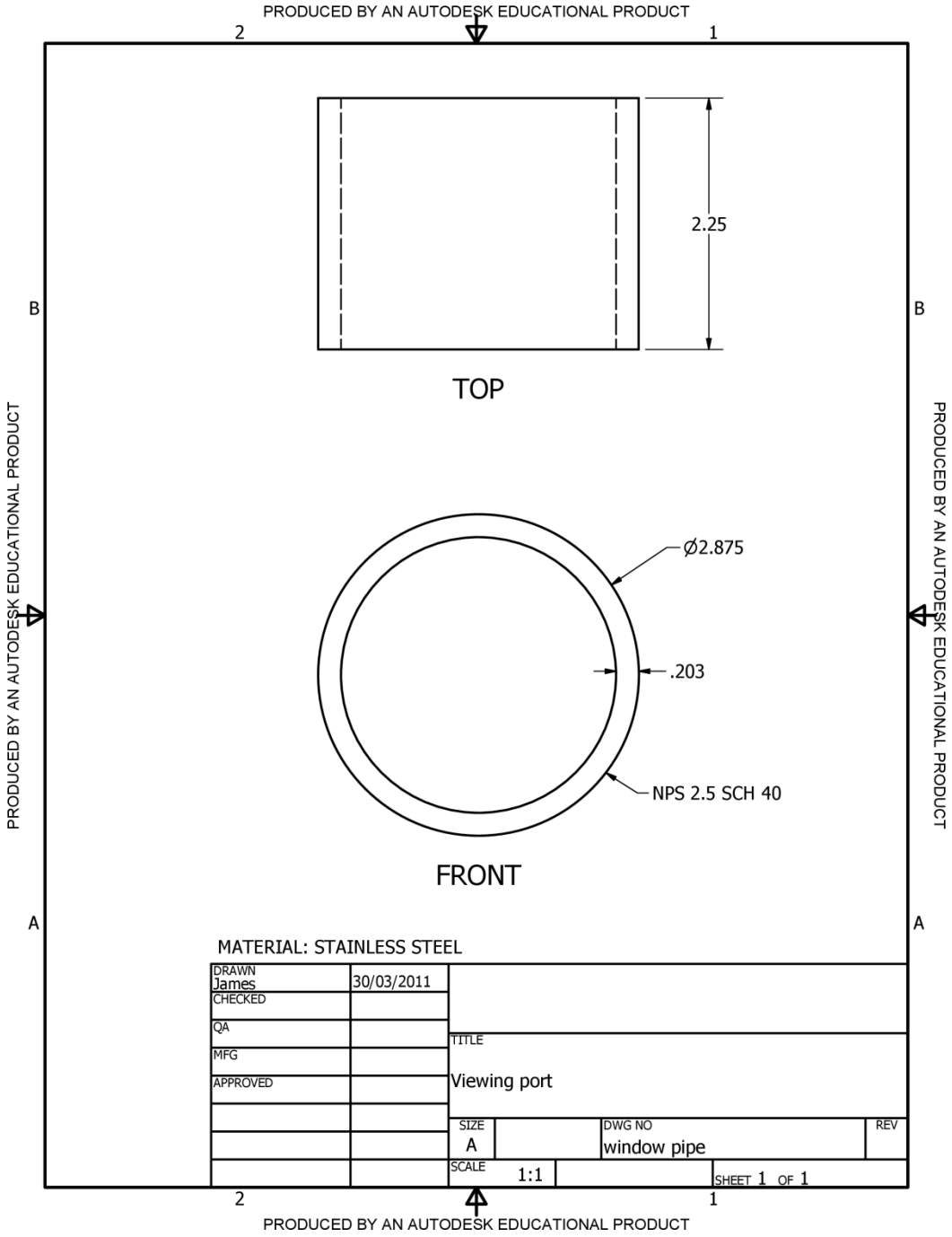
PRODUCED BY AN AUTODESK EDUCATIONAL PRODUCT
2.25
TOP
Ø2.875
.203
NPS 2.5 SCH 40
FRONT
MATERIAL: STAINLESS STEEL
DRAWN James 30/03/2011
CHECKED
QA
MFG
APPROVED
TITLE
Viewing port
SIZE A
DWG NO window pipe
REV
SCALE 1:1
SHEET 1 OF 1

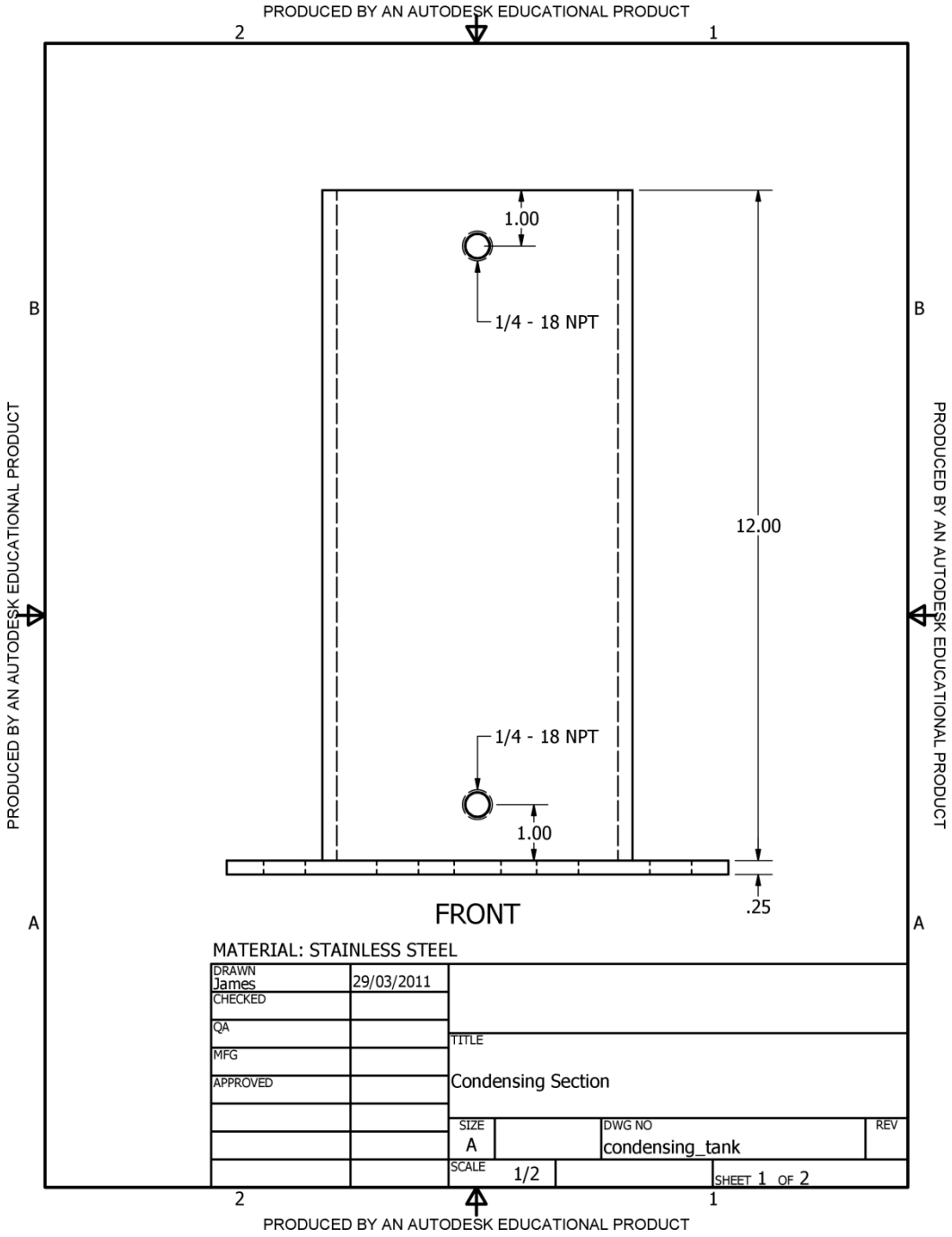
PRODUCED BY AN AUTODESK EDUCATIONAL PRODUCT
1.00
1/4 - 18 NPT
12.00
1/4 - 18 NPT
1.00
.25
FRONT
MATERIAL: STAINLESS STEEL
DRAWN James 29/03/2011
CHECKED
QA
MFG
APPROVED
TITLE
Condensing Section
SIZE A
DWG NO condensing_tank
REV
SCALE 1/2
SHEET 1 OF 2

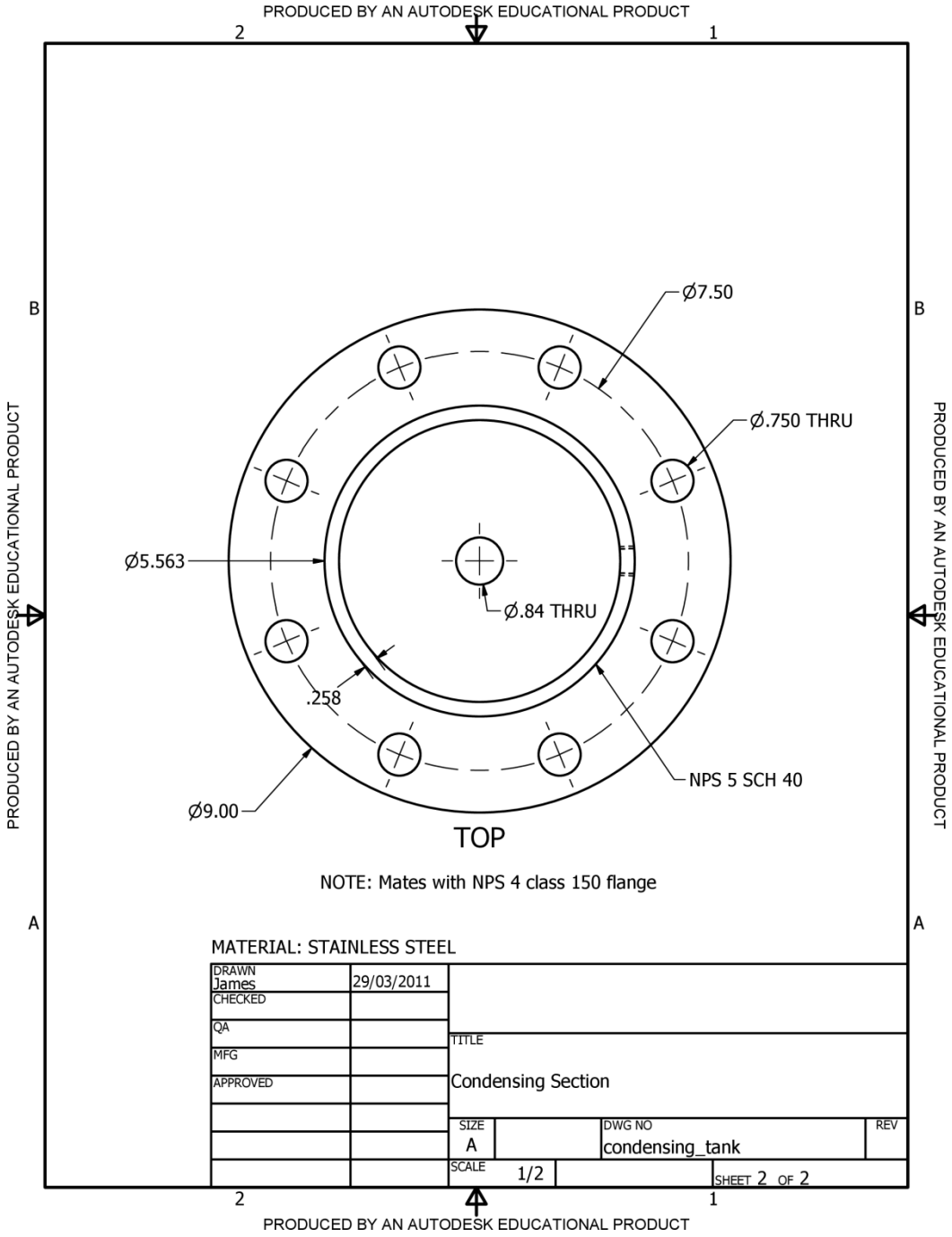
PRODUCED BY AN AUTODESK EDUCATIONAL PRODUCT
PRODUCED BY AN AUTODESK EDUCATIONAL PRODUCT
PRODUCED BY AN AUTODESK EDUCATIONAL PRODUCT
PRODUCED BY AN AUTODESK EDUCATIONAL PRODUCT
Ø7.50
Ø.750 THRU
Ø5.563
Ø.84 THRU
.258
NPS 5 SCH 40
Ø9.00
TOP
NOTE: Mates with NPS 4 class 150 flange
MATERIAL: STAINLESS STEEL
DRAWN James 29/03/2011
CHECKED
QA
MFG
APPROVED
TITLE
Condensing Section
SIZE A
DWG NO condensing_tank
REV
SCALE 1/2
SHEET 2 OF 2

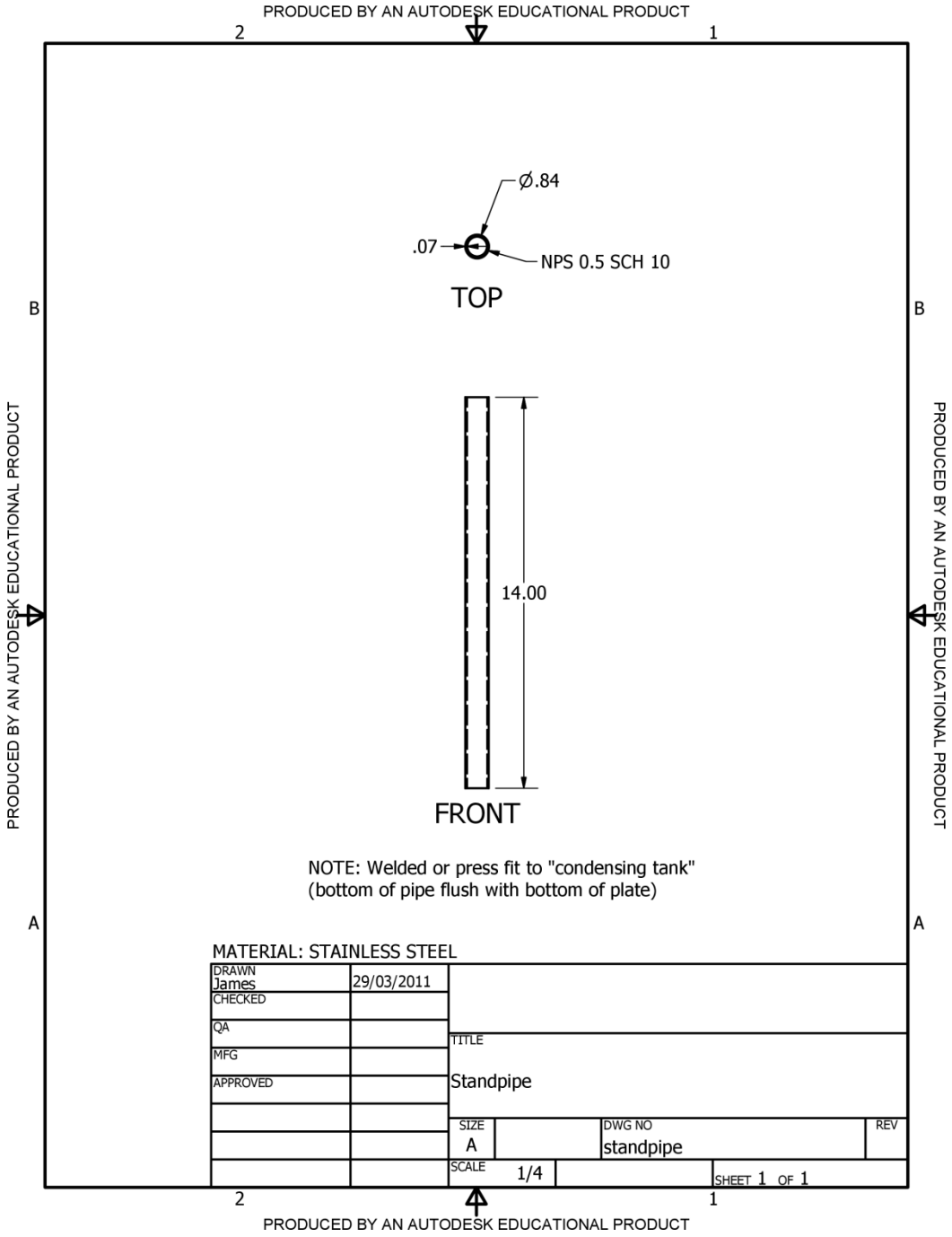
PRODUCED BY AN AUTODESK EDUCATIONAL PRODUCT
Ø.84
.07
NPS 0.5 SCH 10
TOP
14.00
FRONT
NOTE: Welded or press fit to "condensing tank"
(bottom of pipe flush with bottom of plate)
MATERIAL: STAINLESS STEEL
DRAWN James 29/03/2011
CHECKED
QA
MFG
APPROVED
TITLE
Standpipe
SIZE A
DWG NO standpipe
REV
SCALE 1/4
SHEET 1 OF 1

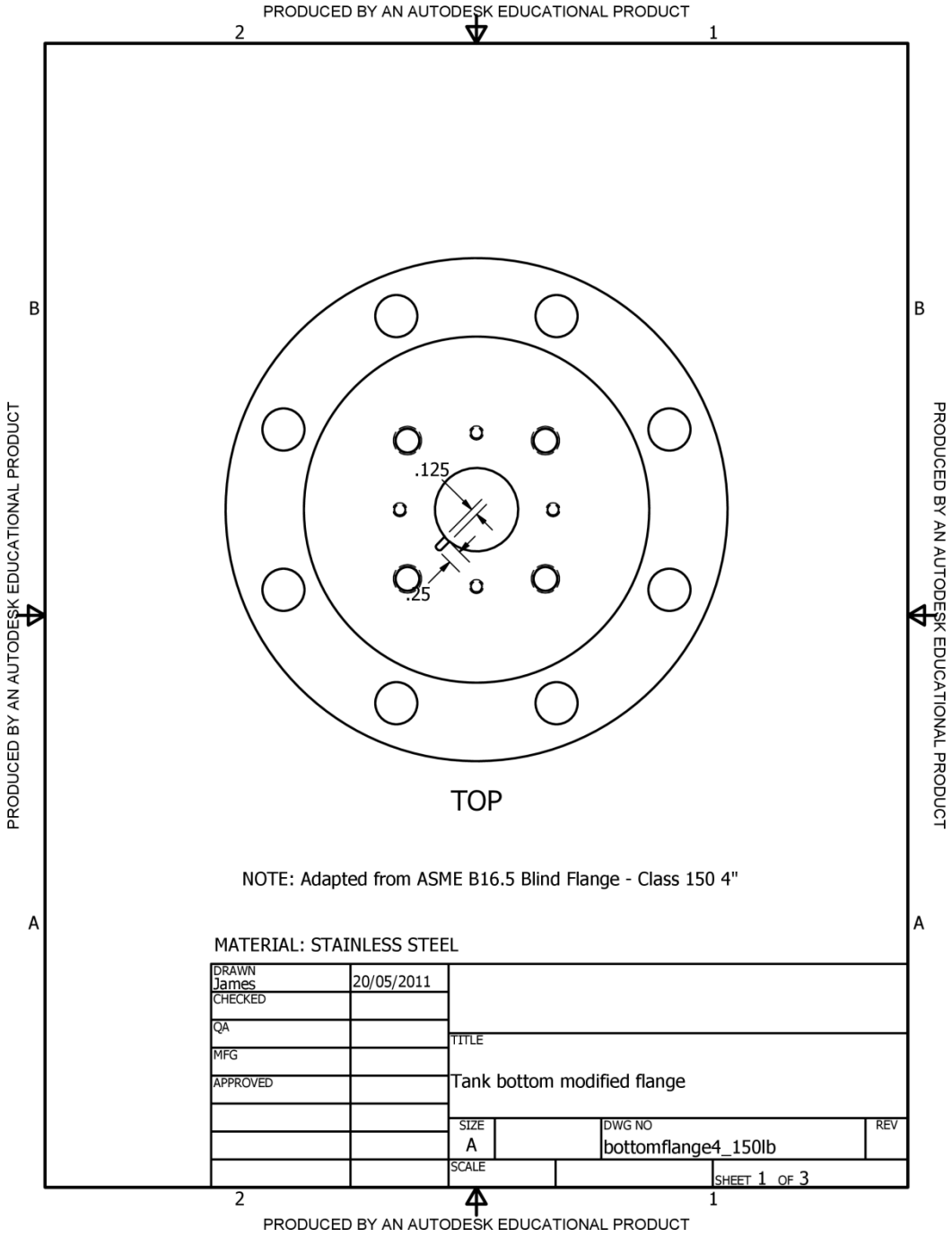
PRODUCED BY AN AUTODESK EDUCATIONAL PRODUCT
PRODUCED BY AN AUTODESK EDUCATIONAL PRODUCT
PRODUCED BY AN AUTODESK EDUCATIONAL PRODUCT
PRODUCED BY AN AUTODESK EDUCATIONAL PRODUCT
.125
.25
TOP
NOTE: Adapted from ASME B16.5 Blind Flange - Class 150 4"
MATERIAL: STAINLESS STEEL
DRAWN James 20/05/2011
CHECKED
QA
MFG
APPROVED
TITLE
Tank bottom modified flange
SIZE A
DWG NO bottomflange4_150lb
REV
SCALE
SHEET 1 OF 3

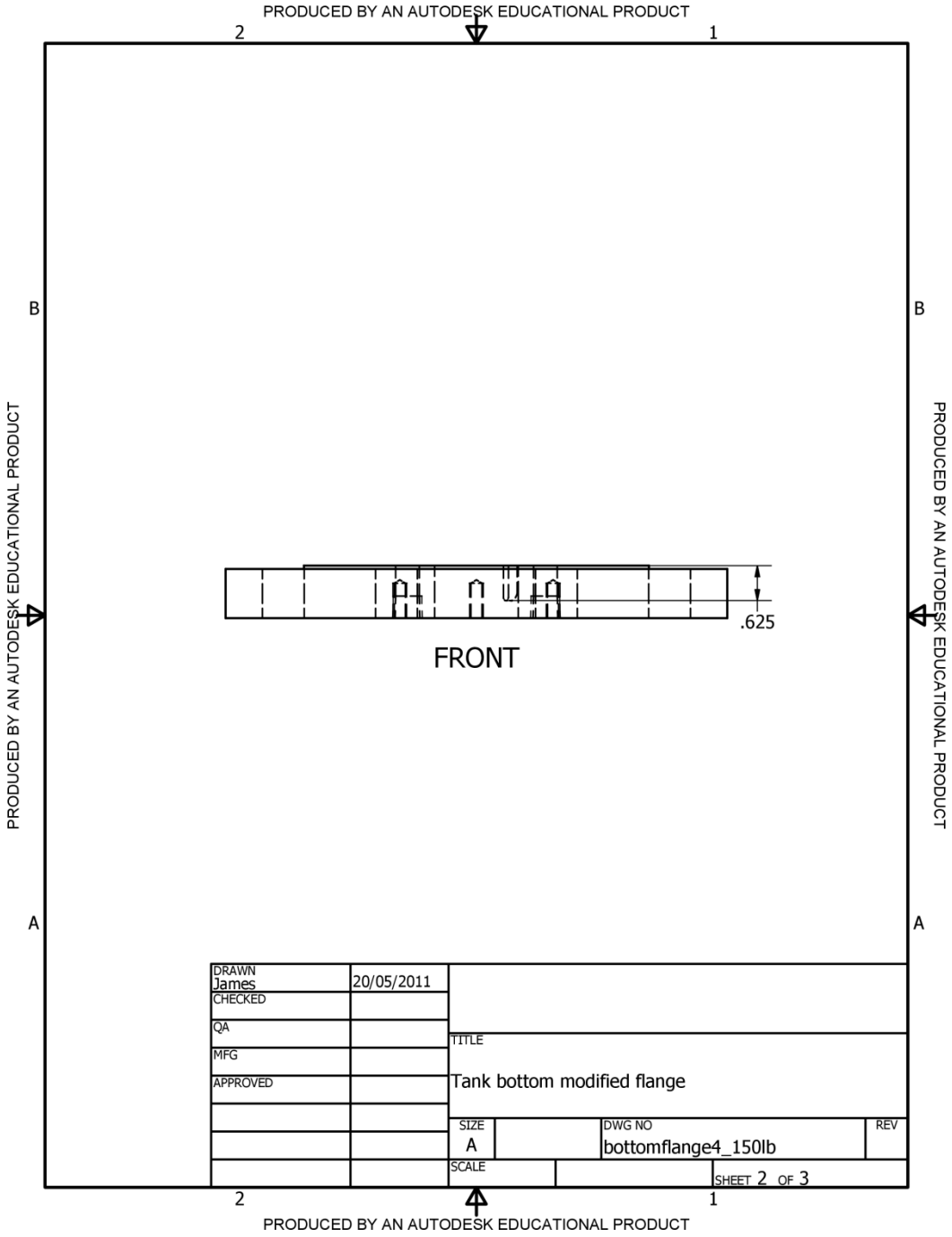
PRODUCED BY AN AUTODESK EDUCATIONAL PRODUCT
PRODUCED BY AN AUTODESK EDUCATIONAL PRODUCT
PRODUCED BY AN AUTODESK EDUCATIONAL PRODUCT
PRODUCED BY AN AUTODESK EDUCATIONAL PRODUCT
.625
FRONT
DRAWN James
20/05/2011
CHECKED
QA
MFG
APPROVED
TITLE
Tank bottom modified flange
SIZE A
DWG NO bottomflange4_150lb
REV
SCALE
SHEET 2 OF 3

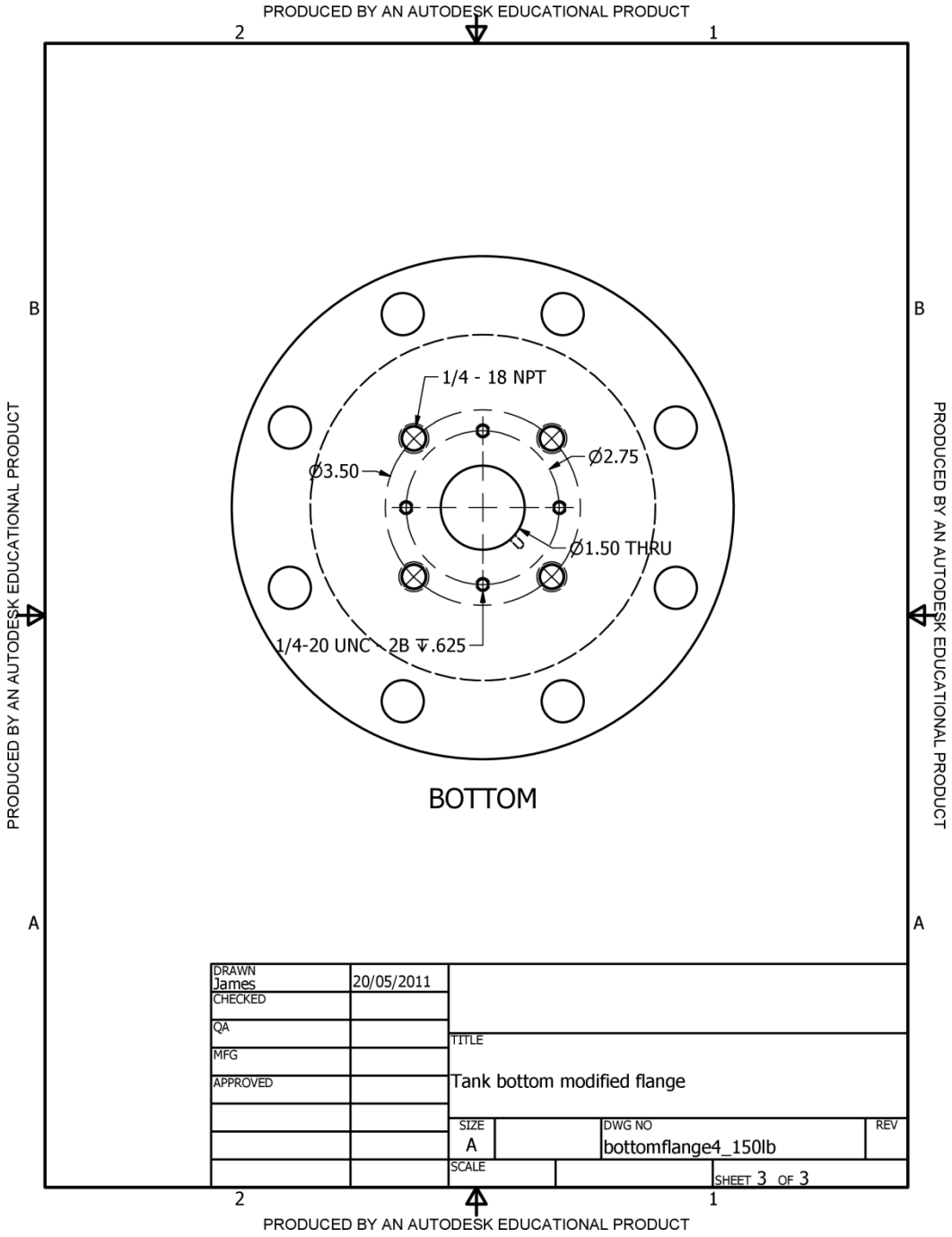
PRODUCED BY AN AUTODESK EDUCATIONAL PRODUCT
PRODUCED BY AN AUTODESK EDUCATIONAL PRODUCT
PRODUCED BY AN AUTODESK EDUCATIONAL PRODUCT
PRODUCED BY AN AUTODESK EDUCATIONAL PRODUCT
1/4 - 18 NPT
Ø3.50
Ø2.75
Ø1.50 THRU
1/4-20 UNC - 2B ↧.625
BOTTOM
DRAWN James 20/05/2011
CHECKED
QA
MFG
APPROVED
TITLE
Tank bottom modified flange
SIZE A
DWG NO bottomflange4_150lb
REV
SCALE
SHEET 3 OF 3

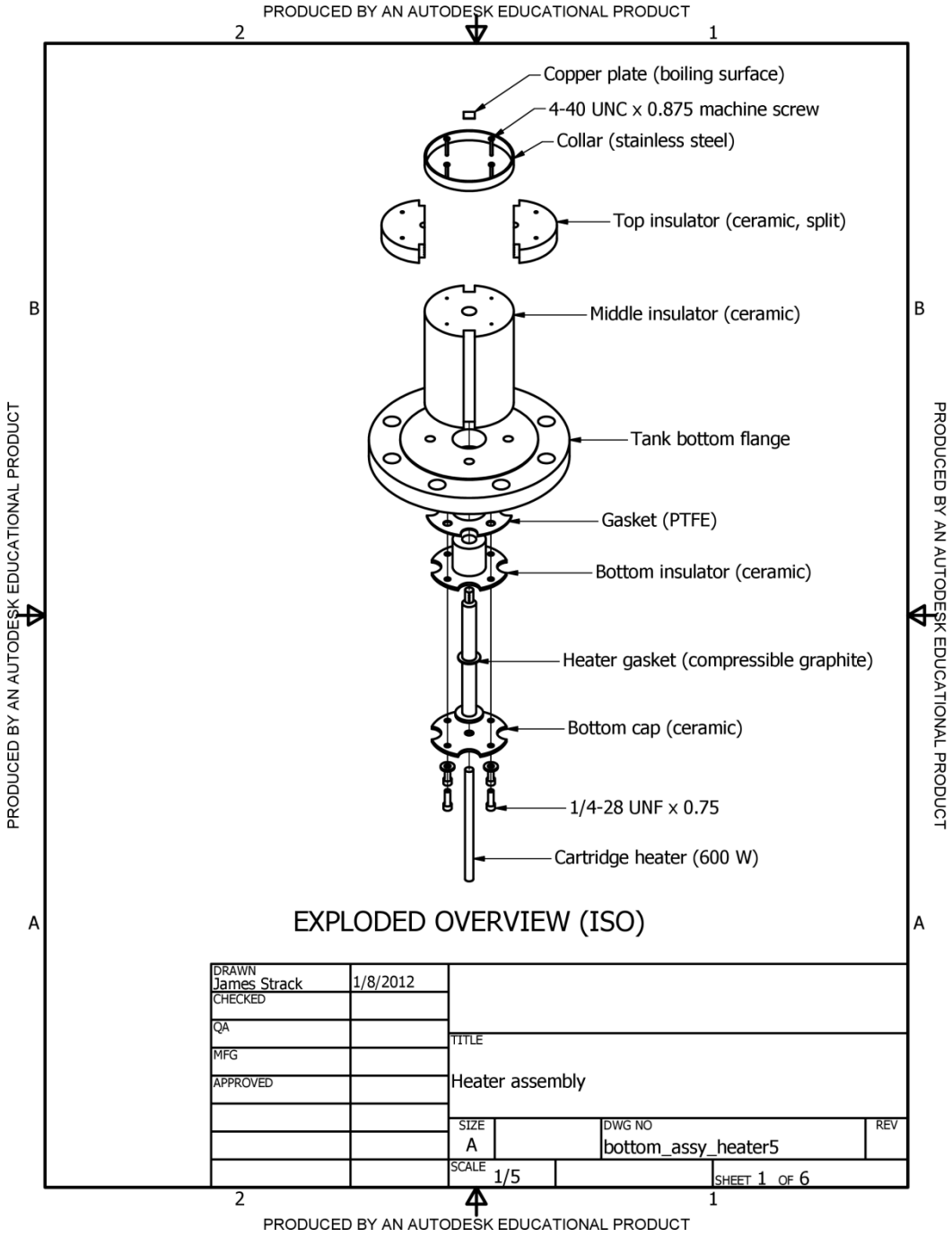
PRODUCED BY AN AUTODESK EDUCATIONAL PRODUCT
Copper plate (boiling surface)
4-40 UNC x 0.875 machine screw
Collar (stainless steel)
Top insulator (ceramic, split)
Middle insulator (ceramic)
Tank bottom flange
Gasket (PTFE)
Bottom insulator (ceramic)
Heater gasket (compressible graphite)
Bottom cap (ceramic)
1/4-28 UNF x 0.75
Cartridge heater (600 W)
EXPLODED OVERVIEW (ISO)
DRAWN James Strack 1/8/2012
CHECKED
QA
MFG
APPROVED
TITLE
Heater assembly
SIZE A
DWG NO bottom_assy_heater5
REV
SCALE 1/5
SHEET 1 OF 6

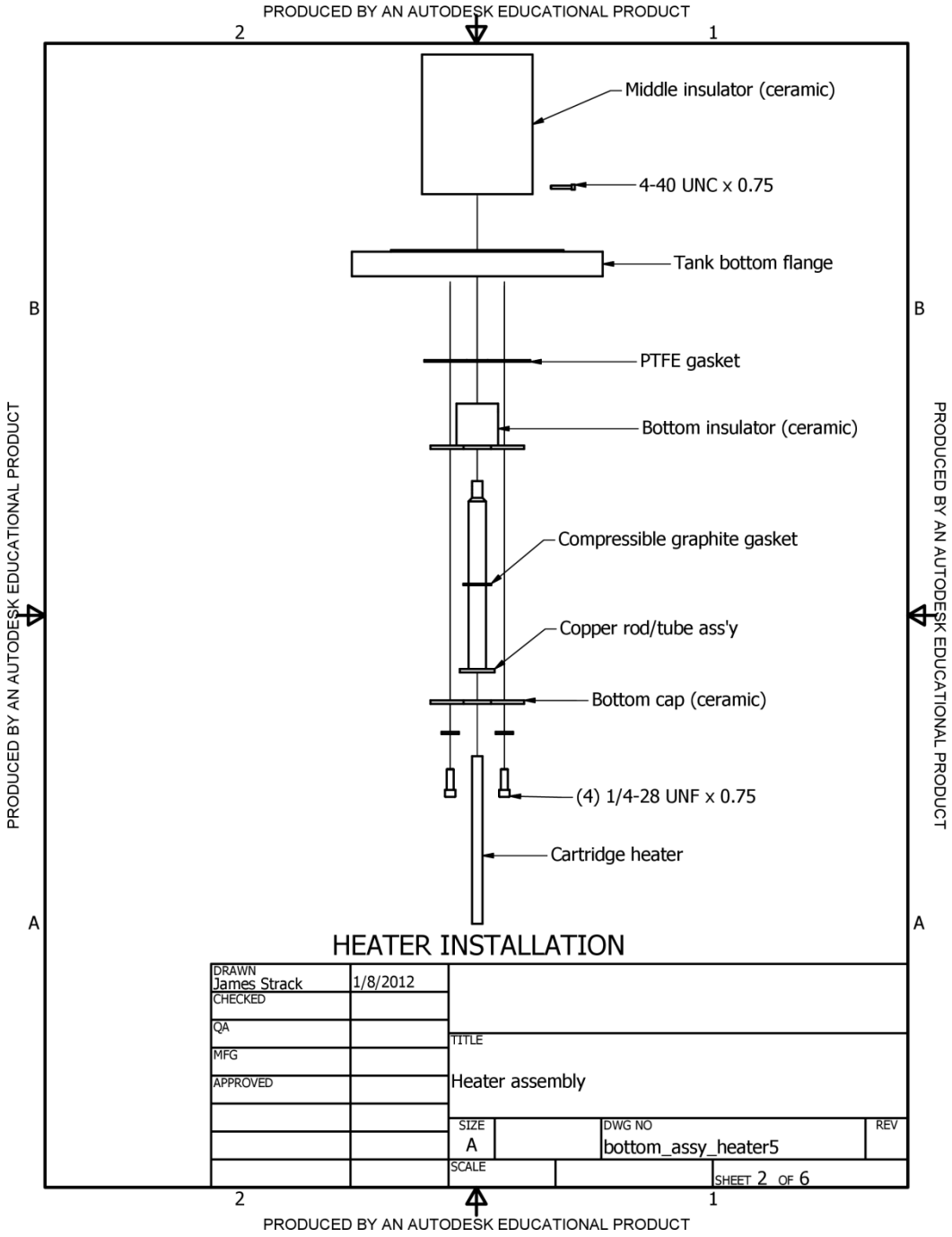
PRODUCED BY AN AUTODESK EDUCATIONAL PRODUCT
Middle insulator (ceramic)
4-40 UNC x 0.75
Tank bottom flange
PTFE gasket
Bottom insulator (ceramic)
Compressible graphite gasket
Copper rod/tube ass'y
Bottom cap (ceramic)
(4) 1/4-28 UNF x 0.75
Cartridge heater
HEATER INSTALLATION
DRAWN James Strack 1/8/2012
CHECKED
QA
MFG
APPROVED
TITLE
Heater assembly
SIZE A
DWG NO bottom_assy_heater5
REV
SCALE
SHEET 2 OF 6

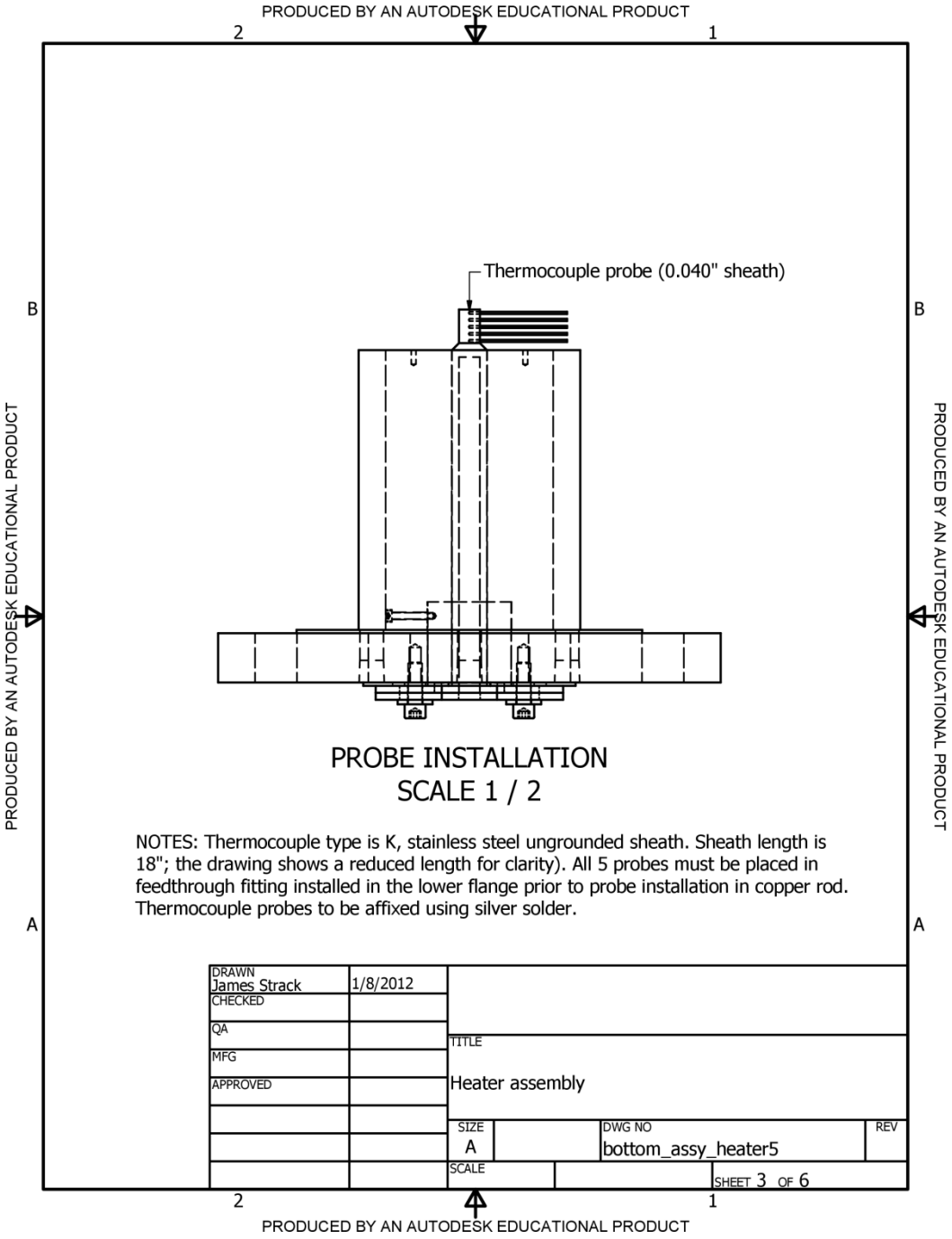
PRODUCED BY AN AUTODESK EDUCATIONAL PRODUCT
Thermocouple probe (0.040" sheath)
PROBE INSTALLATION
SCALE 1 / 2
NOTES: Thermocouple type is K, stainless steel ungrounded sheath. Sheath length is 18"; the drawing shows a reduced length for clarity). All 5 probes must be placed in feedthrough fitting installed in the lower flange prior to probe installation in copper rod. Thermocouple probes to be affixed using silver solder.
DRAWN James Strack 1/8/2012
CHECKED
QA
MFG
APPROVED
TITLE
Heater assembly
SIZE A
DWG NO bottom_assy_heater5
REV
SCALE
SHEET 3 OF 6

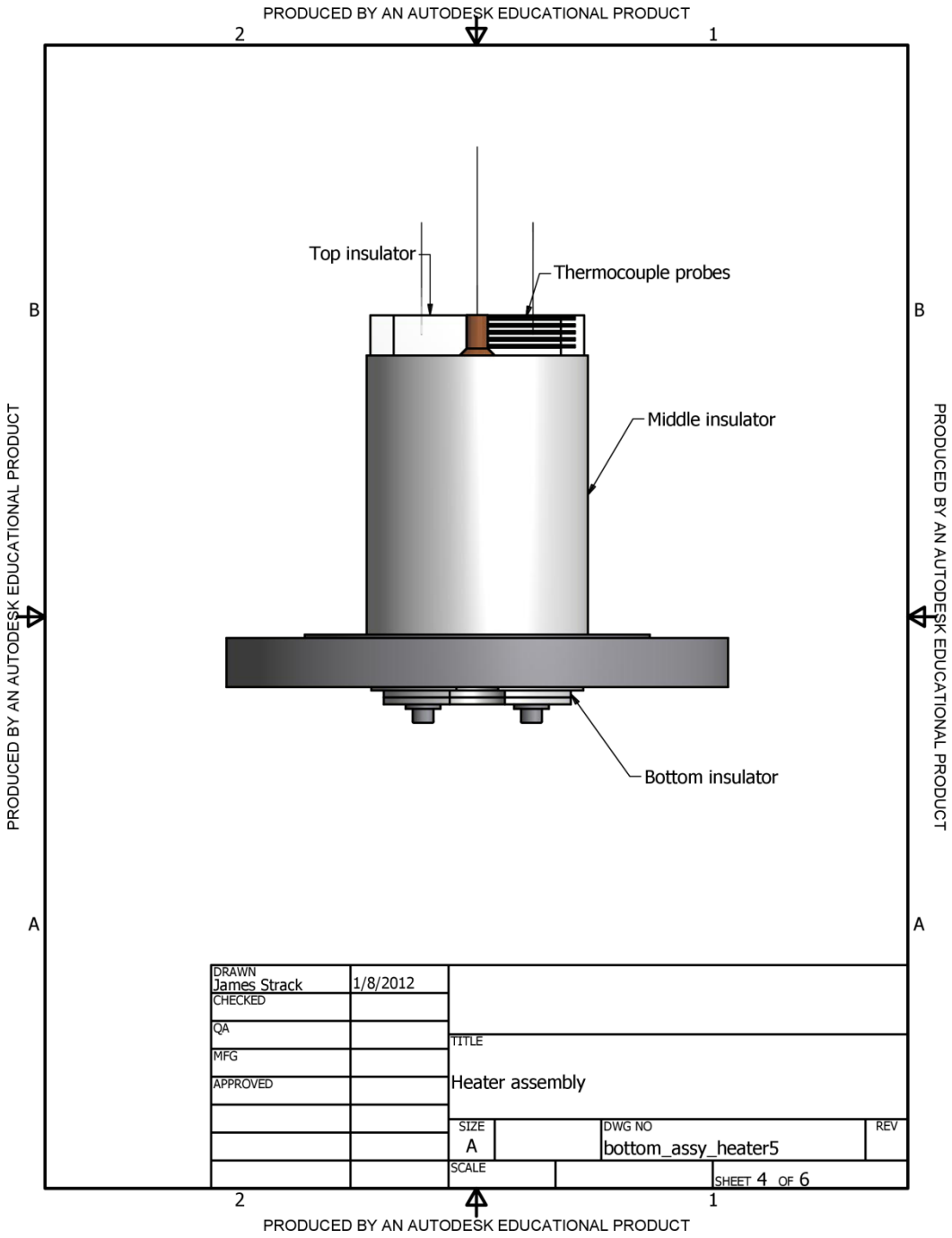
PRODUCED BY AN AUTODESK EDUCATIONAL PRODUCT
Top insulator
Thermocouple probes
Middle insulator
Bottom insulator
DRAWN James Strack 1/8/2012
CHECKED
QA
MFG
APPROVED
TITLE
Heater assembly
SIZE A
DWG NO bottom_assy_heater5
REV
SCALE
SHEET 4 OF 6

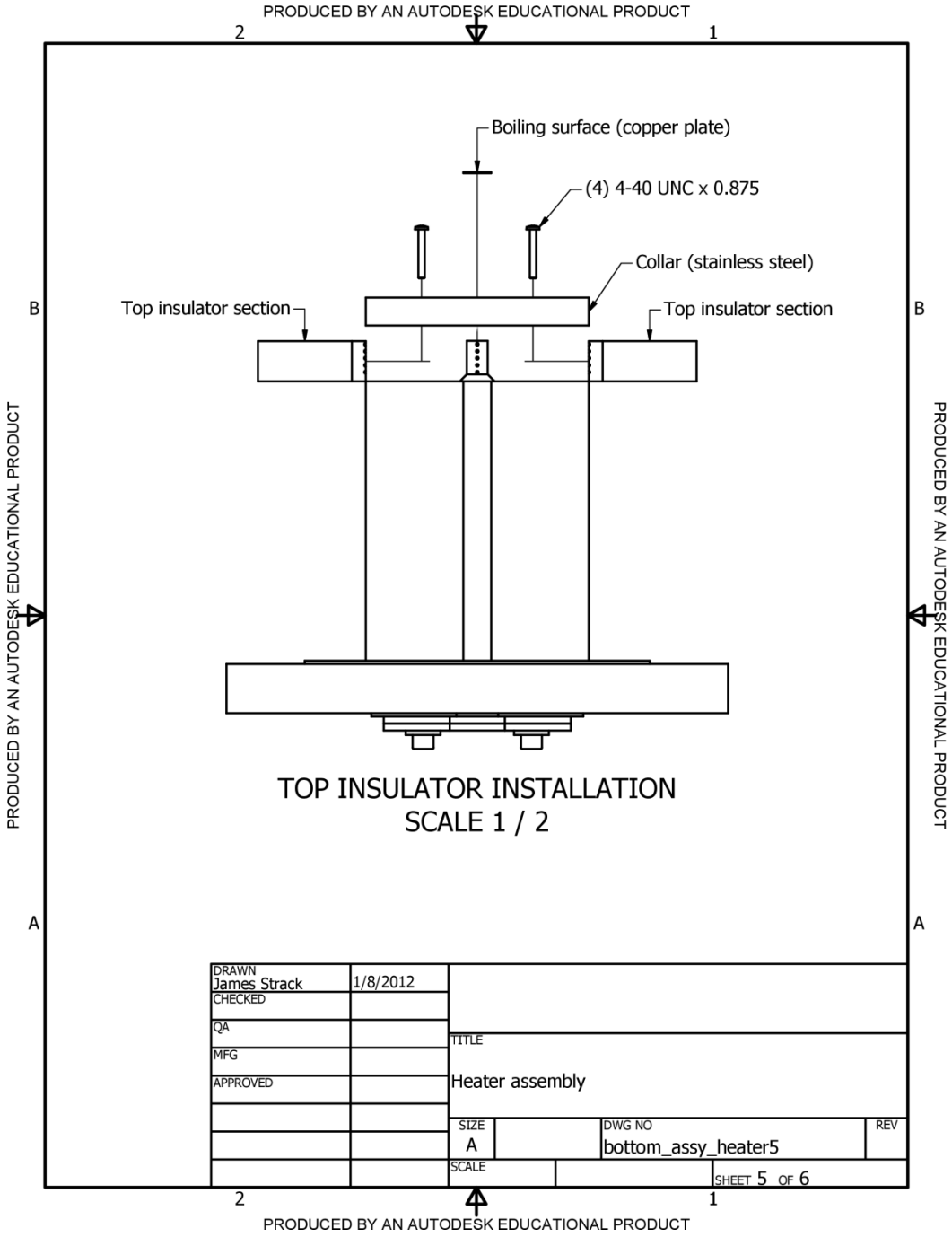
PRODUCED BY AN AUTODESK EDUCATIONAL PRODUCT
Boiling surface (copper plate)
(4) 4-40 UNC x 0.875
Collar (stainless steel)
Top insulator section
Top insulator section
TOP INSULATOR INSTALLATION
SCALE 1 / 2
DRAWN James Strack 1/8/2012
CHECKED
QA
MFG
APPROVED
TITLE
Heater assembly
SIZE A
DWG NO bottom_assy_heater5
REV
SCALE
SHEET 5 OF 6

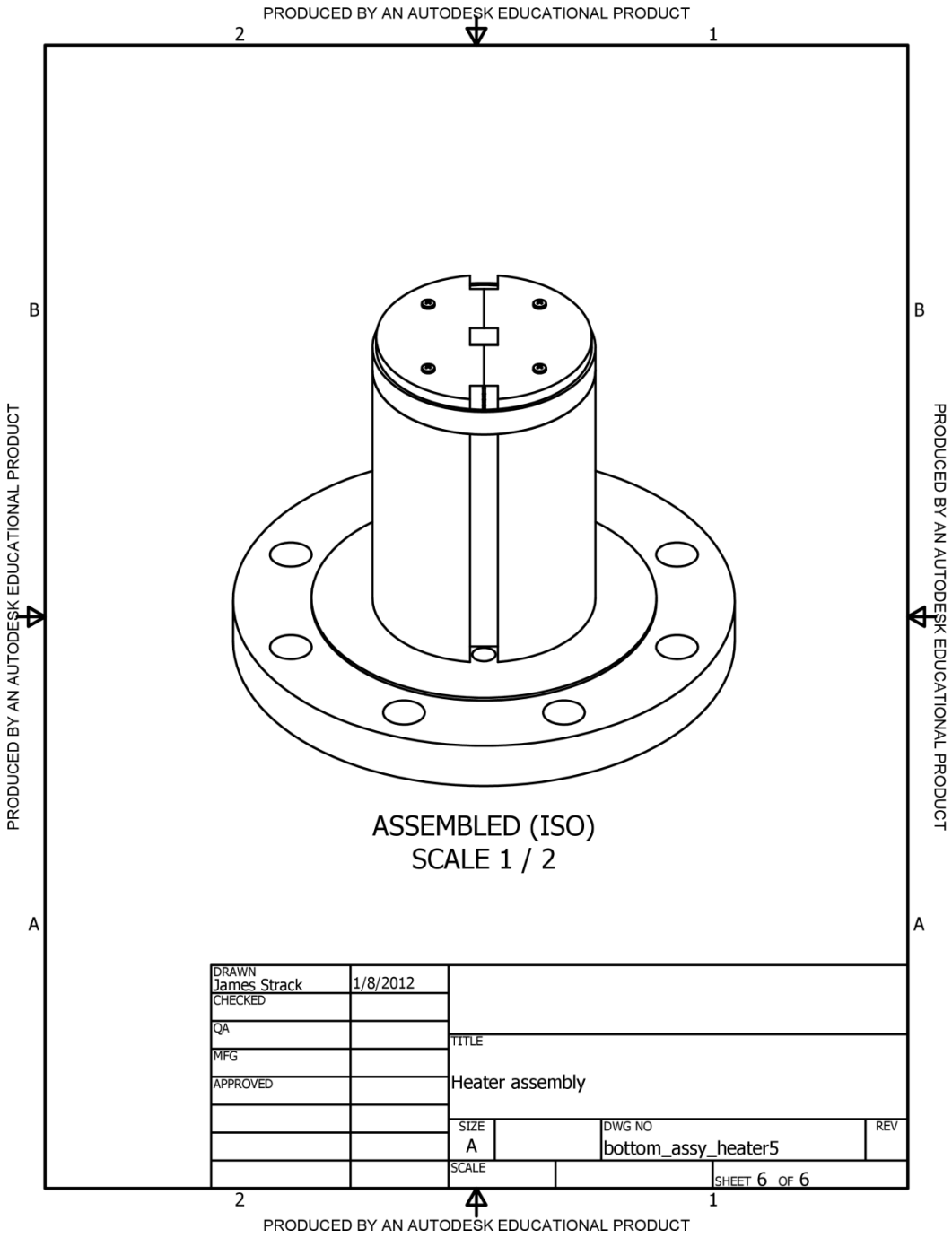
PRODUCED BY AN AUTODESK EDUCATIONAL PRODUCT
PRODUCED BY AN AUTODESK EDUCATIONAL PRODUCT
PRODUCED BY AN AUTODESK EDUCATIONAL PRODUCT
PRODUCED BY AN AUTODESK EDUCATIONAL PRODUCT
ASSEMBLED (ISO)
SCALE 1 / 2
DRAWN James Strack 1/8/2012
CHECKED
QA
MFG
APPROVED
TITLE
Heater assembly
SIZE A
DWG NO bottom_assy_heater5
REV
SCALE
SHEET 6 OF 6

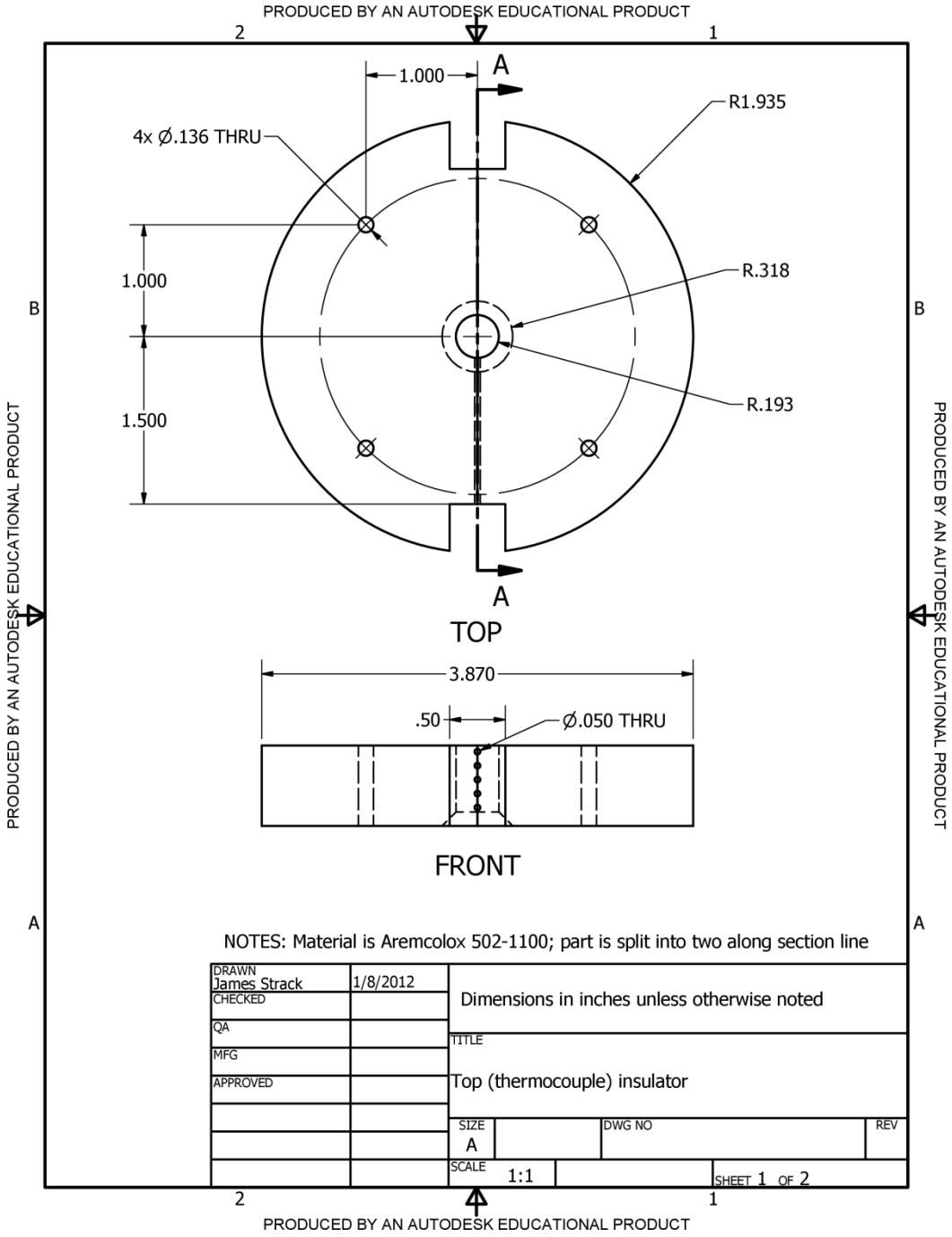
PRODUCED BY AN AUTODESK EDUCATIONAL PRODUCT
1.000
A
R1.935
4x Ø.136 THRU
1.000
R.318
1.500
R.193
A
TOP
3.870
.50
Ø.050 THRU
FRONT
NOTES: Material is Aremcolox 502-1100; part is split into two along section line
DRAWN James Strack 1/8/2012
CHECKED
QA
MFG
APPROVED
Dimensions in inches unless otherwise noted
TITLE
Top (thermocouple) insulator
SIZE A
DWG NO
REV
SCALE 1:1
SHEET 1 OF 2

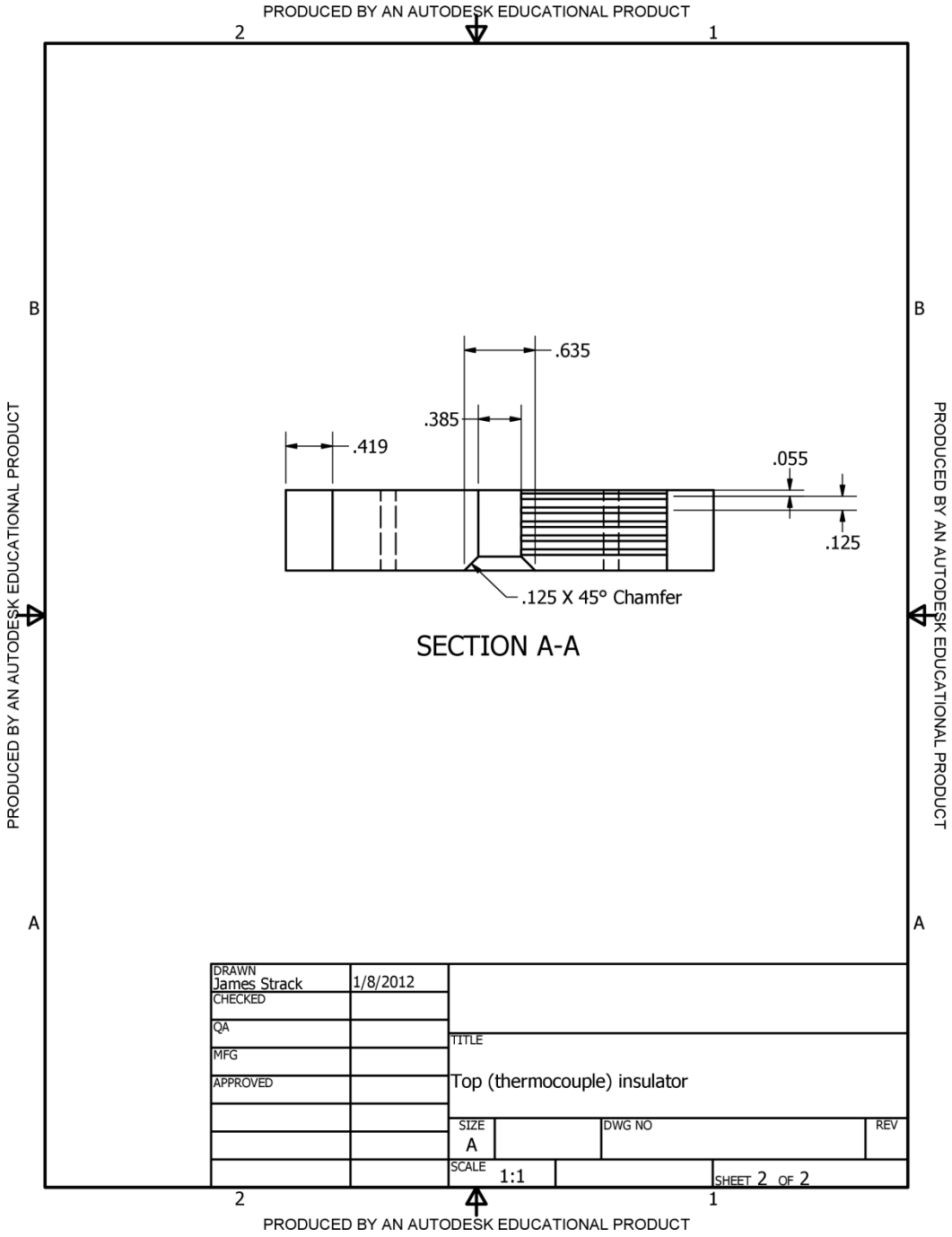
PRODUCED BY AN AUTODESK EDUCATIONAL PRODUCT
PRODUCED BY AN AUTODESK EDUCATIONAL PRODUCT
PRODUCED BY AN AUTODESK EDUCATIONAL PRODUCT
PRODUCED BY AN AUTODESK EDUCATIONAL PRODUCT
.635
.385
.419
.055
.125
.125 X 45° Chamfer
SECTION A-A
DRAWN James Strack 1/8/2012
CHECKED
QA
MFG
APPROVED
TITLE
Top (thermocouple) insulator
SIZE A
DWG NO
REV
SCALE 1:1
SHEET 2 OF 2

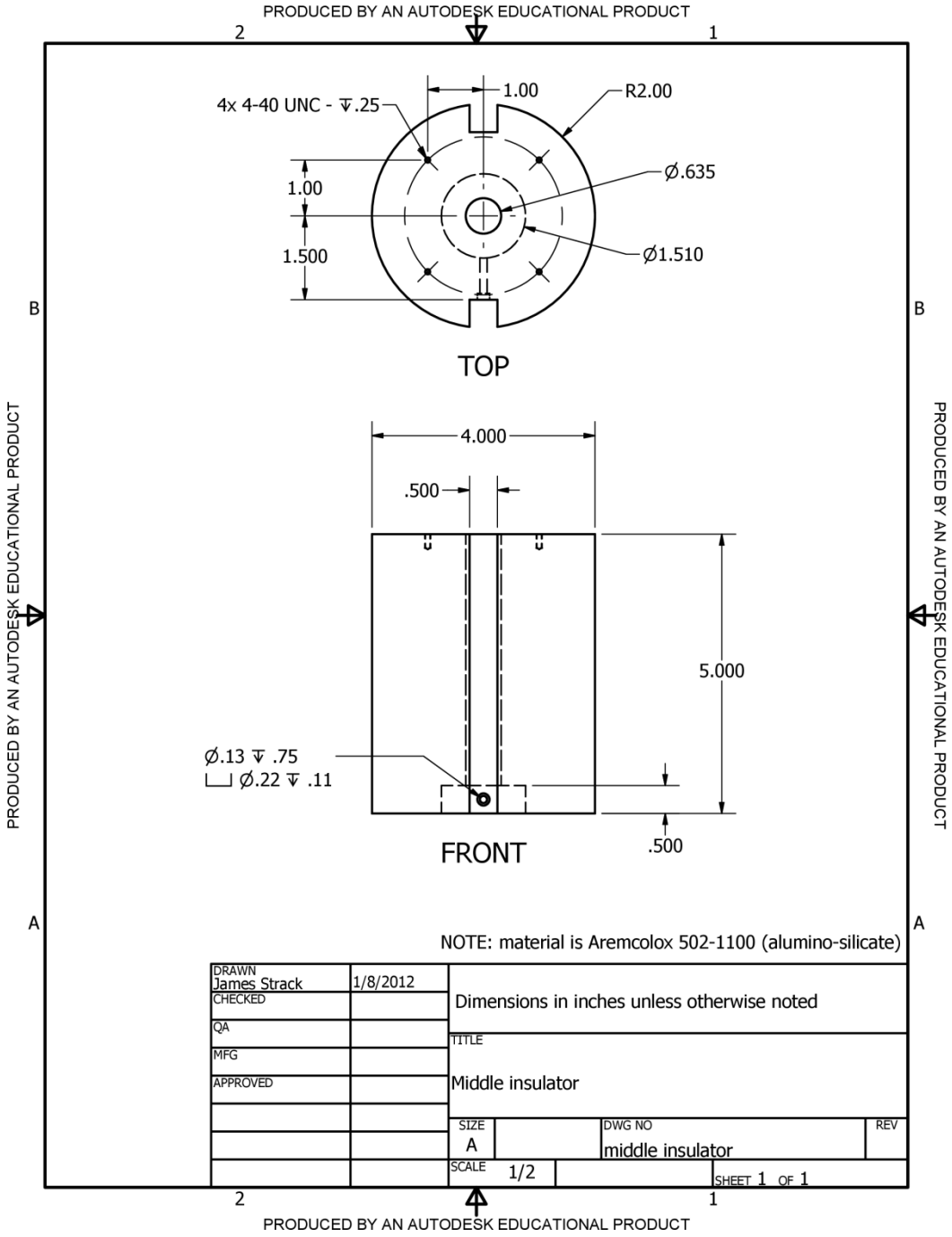
PRODUCED BY AN AUTODESK EDUCATIONAL PRODUCT
4x 4-40 UNC - ↧.25
1.00
R2.00
1.00
Ø.635
1.500
Ø1.510
TOP
4.000
.500
5.000
Ø.13 ↧ .75
⌴ Ø.22 ↧ .11
.500
FRONT
NOTE: material is Aremcolox 502-1100 (alumino-silicate)
DRAWN James Strack 1/8/2012
CHECKED
QA
MFG
APPROVED
Dimensions in inches unless otherwise noted
TITLE
Middle insulator
SIZE A
DWG NO middle insulator
REV
SCALE 1/2
SHEET 1 OF 1

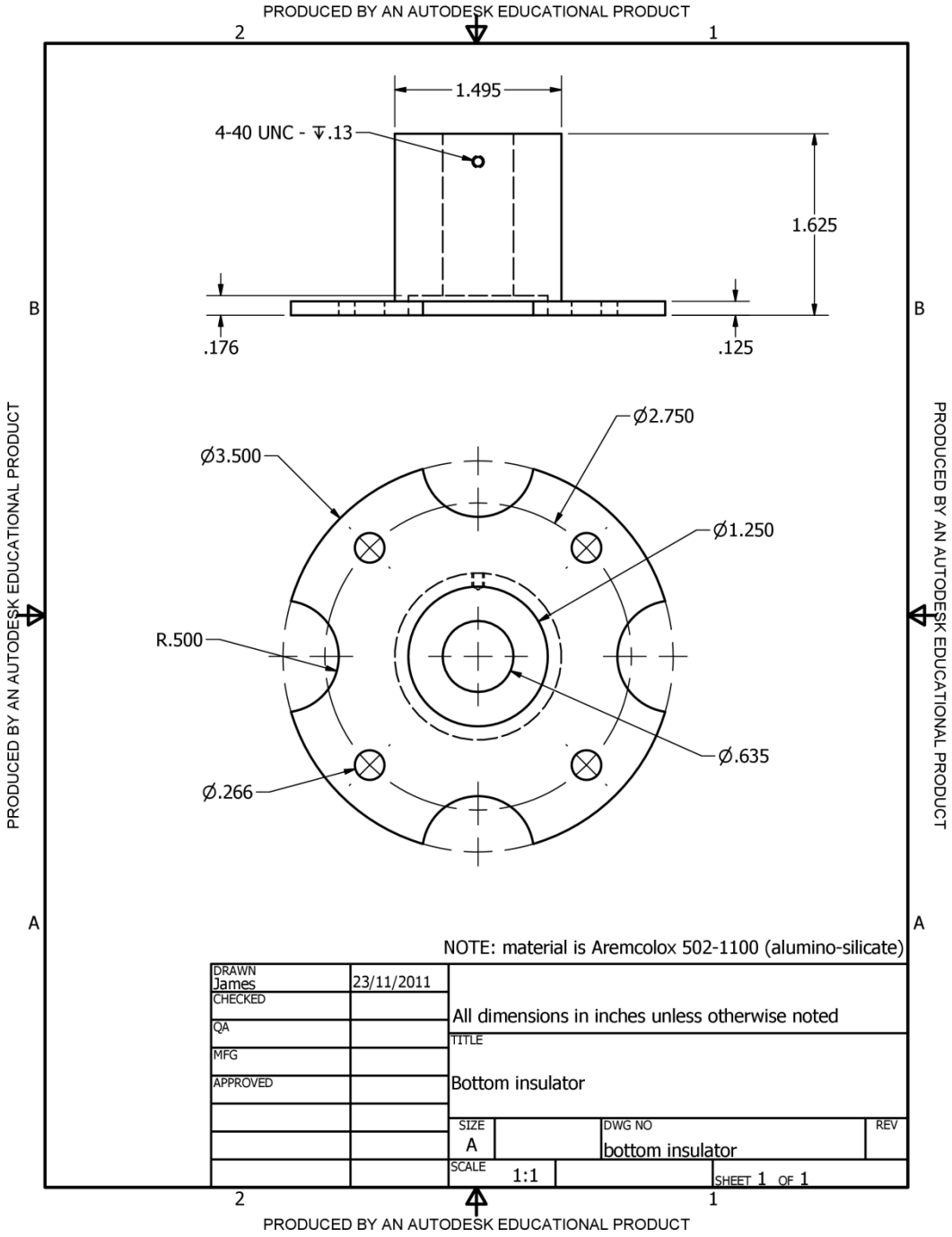
PRODUCED BY AN AUTODESK EDUCATIONAL PRODUCT
1.495
4-40 UNC - ↧.13
1.625
.176
.125
Ø2.750
Ø3.500
Ø1.250
R.500
Ø.635
Ø.266
NOTE: material is Aremcolox 502-1100 (alumino-silicate)
DRAWN James 23/11/2011
CHECKED
QA
MFG
APPROVED
All dimensions in inches unless otherwise noted
TITLE
Bottom insulator
SIZE A
DWG NO bottom insulator
REV
SCALE 1:1
SHEET 1 OF 1

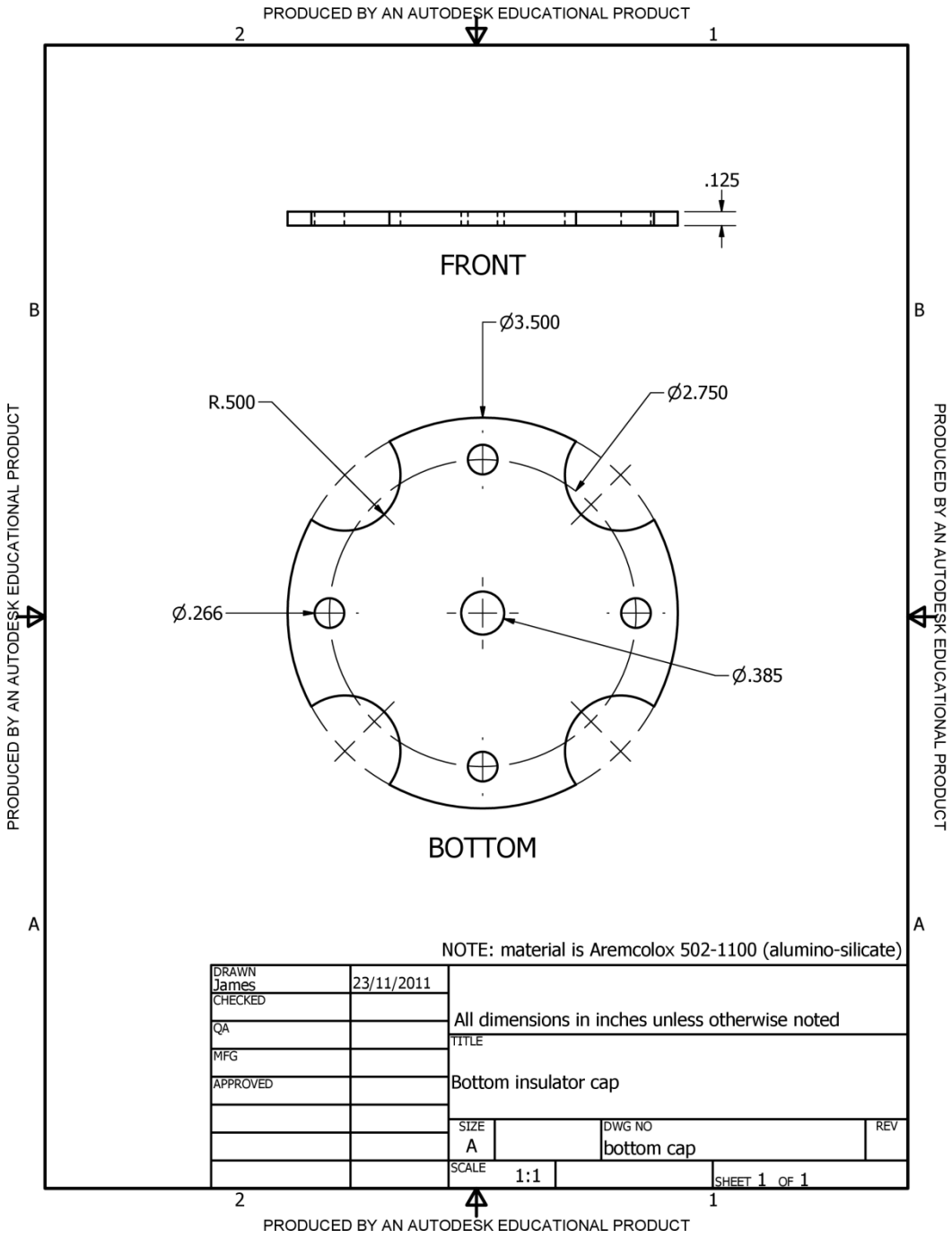
PRODUCED BY AN AUTODESK EDUCATIONAL PRODUCT
.125
FRONT
Ø3.500
R.500
Ø2.750
Ø.266
Ø.385
BOTTOM
NOTE: material is Aremcolox 502-1100 (alumino-silicate)
DRAWN James 23/11/2011
CHECKED
QA
MFG
APPROVED
All dimensions in inches unless otherwise noted
TITLE
Bottom insulator cap
SIZE A
DWG NO bottom cap
REV
SCALE 1:1
SHEET 1 OF 1

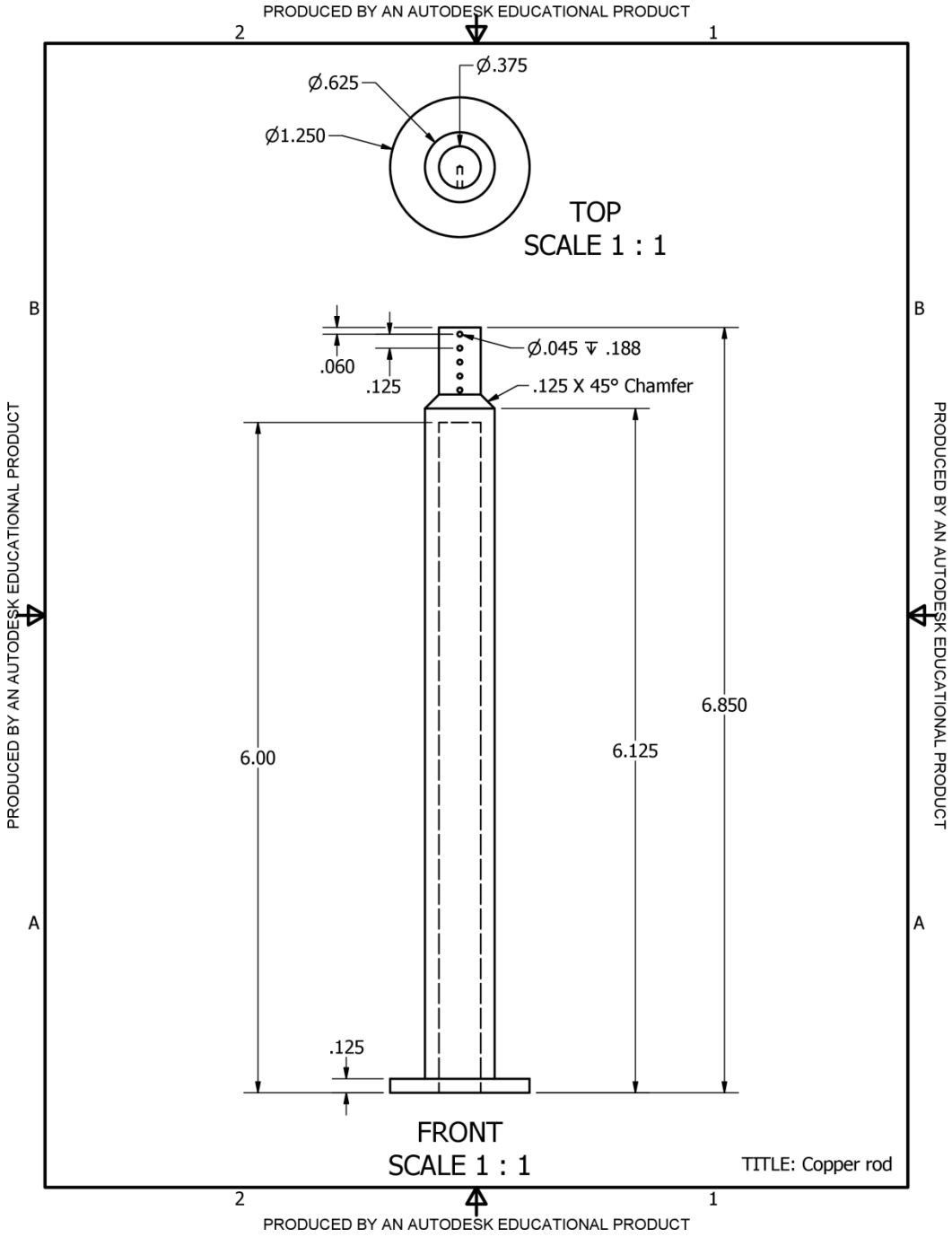
PRODUCED BY AN AUTODESK EDUCATIONAL PRODUCT
Ø.625
Ø.375
Ø1.250
TOP
SCALE 1 : 1
.060
.125
Ø.045 ↧ .188
.125 X 45° Chamfer
6.00
6.125
6.850
.125
FRONT
SCALE 1 : 1
TITLE: Copper rod

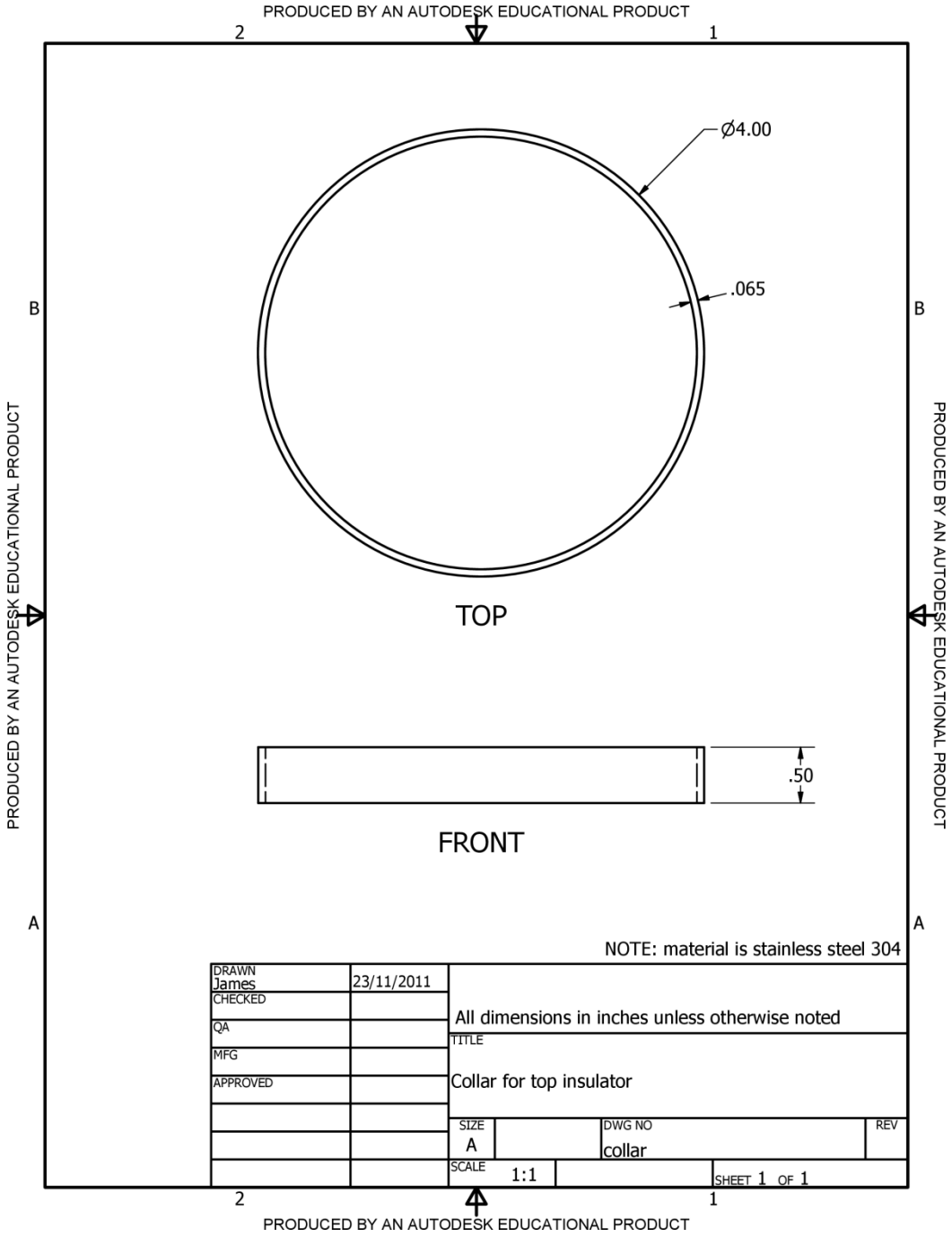
PRODUCED BY AN AUTODESK EDUCATIONAL PRODUCT
Ø4.00
.065
TOP
.50
FRONT
NOTE: material is stainless steel 304
DRAWN James 23/11/2011
CHECKED
QA
MFG
APPROVED
All dimensions in inches unless otherwise noted
TITLE
Collar for top insulator
SIZE A
DWG NO collar
REV
SCALE 1:1
SHEET 1 OF 1